INFORMATION SOCIETY TECHNOLOGIES (IST) PROGRAMME
Future and Emerging Technologies (FET)

Deliverable D33
FINAL REPORT

Project acronym: OLAS
Project full title: Organic electrically pumped LASer by engineering of heterojunctions in field-effect devices

Proposal/Contract n°.: EU-IST- *FP6-015034*

Operative commencement date of contract: 01.01.2006
Contract Duration: 36 months
Date of preparation: 15.02.2009

Period covered: from 01/01/2006 to 31/12/2008

Project coordinator name: Muccini Michele

Project coordinator organisation name: CNR, Consiglio Nazionale delle Ricerche, Italy

CONTENT

Executive Summary

The project aimed at performing foundational research in the field of organic optoelectronics and in particular aimed at exploring novel approaches based on field-effect technology to achieve an electrically pumped organic laser. The project strategy envisioned the use of an innovative approach based on the engineering of organic heterojunctions in field-effect devices by integration of all the needed scientific and technological competences. All activities were synergistically integrated in the project: photonic and optoelectronic device modelling, photonic nanofabrication technologies, ultra-broad-band characterisation of photonic nanostructures, field-effect device technology, OLED technology, organic materials and heterojunctions engineering, advanced growth methods for highly ordered organic heterojunctions, laser scanning confocal microscopy and spectroscopy for heterojunctions imaging and characterisation, ultrafast spectroscopy, optoelectronic device characterization and testing.

The main objectives of the projects are briefly described in the table below.

Milestone /WP /month	Brief description of Milestone objectives
M1 /WP1 /m6	First choice of organic materials for heterojunctions
M2 /WP2 /m6	Design of photonic feedback structures
M3 /WP3 /m12	Fabrication of the photonic feedback structure
M4 /WP5 /m12	Technology for organic heterojunctions field-effect devices assessed
M5 /WP2 /m15	Simulation of heterojunction device structures
M6 /WP4 m18	Achieve optically pumped laser of organic heterojunctions on photonic feedback structures
M7 /WP6 /m18	Final choice of organic materials for heterojunctions
M8 /WP7 /m21	Fabricate organic heterojunction field-effect devices with integrated photonic feedback structure
M9 /WP7 /m27	Achieve optically pumped laser in organic heterojunctions field-effect devices under electrical bias
M10 /WP8 /m30	Achieve stimulated emission by electrical pumping of organic heterojunctions field-effect devices
M11 /WP8 /m33	Achieve electrically pumped laser in organic heterojunctions field-effect devices
M12 /WP9 /m36	Assessment of electrically pumped organic laser technology

Table 1. Milestone objectives

The consortium was formed by five partners from four European nations, including one SME, one prominent industrial enterprise, a national research lab, an independent research organisation and an academic research institution. These groups, international leaders in their respective field, complemented their expertise and facilities to reach the ambitious objectives of the project.

Partner		Organisation	Country	Business activity area	RTD role in project
CO	1	CNR- Istituto per lo Studio dei Materiali Nanostrutturati, Bologna (CNR-ISMN)	IT	Gov. Res. Org. Research on nanostructured materials	Coordination; OMBD organic heterojunction growth, interface engineering, Laser Scanning Confocal microscopy and spectroscopy, optoelectronic characterisation of heterojunctions, mapping emission area of devices.
P	2	Interuniversity Microelectronics Centre, Leuven (IMEC)	BE	Res. Cent. R&D in Micro-electronics	Technological development and fabrication of field-effect heterojunction device structures, electrically pumped laser.
P	3	RWTH Aachen, Institute für Halbleiter-Technik (IHT)	D	University Res. centre, Ultrafast photonics, opto- and nano-electronics	Linear optical characterisation of photonic devices, spectroscopy of materials.
P	4	AMO GmbH, Aachen (AMO)	D	SME, nanotechnology and advanced microelectronics	Manufacturing of inorganic photonic nanostructures
P	5	IBM Zurich Research Laboratory (IBM-ZRL)	CH	Ind. Res. Lab. Sci &Tec Dept.Display Tech and Optical Networking	Specification for organic lasers, Design and modelling of device structures, OLED technology, optically pumped laser, measuring and testing of optoelectronic devices, technology assessment.

Table 2. OLAS consortium overview

The co-ordinator contact details are:
Dr. Michele Muccini
CNR-ISMN
Via P. Gobetti, 101
40129 Bologna, ITALY
E-mail: M.Muccini@bo.ismn.cnr.it
Project website: www.olasproject.eu

The consortium achieved the following major results:

- state-of-the-art ambipolar and balanced mobility in light-emitting field-effect transistors, which employ a double layer organic heterojunction.
- Photonic feedback structures suitable to be integrated in field-effect devices were fabricated by interference lithography.
- The photonic characteristics of the novel device structure were modelled and used as a guide for the fabrication of the fully integrated optoelectronic-photonic device.
- A novel design of planar photonic feedback structures that prevents losses at the edges thereby decreasing the lasing threshold in ultrasmall lasing active areas was demonstrated.
- A novel field-effect hybrid device structure was thoroughly investigated and its optoelectronic properties modelled.
- A novel three-layer field-effect organic heterojunction approach was demonstrated and the corresponding devices characterized.
- In depth knowledge of the dielectric-organic and organic-organic interface characteristics were gained and used to fabricate light-emitting field-effect transistors with state of the art n- type and p-type current densities.
- A complete technology set for the fabrication of field-effect organic heterojunction devices, both planar and hybrid, was developed.
- The first ever made integrated photonic field-effect device was fabricated.
- ASE and lasing properties of organic heterojunctions on photonic feedback structure under optical pumping were determined.
- The charge-induced losses in the tri-layer vertical heterojunction device under electrical bias condition were evaluated.
- A novel hybrid approach with organics and silicon-on-insulator technology for photonic feedback structures was designed and realized.
- Three patents were filed to ensure possible exploitation.

The fabrication of the integrated photonic field-effect devices faced highly technical complexity and was not as fast as anticipated. This led to a delay in the fully integrated device preparation that did not allow the consortium to achieve the electrically pumped lasing in the limited time frame of the project.

However, the consortium developed specific and unique know-how on photonic field-effect organic heterojunctions that represents a key competitive advantage over international competitors in USA

and Japan in the field. It is worth highlighting that the results of the OLAS consortium partners are an international benchmark for the photonic field-effect organic heterojunction approach.
In order to strengthen the European leadership, the OLAS consortium took the initiative to organise topical discussions with other European groups and consortia (e.g., the German OLAS consortium) in order to spread within the European scientific community its results and to promote the exchange of ideas on the most critical technological and scientific issues.

In addition to these specific actions targeting the European scientific and technological community, the consortium was active in disseminating the results via publications in international top ranked scientific journals and in gathering an ever increasing international community to be active on the topic of the project. Dissemination via organization and participation to thematic workshops was selected as a preferential mean to raise awareness and stimulate interest of the most relevant academic and industrial actors on the results achieved by the project. OLAS served as a cooperating organization for the SPIE Europe's Photonic Europe Conference held in Strasbourg on 7-11 April, 2008. Within the SPIE Europe's Photonic Europe Conference OLAS partners organized a thematic workshop on "Organic Optoelectronics and Photonics" where the topics of organic lasing and light emitting field-effect structures were specifically addressed. The attendance to the workshop was particularly high (an average of 120 attendees was registered) and OLAS partners presented extensively their results. In addition, CNR organised an international conference devoted to electroluminescent phenomena in both organic and hybrid structures (EL2008 "14th International Workshop on Inorganic and Organic Electroluminescence & 2008 International Conference on the Science and Technology of Emissive Display and Lighting", Rome, 9-12 September 2008).

Section 1 – Project execution

a. Project objectives

The primary objective of the project was the exploration of a novel approach based on photonic field effect organic heterojunctions for the realization of an electrically pumped organic laser. The principal targeted device characteristics and specifications were the following:

- N-type and p-type charge transport in the device is accomplished using different dedicated materials, each one with optimised performances.
- A host-guest system is used for lasing emission.
- The guest emitter and the host-guest system are to be selected and properly engineered during the course of the project.

- Emission is preferably in the red to allow a wider choice of the transport and host materials.
- Operation is at room temperature.
- Electrical driving is in pulsed mode.
- The optical output power for the first technological demonstration will be limited to nW - μW.

Intermediate objectives of the project, which proved valuable in themselves, were:

1. To establish novel integrated design for multifunctional organic devices based on the integration of organic heterojunctions, field-effect structures and photonic feedback structures.
2. To fabricate innovative resonant photonic structures compatible with multifunctional field-effect device technology.
3. To engineer organic heterojunctions with controlled interfacial properties capable of sustaining high ambipolar current density and efficient light emission.
4. To integrate electronic and photonic heterojunctions with optical feedback structures in a field-effect configuration.
5. To achieve optically pumped lasing in field-effect organic heterojunction devices.
6. To evaluate the main optical losses (polaron, contact or triplet quenching) in a real device including all injecting and non-injecting contacts.
7. To file patent applications in order to make possible the exploitation of the project results.

The goal of achieving an electrically pumped organic laser was long pursued by the international scientific community and has recently become a very hot topic thanks to highly promising results. On the one hand, the advances achieved in the brightness and current density values in organic light-emitting diodes revamped the search for injection lasing using the consolidated OLED structure. On the other hand, the constant improvement in device performances of light-emitting field-effect transistors prompted the use of planar device structures.

A number of projects have started in the last two years in Asia, USA and Europe which pursue the organic laser following either of the two approaches. Within this context the results achieved by the consortium partners on light-emitting field-effect devices make the OLAS project a benchmark as witnessed by the top rank scientific publications and invited talks in international topical conferences.

b. Major project results

The major results achieved during the project include:

- The modelling of the photonic and optoelectronic characteristics of the newly proposed device structure that were then used in the course of the project as a guide for the fabrication of the integrated photonic heterojunction device.
- The design and fabrication of an innovative planar photonic feedback structure that enables ultrasmall footprint surface emitting lasers. This allows in principle high integration density in the final device without increase of the optical losses at the edges of the structure.
- The development of a complete technology set for the fabrication of photonic field-effect organic heterojunction devices, both planar and hybrid.
- state-of-the-art ambipolar and balanced mobility in light-emitting field-effect transistors, which employ a double layer organic heterojunction.
- The realization of light-emitting field-effect transistors with state of the art n-type and p-type current densities (up to 1KA/cm^2). The active layer of the device is based on a three layer vertical heterojunction.
- The fabrication for the first time of an integrated photonic field-effect device.
- The determination of the ASE properties of the three layer vertical heterojunction device under optical pumping.
- The determination of the lasing properties of field-effect organic heterojunctions on photonic feedback structure under optical pumping.
- The evaluation of the charge-induced losses in the tri-layer vertical heterojunction device under electrical bias condition.
- The design and realization of a novel hybrid approach with organics and silicon-on-insulator technology for photonic feedback structures.
- The filing of three patents to ensure future possible exploitation of the project results.

c. Workpackages activities

WP1. Specification definitions (WP leader: CNR)

Workpackage 1 was devoted to define and regularly update the specifications of the n-type and p-type transport materials, of the emitting compounds and of the lasing organic heterojunction structures.

The activity started by recognizing that, in the heterojunction approach, each material should have a specific optimized function in the device and must be compatible with the other active materials forming the photonic heterostructure. The compatibility should hold both from the energetic as well as from the processing point of view. Therefore the energy gaps and the energetic positions of the HOMO and LUMO levels of the materials should allow efficient electron and hole transport coupled to the highest possible light emission efficiency.

The task of the definition of the n-type and p-type transport materials' characteristics, mainly worked out by CNR, has established that the selected *p* and *n* conductors must possess field-effect charge mobility of the order of 10^{-2} -10^{-1} cm^2/Vs. Indeed, equal and high mobility values for both positive and negative charges would be highly desirable from the one hand to maximize currents balance and charge recombination, and from the other hand to minimize the required charge carrier densities in the device. In addition, a high charge mobility will determine the switching time of the field-effect lasing device. The transport properties of candidate materials were evaluated using single layer Organic Thin Film Transistors (OTFTs) devices as test structures. The energetic characteristics of the n- and p-type materials must be such that the n-conductor act as a hole blocking material, while the p-conductor is an electron blocking material. In addition it is required that the energy band gap is equal or higher than 2 eV in order to assure the best energetic overlap with the light emitting compound.

At the beginning of the project suitable n-type transport materials were identified in α, ω-diperfluorohexyl-4T (DHF4T) and N, N-ditridecylperylene-3,4,9,10-tetracarboxylic diimide (P13). The molecular structures and the HOMO and LUMO energy levels are reported in Figure 2.1.1.

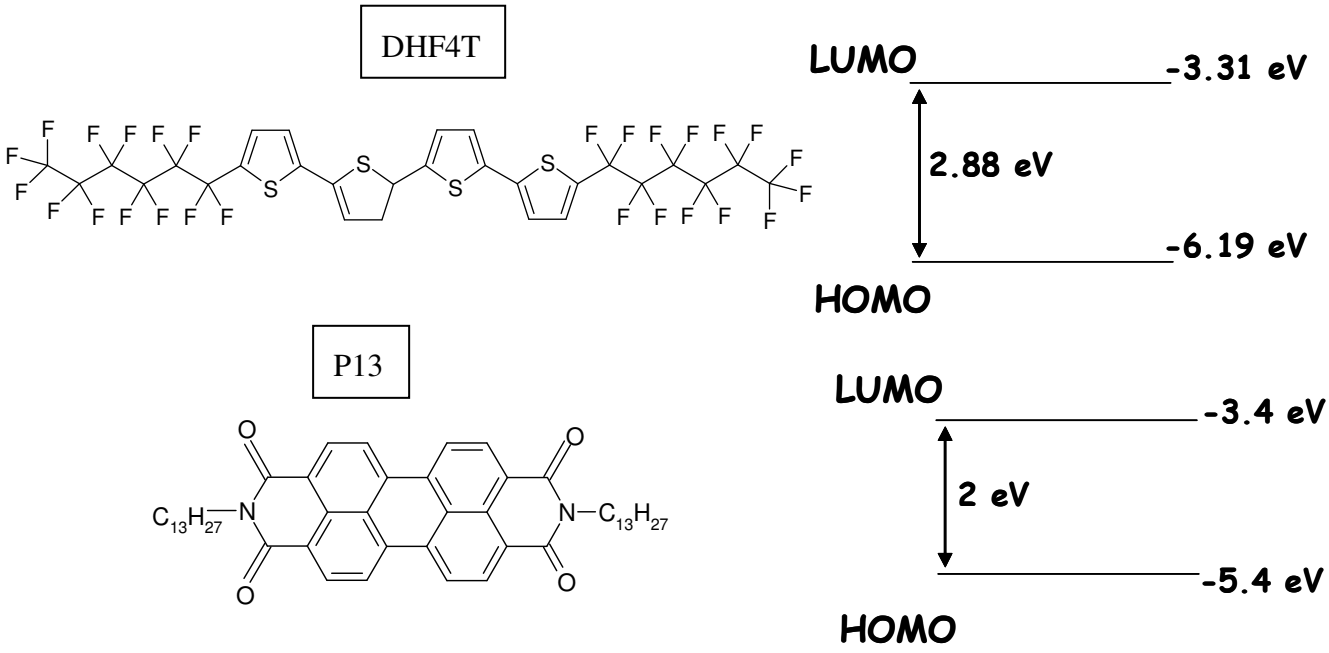

Fig. 2.1.1. Molecular structures and HOMO and LUMO energy levels of α, ω-diperfluorohexyl-4T (DHF4T)

and N, N-ditridecylperylene-3,4,9,10-tetracarboxylic diimide (P13).

Among p-type transport materials we identified p-(α,ω)-dihexyl-quaterthiophene (DH4T) and p-hexaphenyl (P6), whose molecular structures and the HOMO and LUMO energy levels are reported Figure 2.1.2.

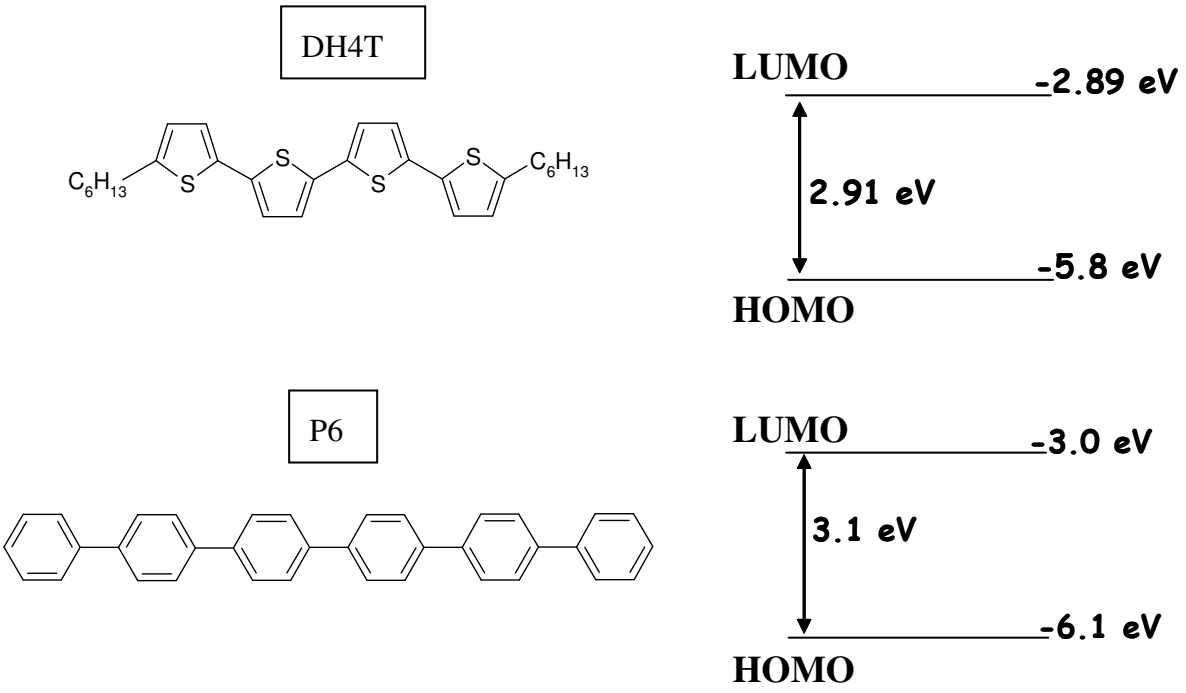

Fig. 2.1.2 Molecular structures and HOMO and LUMO energy levels of p-(α,ω)-dihexyl-quaterthiophene (DH4T) and p-hexaphenyl (P6).

The task of identifying the specific properties that light emitting and lasing materials should have, has been performed by CNR and IBM. At the stage of defining specifications, we considered both singlet emitters ad triplet emitters as suitable candidates. Emitters should be selected for their optical properties and for their energetic compatibility with the n and p conductors.

The final choice of the emitting material must be strictly related to the host material and the host-guest system should be regarded as a single functional unit. The parameters to be used for evaluation of the emitting system were established to be the following: i) energy position and intensity of the optical gain; ii) eventual residual absorption of the host material within the energy range of the optical gain of the guest, which could lead to significant optical losses; iii) energetic position of the triplet levels of the host material to be used with triplet emitters.

Pump & Probe spectroscopy was therefore envisaged as being of crucial importance to evaluate the photonic properties of the organic heterojunction.

4-(dicyanomethylene)-2-methyl-6-(p-dimethylaminostyryl)-4H-pyran (DCM) and bis(2-(2'-benzothienyl)-pyridinato-N,C3')iridium(acetylacetonate) [$(btp)_2Ir(acac)$] were identified as candidate emitting materials, representing the broader family of singlet emitters and triplet emitters, respectively. At the beginning of the project the consortium was aware that triplet emitters have never been observed to generate Amplified Spontaneous Emission (ASE) upon optical pumping (and obviously neither by electrical pumping). Therefore, the consortium decided to perform specifically targeted experiments to clarify the possibility of using triplet emitters as lasing media.

A model host-guest system formed by tris(quinolin-8-olato)aluminum(III) (Alq3) as a host and 4-(dicyanomethylene)-2-methyl-6-(p-dimethylaminostyryl)-4H-pyran (DCM) as a guest was considered as a well known reference system. Photoluminescence and Amplified Emission Experiments (ASE) experiments were performed on the Alq_3:DCM model system to derive the specific photonic parameters to be used to benchmark the final heterojunction. This task was primarily performed by CNR (sample preparation) and by RWTH (spectroscopic experiments).
ASE measurements were performed by focusing the 400 nm pump beam near one edge of the sample with an elliptical Gaussian beam profile (vertical FWHM: 70µm, horizontal FWHM: 1500µm). The polarization of the pump beam was set vertically to maximize emission along the elongated pumped region of the organic film. The obtained photoluminescence spectra are shown in Figure 2.1.3(a), indicating the dependence of the spectral emission on the excitation fluence per pulse. The threshold of ASE is determined quantitatively from the plot displayed in Figure 2.3(b), that shows how the PL- and ASE-intensity depend linearly on the excitation energy, with a clear slope change at the ASE threshold. From the intersection between the two linear fits, one for the region below threshold and one for the region above threshold, we obtain a threshold value for ASE of ~32 µJ/cm^2.

a) **b)**

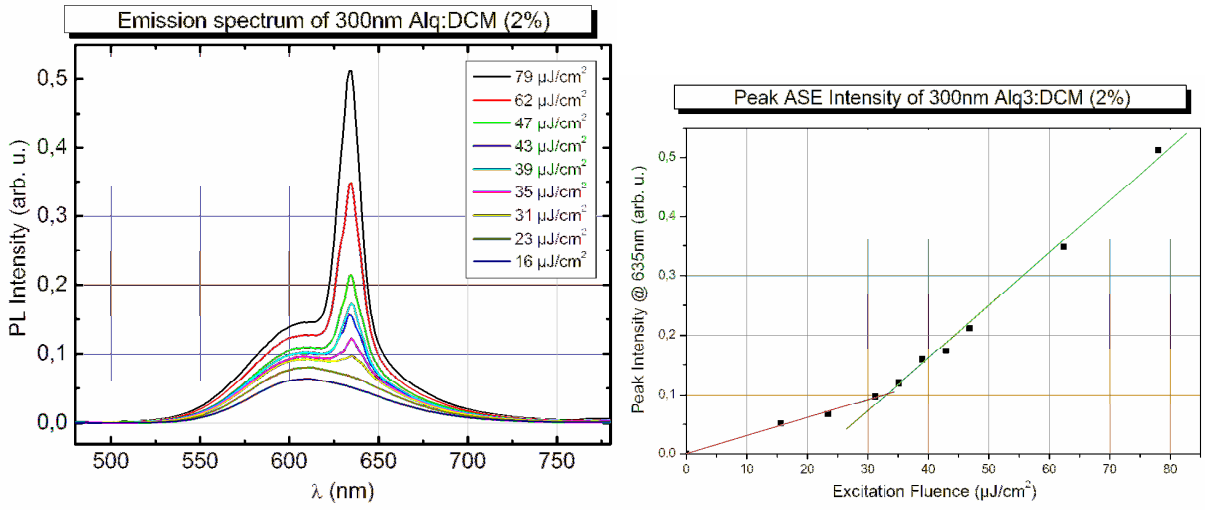

Figure 2.1.3. a) Photoluminescence spectra of an alq3:DCM(2%) film at different excitation fluences. B) Photoluminescence peak intensity as a function of the excitation fluence.

In addition to the planar heterojunction geometry envisioned in the proposal, an alternative device structure was considered, that is a hybrid structure between a light-emitting diode and a field-effect transistor. The intended device structure, which minimizes the optical losses by moving the metallic contact away from the recombination zone, is shown in Figure 2.1.4. Light generation occurs at a distance of several microns from the metal contact, reducing exciton quenching and photon absorption.

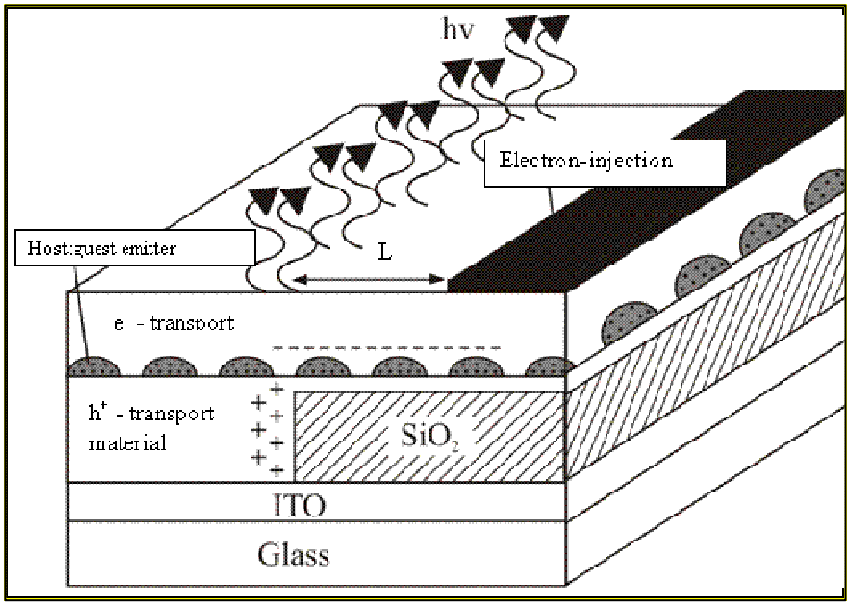

Figure 2.1.4. Envisioned device structure comprising a light-emitting field-effect device based on a vertical organic heterojunction.

The energy diagram of the device structure is depicted in Figure 2.1.5.

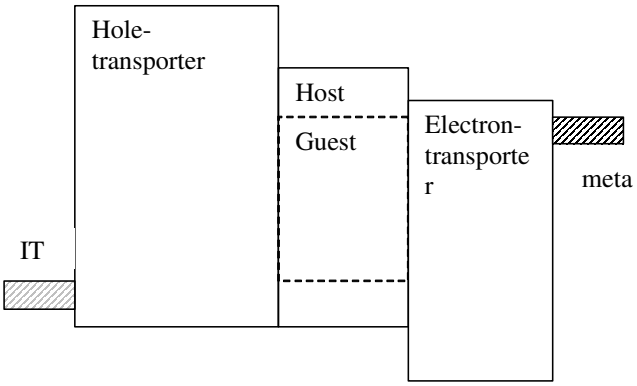

Figure 2.1.5. Schematic band diagram for the device structure depicted in figure 2.1.4.

A novel device architecture based on a three layer vertical organic heterojunctions in planar field-effect devices was also introduced. A three component vertical organic heterojunction embedded in

a planar field effect transistor structure has the potential to generate electroluminescence via the recombination of balanced n-type and p-type high current densities. If the heterojunction is properly engineered, balanced current densities higher than 1KA/cm^2 could be achieved. The device structure also prevents exciton quenching at metal electrodes as they are fabricated several microns apart from the active channel area where exciton recombination is expected to occur.
A schematic view of the three layer heterojunction device structure is reported in figure 2.1.6.

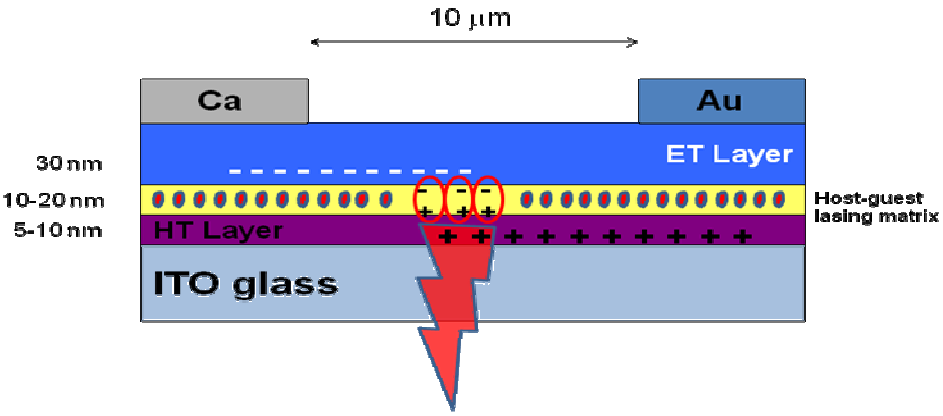

Fig. 2.1.6: Three layer vertical organic heterojunctions in planar field-effect devices. Each layer thickness is designed to maximise both the current density and the exciton recombination probability. Final specifications will depend on the growth properties and electronic and optoelectronic characteristics of the specific materials employed.

Potentially the device structure can afford current densities on the order of KA/cm^2 for both carrier types. In order to comply with these figures, n-type and p-type mobility on the order of 10^{-1} cm^2/Vs must be achieved. This will be strictly related to quality of the relevant interfaces in the organic heterojunction. Indeed, in the proposed scheme the hole field-effect charge transport is expected to take place at the interface with the dielectric, while the electron transport occurs at the interface between the host-guest lasing layer and the n-type layer. The careful control of each layer growth and the proper engineering of the interfaces are crucial to the electronic and optoelectronic device properties. Specific experimental tasks were devoted to these aspects in WP4.
At this stage of definition the device structure did not explicitly include an optical resonant cavity. However, it was clear that a resonant cavity could be implemented either by structuring the substrate or by engineering an external cavity using the technology developed for the hybrid vertical/planar device structure.

The initial choice of materials encompassed p-(α,ω)-dihexyl-quaterthiophene (DH4T) as p-type material, aluminum tris-quinoline (Alq3) as host material, 4-(dicyanomethylene)-2-methyl-6-(p-dimethylaminostyryl)-4H-pyran (DCM) as lasing compound and α, ω-diperfluorohexyl-4T (DHF4T) as n-type material.

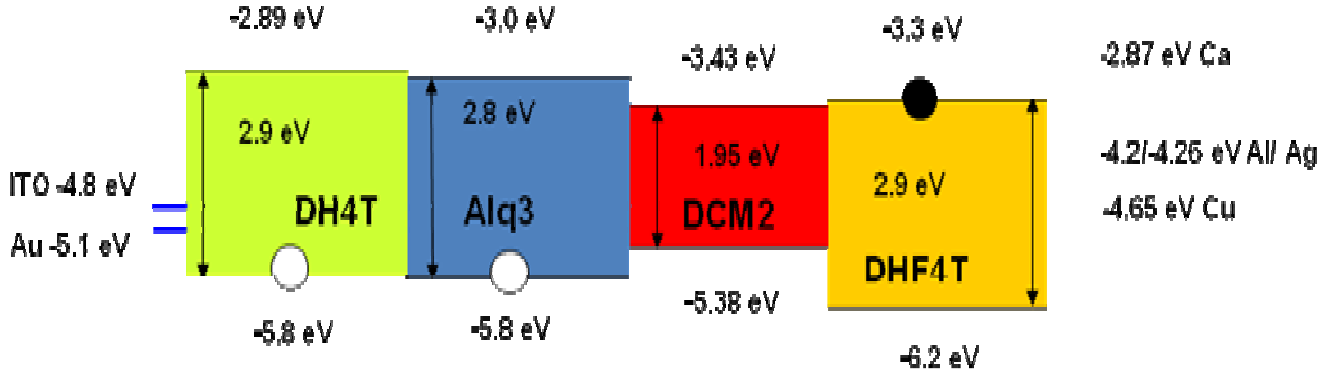

Fig. 2.1.7. Schematic band diagram for an organic heterojunction where the host-guest lasing matrix is formed by a co-evaporated Alq3:DCM layer.

Issues of growth compatibility between DH4T and Alq3, as well as between Alq3 and DHF4T was to be thoroughly evaluated in order to clarify the potential of this heterojunction for providing the targeted high current densities and efficient light emission.

It was clearly highlighted that in all of the device structures targeted by the project one critical aspect was represented by the n-type transport material. This is due to the demanding requested specifications (growth compatibility with underneath layers, high field-effect mobility when grown on other organics, wide bandgap to avoid residual absorption) and to the limited number of available efficient n-type materials.
For this reason, although N,N-ditridecylperylene-3,4,9,10-tetracarboxylic diimide (P13) and α,ω-diperfluorohexyl-4T (DHF4T) were identified as suitable candidates, a continuous monitoring of n-type materials which could fit the specifications and be used in our device structures was performed. The following two classes of materials were considered to be valuable alternatives to the systems currently used in the project for future developments.

Core-Cyanated Rylenes n-type materials

The molecular structure of typical core-cyanated rylenes is reported in Fig. 2.1.8.

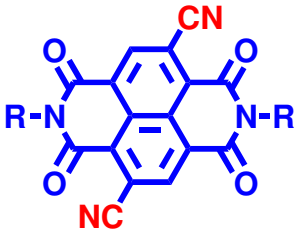

Fig. 2.1.8. Molecular structure of core-cyanated rylenes.

The most relevant characteristics of this material for integration into the OLAS device structures are

its optical gap E_{op} = 3.0-3.2 eV and its mobility that can be as high as 10^{-1} cm^2 V^{-1} s^{-1} [1]. This mobility value is comparable with that of the currently used DHF4T, while the optical gap is higher. Charge mobility, threshold voltage and I_{on}/I_{off} ratio for thin films grown at different substrate temperature are shown in Figure 2.1.9 for the single and double CN substituted compounds.

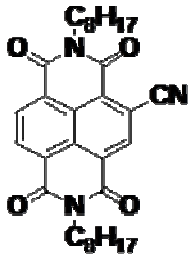

T_d (°C)	μ ($cm^2V^{-1}s^{-1}$)	V_{th} (V)	I_{on}/I_{off}
23	$9.9x10^{-4}$	35 (4)	10^5
70	$2.2x10^{-3}$ ($4x10^{-4}$)	53 (10)	10^4
90	$3.7x10^{-3}$ ($4x10^{-4}$)	34 (4)	10^5
110	$2.5x10^{-3}$	39 (2)	10^5
130	$4.7x10^{-3}$ ($2x10^{-4}$)	28 (2)	10^5

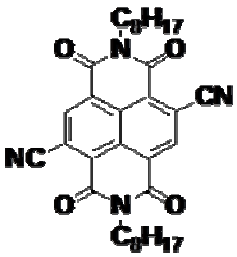

T_d (°C)	μ ($cm^2V^{-1}s^{-1}$)	V_{th} (V)	I_{on}/I_{off}
23	$6.9x10^{-2}$ ($2x10^{-3}$)	-32 (2)	10^2
70	$3.6x10^{-3}$	13 (3)	10^3
90	0.12 (0.007)	-10 (1)	10^3
110	0.15 (0.01)	-37 (2)	10^2
130	0.14	-37 (2)	10^2

Figure 2.1.9. Electrical parameters of core-cyanated rylenes thin films grown at different substrate temperature on HMDS treated SiO_2 dielectrics.

It is clear that in selecting the growth conditions for the best electrical response, the lowest possible threshold voltage has to be chosen. This parameter directly affects the current balance and density that can be injected in the device at an applied voltage. It is also mandatory to pay attention to the film morphology at the selected growth condition as it influences charge transport and interfacial properties with the layers grown on top of it.

Anthracenedicarboximide n-type materials

Another material class with interesting characteristics is the CN substituted anthracenedicarboximide (ADI8-CN_2) [2,3], whose molecular structure is reported below.

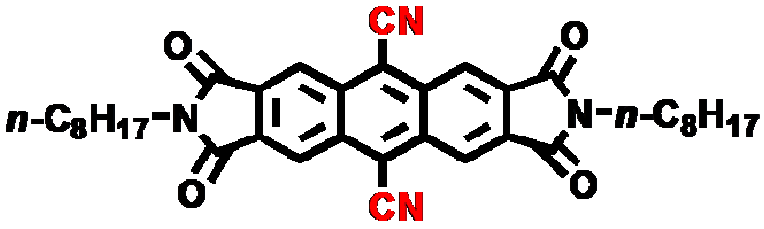

Figure 2.1.10. Molecular structure of CN substituted anthracenedicarboximide.

Field effect transistors based on thin films of ADI8-CN_2 show very high $I_{on/off}$ ratios, n-type mobility on the order of 10^{-2} cm^2 V^{-1} s^{-1} and excellent stability when operated in air.

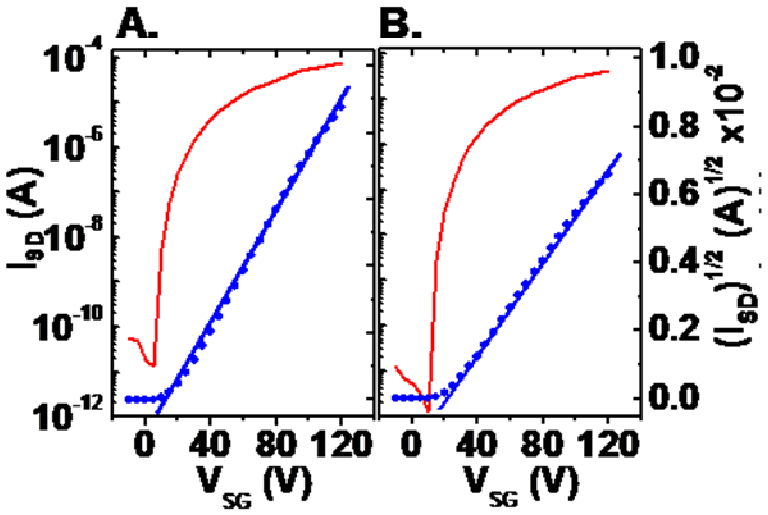

Figure 2.1.11. I-V transfer curves of field effect transistors based on thin films of ADI8-CN_2 measured in vacuum: $\mu = 0.03$ cm^2 V^{-1} s^{-1}, $I_{on/off} = 5 \times 10^6$ (A), and in air: $\mu = 0.02$ cm^2 V^{-1} s^{-1}, $I_{on/off} = 4 \times 10^7$ (B) [3].

The UV-vis absorption spectrum of a thin film (thickness: 50 nm) of ADI8-CN_2 is shown in Figure 2.1.12.

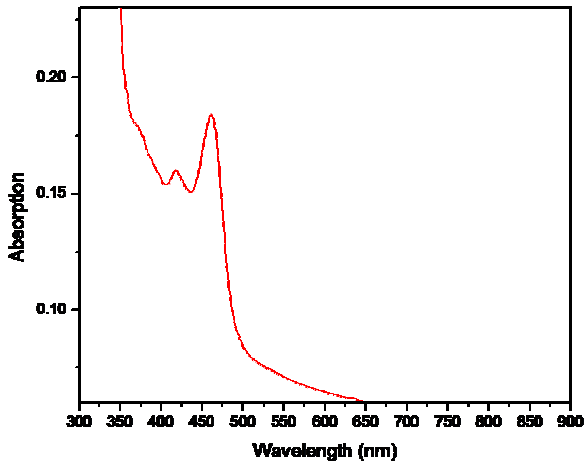

Figure 2.1.12. UV-vis absorption spectrum of a thin film of ADI8-CN_2 with nominal thickness of 50 nm.

A detrimental absorption tail extending in the red down to 650 nm is clearly visible in the spectrum. However, it has to be verified whether the long absorption tail is of electronic origin or rather originates from surface light scattering in the film.

WP1 established the characteristics against which the properties of candidate transport and emitting materials had to be evaluated. A hybrid, as well as a three layer heterojunction, device structure were envisioned as possible alternatives to the fully planar heterojunction approach. WP1 provided input to all other WPs where the actual experimental work was performed.

[1] Facchetti, Marks, Wasielewski et.al. *Chem. Mater.* **2007**, 19, 2703.
[2] Facchetti, Marks et.al. *JACS* **2007**, 129, 15259.
[3] Facchetti, Marks et.al. *JACS* **2007**, 129, 13362.

Table 2.1.1: Deliverables of WP1

Del. no.	Deliverable name	Workpackage no.	Date due (month)	Actual delivery date	Estimated indicative person-months *)	Used indicative person-months *)	Lead contractor
D3	Specifications of n- type and p-type transport materials and phosphorescent compounds	1	M3	M3	4	4	CNR
D4	Specifications of organic heterojunctions	1	M6	M 6	3	3	CNR
D7	Specifications of heterojunction photonic field-effect device structure	1	M9	M9	4	4	CNR

Table 2.1.2: Milestones of WP1

Milestone no.	Milestone name	Workpackage no.	Date due	Actual delivery date	Lead contractor
1	First choice of organic materials for heterojunctions	1	M6	M6	CNR

WP2. Design and modelling (WP leader: IBM)

This workpackage was devoted to model and optimise the photonic and the electrical properties of the device. Special emphasis was given to the design and modelling of the photonic feedback-structure. The choice for a proper device design is made based on the individual properties of the materials used in the heterojunction (WP1) and the available fabrication technology (WP3 and WP5).

Photonic feedback structures with different geometries (vertical, lateral 1D and lateral 2D) were simulated by IBM for the light emitting device built by IMEC (WP5). Optical confinement and losses due to material absorption were modelled and assessed quantitatively. As a result of the simulations, no fundamental preference for either feedback geometry was obtained. Hence, the final selection will exclusively depend on the actual material stack used and the fabrication abilities. The simulations indicate which of the materials in the stack contribute most strongly to the absorption in the resonator and therefore, where alternatives should be considered (feedback to WP1). A general challenge arose to be the intrinsic low optical confinement (of the order of 5%) due to the small material volume with optical gain.

We modelled an optimized quarter wave stack by using a transfer matrix method and calculated the wavelength dependent optical transmission through the dielectric mirror. A device with 10 layer pairs of SiO_2 and TaO_2 is expected to provide a sufficient broad band gap and good reflectivity around the design wavelength of the EML of around 610 nm.

We focused on the question whether there are fundamental advantages of using either a vertical or a lateral optical feedback structure to build an electrically pumped organic laser. For this, we modelled the optical fields and the material properties of the hybrid device developed within OLAS. In this heterojunction design the field effect is exploited in such a way that the metal electrode can be moved away far enough from the optically active region so that its absorption can be neglected in the calculations. For our simulations we used the optical material properties such as the refractive index and the absorption coefficient measured by spectroscopic ellipsometry. To include the absorption in the simulations we fit the complex dielectric functions by multi-oscillator Lorentz models in the interesting wavelength range around $\lambda = 610$ nm.

We study three basic resonator/device geometries shown in Figure 2.2.1. In Figure 2.2.1(a), a vertically oriented laser resonator is formed by two distributed bragg reflectors (DBR) placed below and above the device. Each of the 2 x 10 dielectric inorganic layer pairs consists of 106 nm low refractive index material (SiO_2, n = 1.47) and 74 nm high refractive index material (Ta_2O_5, n = 2.15). Figure 2.2.1(b) displays the unit cell of a photonic feedback structure comprised of extended

ridges providing one-dimensional feedback in the lateral plane. We study ridges consisting of both high and low index dielectric material (Ta_2O_5 or SiO_2). Similarly, the photonic structure may consist of small cylindrical rods of high or low index material. Such a structure is shown in Figure 2.2.1(c) and allows two-dimensional photonic feedback. We chose the lateral size of the periodically repeated unit cells to be 185 x 185 nm in all studied geometries. The vertical size of both the ridges and the cylinders in Figure 2.2.1(b) and 2.2.1(c) is 100 nm. The width of the ridges in Figure 2.2.1(b) is 72 nm (Ta_2O_5 ridges) or 106 nm (SiO_2 ridges). The cylinders in Figure 2.2.1(c) have a diameter of 130 nm (same value for both Ta_2O_5 cylinders and SiO_2 cylinders). The photonic band edge states provide adequate feedback in 1st order. Hence, there is no output coupling but this can be increased to the desired amount by intentionally placing defects in the photonic crystal structure. The resonant cavity modes have high optical intensity inside the gain material. However, the dimensions of the ridges and the cylinders are not fully optimized for the largest possible size of the photonic band gap since this is not relevant for the considerations presented here since we assume linear absorption only.

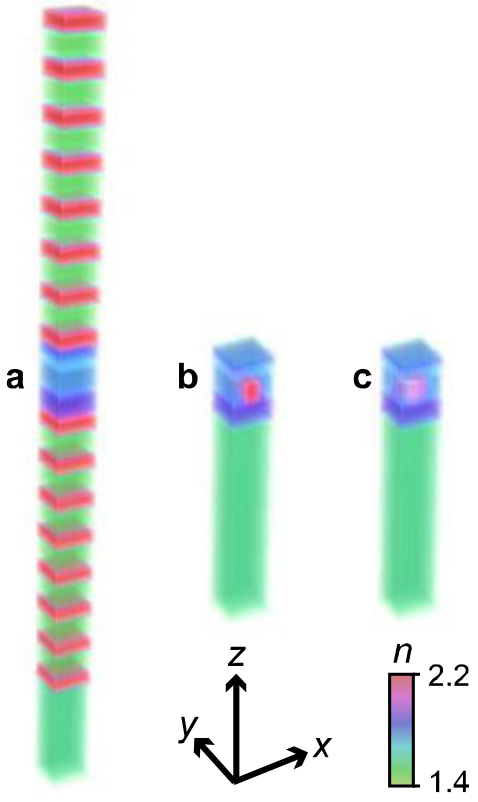

Figure 2.2.1. Three different photonic feedback structures are studied for the IMEC device material stack. The refractive indices are shown color-coded. The organic material system with refractive indices between 1.6 and 1.9 is displayed in blue colors. For the simulations the unit cell which is displayed repeats infinitely in the *x*-*y* plane. a) Vertically oriented laser cavity where feedback and laser emission occurs in *z*-direction. The optical feedback is achieved by pairs of low (green) and high index (red) layers above and below the active region. b) The optical feedback is achieved in the *x*-direction by either a high index (red) or equivalently a low index (not shown) ridge which runs in the center of the unit cell in *y*-direction. The substrate is shown in green below the active region. c) Very similar to b), but the photonic feedback is now achieved by cylindrical rods of high index (red) or equivalently low index (not shown) material. In this configuration two-dimensional optical feedback is possible in the *x*-*y* plane.

A very important figure of merit to evaluate whether an electrically pumped light emitting device will show laser action is the population density N_{th} of excitons at the laser threshold. This number has to be as low as possible in order to admit reaching the lasing threshold before stronger electrical excitation leads to more excitation-induced quenching and ultimately catastrophic device failure. The optical resonator geometry influences the threshold through two important factors: the optical confinement factor Γ and the Q factor of the laser cavity. N_{th} is inversely proportional to both Γ and Q:

$$N_{\text{th}} \propto \frac{1}{\Gamma Q}$$

The confinement factor $\Gamma = \int_{\text{gain volume}} n(\mathbf{r})^2 \left|E(\mathbf{r})\right|^2 d^3\mathbf{r} \Big/ \int n(\mathbf{r})^2 \left|E(\mathbf{r})\right|^2 d^3\mathbf{r}$ corresponds to the electric light field energy contained inside the region with optical gain normalized to the total energy. The quality factor $Q = 2\pi/\lambda\alpha$ is inversely proportional to the cavity loss coefficient α and includes material absorption and output coupling from the resonator.

In Figure 2.2.2, we plot the electric field energy of the light in the resonator as a function of the position inside the vertical laser cavity (corresponding to Fig. 2.2.1(a)) using a one-dimensional finite-difference time-domain (FDTD) simulation. Even without additional transparent spacing layers the gain region of the material stack used in the project is well centred on an intensity anti-node. But due to its small size (25 nm thickness) the resulting confinement factor is only $\Gamma = 0.053$. Since the wavelength of the resonator is slightly off the centre wavelength of the light emission a small increase in the layer thicknesses or an additional spacing layer would be needed in order to fine-tune the resonance of the laser cavity.

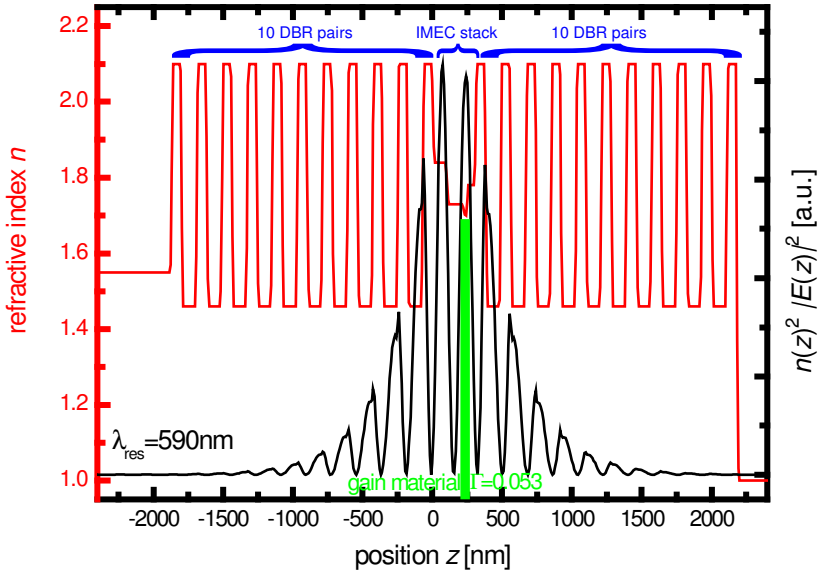

Figure 2.2.2. Simulation of the electrical field energy distribution and calculation of the confinement factor inside the vertically oriented laser cavity (see figure 2.2.1a). The electrical field energy for the resonance wavelength of λ_{res} = 590nm is shown as the black line (right axis). The device stack is located between z = 0 and z = 305 nm and is sandwiched by 10 pairs of DBR mirror layers on each side. The respective refractive indices are plotted as red line (left axis). The location and extension of the gain region is shown as green bar. The electrical field energy contained in this region corresponds to a confinement factor of Γ = 0.053.

In a lateral photonic feedback geometry the optical confinement in the vertical direction is given by total internal reflection because the refractive indices below (i.e. the glass substrate, n = 1.55) and above (i.e. air, n = 1) are lower than those in the organic material stack (n = 1.6-1.9). Figure 2.2.3 shows the electric field energy in a laterally periodic photonic feedback structure (corresponding to Fig. 2.2.1(b) which we obtained by three-dimensional FDTD simulations. While only a vertical cut through the edge of the unit cell is plotted, we calculate the confinement factor for the resonant mode through three-dimensional integration to be Γ = 0.038. This value can be slightly increased to Γ = 0.042 by using high-index Ta_2O_5 (n = 2.1) instead of low-index SiO_2 (n = 1.46) material for the ridges. This value is even lower than the confinement in the vertical resonator configuration because the gain layer is not placed in the field maximum.

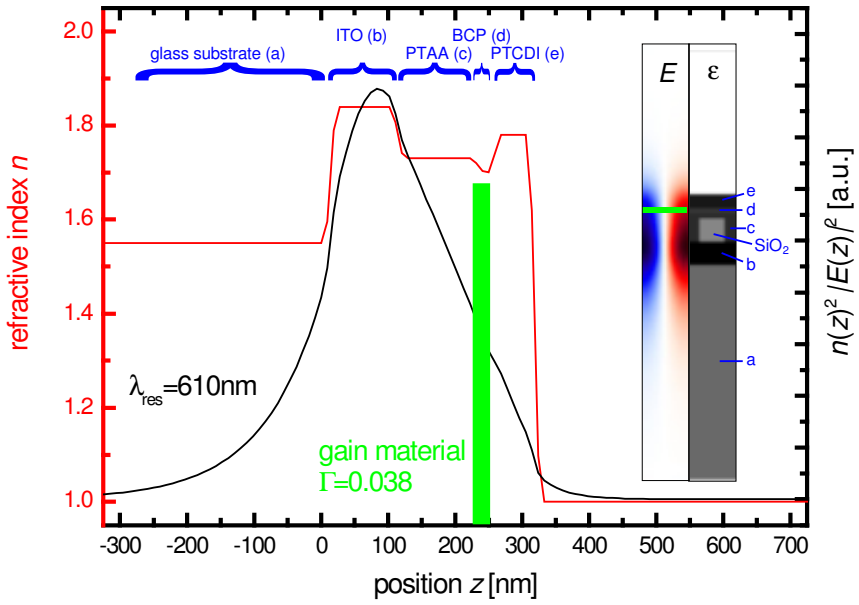

Figure 2.2.3. Simulation of the electrical field energy distribution and calculation of the confinement factor inside the laser cavity with lateral photonic feedback using ridges of low-index material (see figure 2.2.1(b)). The inset on the right shows the electric field distribution (*E* in blue-red colors) and the dielectric constants (ε in grey shades) in a vertical cut through the structure. Corresponding to their refractive index the material stack is displayed in dark grey, the SiO2 ridge in light grey, and the glass substrate in medium grey. The labels correspond to: a) glass substrate, b) ITO (indium-tin-oxide), c) PTAA (Poly(triarylamine)), d) BCP (2,9-dimethyl-4,7-diphenyl-1,10-phenanthroline), e) PTCDI (N,N'-ditridecylperylene-3,4,9,10-tetracarboxylic diimide). The electrical field energy for the resonance wavelength of $\lambda_{res} = 610$nm is calculated at the edge of the unit cell and plotted as black line (right axis). The respective refractive indices are displayed as red line (left axis). The location and extension of the gain region is shown as green bar. The electrical field energy contained in this region corresponds to a confinement factor of $\Gamma = 0.038$.

Since the vertical resonator and the lateral feedback structure with ridges only provide strong optical confinement in one or two dimensions, respectively, we also studied two-dimensional lateral photonic feedback structures using cylindrical rods which enable full three-dimensional confinement. By three-dimensional FDTD calculations we obtain $\Gamma = 0.039$ for the 1st order resonant mode along one of the lateral directions. This value can be slightly increased to $\Gamma = 0.043$ by using high-index Ta_2O_5 ($n = 2.1$) instead of low-index SiO_2 ($n = 1.46$) material.

Table 2.2.1 summarizes the findings for the different photonic feedback structures for the IMEC device material stack. While the vertical resonator seems to be slightly advantageous compared to lateral photonic feedback it should be possible to improve the lateral configuration by positioning the gain layer closer to the intensity maximum inside the cavity by growing a high-index layer above the stack. The confinement in the vertical resonator could also be improved by replacing the ITO anode by a gold anode. However, the very thin gain material layer of only 25 nm thickness poses a general limitation in either design, even more since the actual region with electrically pumped optical gain is likely to be even smaller.

	vertical 10 x DBR (fig. 1a)	**lateral ridge SiO_2 (fig. 1b)**	**lateral rod SiO_2 (fig. 1c)**	**lateral ridge Ta_2O_5 (fig. 1b)**	**lateral rod Ta_2O_5 (fig. 1c)**
confinement factor Γ	0.053	0.038	0.039	0.042	0.043

Table 2.2.1. Optical confinement factor calculated for the different photonic feedback geometries.

Aside the optical confinement, the absorption in the material inside the laser resonator is very crucial in the quest for the electrically pumped organic laser. While the losses due to output coupling from the laser resonator are intended and can be controlled well, there are unavoidable intrinsic absorption losses. The organic heterojunction consists of a stack of materials with a band gap which is only little larger than the one of the emitting material. We performed FDTD simulations in order to address this question. Under strong electrical excitation there will be even more losses because of various additional quenching mechanisms. As these mechanisms are currently not quantitatively accessible for this device, we restrict our calculations to the intrinsic material losses.

In Table 2.2.2 we compare the quality factor of the resonator for each of the photonic feedback configurations shown in Figure 2.2.1. To assess the impact of the relatively strong absorption inside the electron transport layer consisting of PTCDI we perform similar calculations where we set the absorption in the PTCDI to zero. For the vertical resonator this "ideal" electron transport layer results in a dramatic improvement of the *Q* factor while the lateral feedback configurations do not profit as much. In contrast the lateral resonators improve more by additionally replacing the ITO anode with an "ideal" material.

material system	**vertical 10 x DBR (fig. 1a)**	**lateral ridge SiO_2 (fig. 1b)**	**lateral rod SiO_2 (fig. 1c)**	**lateral ridge Ta_2O_5 (fig. 1b)**	**lateral rod Ta_2O_5 (fig. 1c)**
real material absorption	78	203	204	229	229
no absorption in PTCDI	1190	702	704		
no absorption in PTCDI+ITO	2862	17071	45893		
no material absorption	5716	∞	∞		

Table 2.2.2. Comparison of the quality factor calculated for the different photonic feedback geometries. The first row shows the result for the real optical properties of the material stack. For the values in the second row, the strong absorption of the PTCDI layer has been set to zero. In the third row, also the absorption of ITO has been set to zero. In the bottom row, no material absorption at all is included. For the vertical geometry the *Q* factor is a result of the normal cavity losses formed by 10 DBR layer pairs for output coupling. Because of the nature of the first order feedback in the lateral direction, one observes a nearly perfectly vertically guided mode without output coupling and correspondingly a high *Q* factor.

From the comparison of the *Q* factors it can be inferred that there is no intrinsically favourable photonic feedback configuration. It very much depends on the amount and position of absorption losses inside the laser cavity. It was made clear that the use of PTCDI as electron transport layer is a crucial limiting factor.

Modelling of the electrical properties of the planar heterojunction hybrid device.

The electrical properties of the planar heterojunction device and the hybrid field-effect/vertical heterojunction device were also modelled. The electronic and excitonic characteristics of both configurations are simulated using the Silvaco ATLAS two-dimensional device simulator. The simulator solves Poisson and continuity equations, and accounts for a number of processes specific to excitons in OLEDs: exciton formation, exciton lifetime and exciton diffusion.

In Figure 2.2.4 a cross-sectional view of the simulated organic light-emitting field-effect transistor based on a planar heterojunction is shown. The oxide layer on top of the gate is 100 nm thick. Above this dielectric layer an n-type and a p-type semiconductor layer are defined. These two different organic transport layers are depicted in green and red. Both layers have a thickness of 60 nm and overlap each other in the middle of the channel defining a heterojunction. The contacts, injecting the charge carriers, are depicted in gray and are positioned at $x < 1$ µm and $x > 9$ µm.

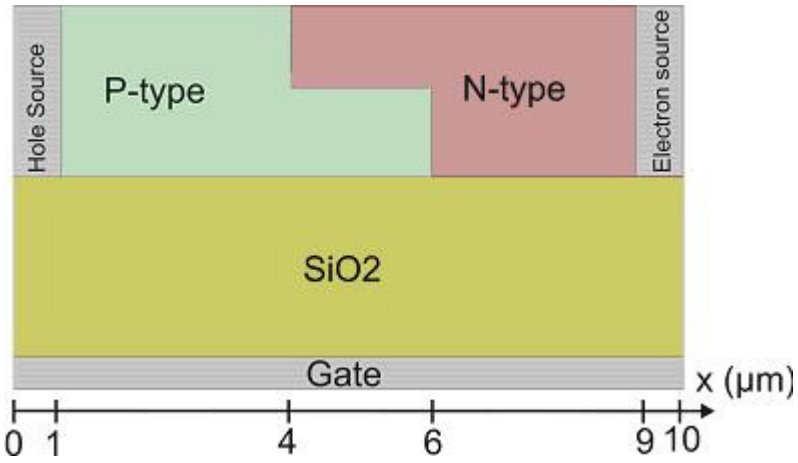

Figure 2.2.4. Cross-section of the simulated organic light-emitting field-effect transistor based on a planar heterojunction.

The traditional nomenclature of source and drain is ambiguous in this type of device, since both electrodes do inject carriers in the organic materials, and neither of them actually drains carriers. Therefore, we will refer to the electrode that injects holes in the p-type semiconductor as the hole source. The hole source is also the electrode that is held at ground potential ($V_H = 0$). The electron

source, at potential V_E, is defined as the electrode that is connected to the n-type semiconductor.

The material parameters used in the simulations are summarized in Table 2.2.3 and correspond to the material parameters of PTCDI-$C_{13}H_{27}$, which is the n-type semiconductor and OOctyl-OPV5, used as p-type semiconductor.

	P-type	N-type
LUMO (eV)	2.9	3.4
HOMO (eV)	5.4	5.4
μ_e (cm^2/Vs)	$1\ 10^{-8}$	$2.5\ 10^{-2}$
μ_h (cm^2/Vs)	$3.5\ 10^{-4}$	$1\ 10^{-8}$
V_T (V)	-15	3

Table 2.2.3. Material parameters used to simulate the organic light-emitting field-effect transistor based on a planar heterojunction.

Figure 2.2.5 shows the experimentally measured as well as the simulated output characteristics of the device. As can be seen, the simulated characteristics nicely fit with the experimentally observed electrical data. The quantitative differences between the measured data and the simulated behaviour can be explained by the fact that the model we used for simulating the device does not incorporate second order effects, such as a gate bias dependent mobility, contact effects, etc.

The characteristics can be qualitatively explained as follows: for a fixed negative gate voltage V_G, holes are injected from the hole source into the p-type material, and a hole accumulation layer is formed. Since the HOMOs of both organic semiconductors are almost equal to each other, holes encounter a negligible barrier at the p-n junction; thus, the hole accumulation layer extends over the complete transistor channel.

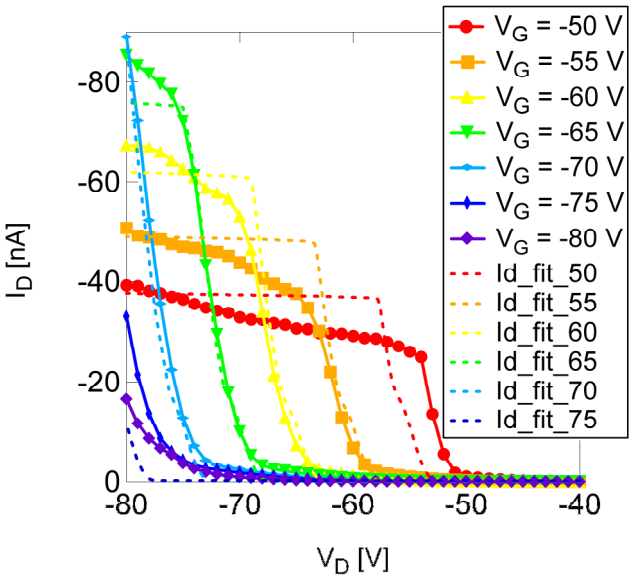

Figure 2.2.5. Electrical characteristics of the device: experimentally measured (solid curves) and simulated (dashed curves).

In a first operation regime, for electron source voltages $|V_E| < |V_G - V_{T,n}|$ (in which $V_{T,n}$ is the threshold voltage of the n-type material), there is only a very low current. Indeed: the hole mobility in the n-type material is low, and in this regime, there are no electrons available yet which the holes can recombine with. As soon as $|V_E| \geq |V_G - V_{T,n}|$, the device enters a second operation regime. Electrons are injected from the electron source into the n-type material, forming an electron accumulation layer. The electron and hole accumulation layers meet somewhere in the channel, and every hole transported from the hole source through the p-type material is expected to recombine with an electron that is carried from the electron source through the n-type semiconductor. The current through the device increases quadratically, as can be expected for any n-type transistor of which V_G and V_D are constant, while V_S decreases. At a certain electron source voltage V_E, the electron current in the n-type material becomes equal to the hole current in the p-type material. From this voltage on, the light-emitting field-effect transistor operates in a third regime. In contrast to previously published light-emitting field-effect transistors [2,3], increasing $|V_E|$ beyond this voltage leads to a saturation of the current. This is explained by the fact that the current in this kind of device is limited by the smallest of the electron and the hole currents. In this third operation regime, the p-type OTFT is in saturation, and its saturated current limits the overall current through the device.

It is assumed that the light emission zone moves within the transistor channel, exactly as was previously described by Zaumseil *et al.* [3]. Figure 2.2.6 clearly illustrates that this is indeed the case. The recombination region moves from right to left (i.e., from the n-region to the p-region) by increasing $|V_E|$ while keeping V_G at a fixed negative value. At a sufficiently negative V_E, the recombination zone is located at the far edge of the n-type material. Electrons face a relatively high injection barrier at the interface with the p-type material. Therefore, the recombination zone does not move further.

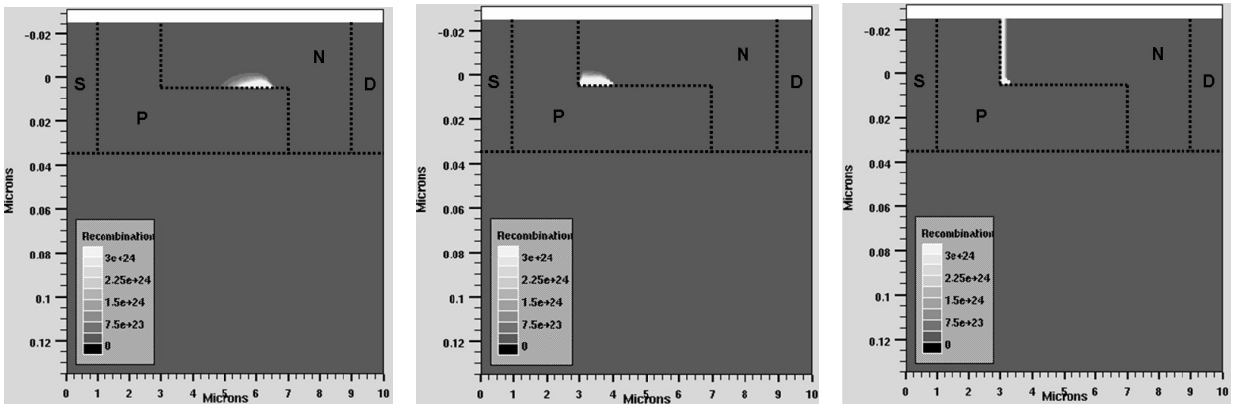

(a) (b) (c)

Figure 2.2.6. Numerical simulations indicate that the recombination zone moves within the transistor channel by increasing $|V_E|$ while keeping V_G at a fixed negative value. (a) V_G=-20V and V_E=-30V, (b) V_G=-20V and V_E=-40V, (c) V_G=-20V and V_E=-45V.

In Figure 2.2.7 a cross-sectional view of the simulated organic light-emitting field-effect device based on a vertical heterojunction is shown. In this case the device utilizes a hole-transport layer (HTL) and a light-emitting electron-transport layer (ETL). The oxide layer is 100 nm thick and covers only the part at $x < 7$ µm of the bottom electrode. On top of this dielectric layer a 50 nm thick p-type semiconductor layer is defined. This p-type layer is depicted in green and is also in contact with the bottom electrode at $x > 7$ µm. An n-type semiconductor layer is then defined on top of the p-type layer. This organic electron transport layer has a thickness of 50 nm and is represented in red. The top-contact is positioned at $x < 1$ µm. So, the distance between the metallic top-contact and the insulator edge is 6 µm.

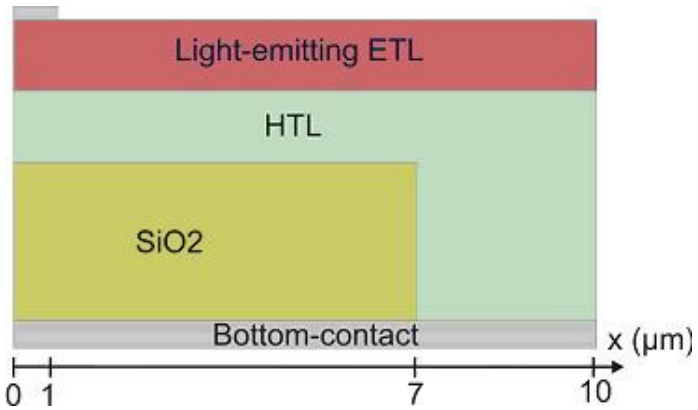

Figure 2.2.7. Cross-section of the simulated organic light-emitting field-effect device based on a vertical heterojunction.

The material parameters used in the simulations are summarized in Table 2.2.4. The light-emitting

electron-transport layer has properties, consisting of experimentally determined field-effect electron mobility for PTCDI-$C_{13}H_{27}$, reported HOMO and LUMO levels for PTCDI-$C_{13}H_{27}$ [1], and typical values (for OLEDs) for radiative singlet lifetime and exciton diffusion length of $16x10^{-9}$ s and 10 nm respectively [4]. The material parameters of the hole transport layer correspond to the material parameters of PTAA. The high LUMO of PTAA prevents electron injection; holes on the other hand can easily overcome the small energy barrier between both HOMO levels resulting in exciton formation in the light-emitting transport layer.

	HTL	Light-emitting ETL
LUMO (eV)	1.8	3.4
HOMO (eV)	5.1	5.4
μ_e (cm^2/Vs)	$1\ 10^{-7}$	$2\ 10^{-2}$
μ_h (cm^2/Vs)	$5\ 10^{-3}$	$5\ 10^{-4}$
τ (s)		$16\ 10^{-9}$
L_{diff} (nm)		10

Table 2.2.4. Material parameters used to simulate an organic light-emitting field-effect device based on a vertical heterojunction.

Figure 2.2.8 shows the experimentally measured as well as the simulated output characteristics of the device. As can be seen, there is a good agreement between the simulated characteristics and the experimentally observed electrical data.

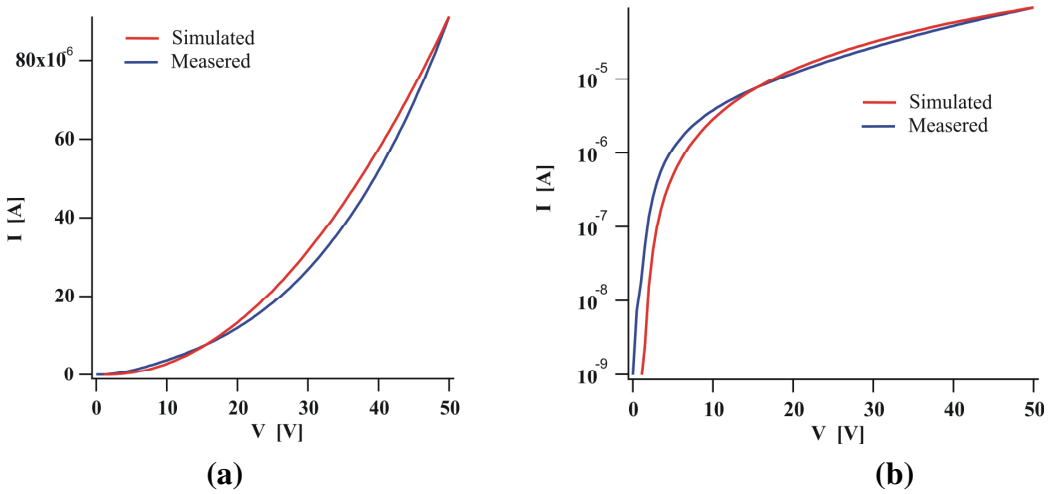

Figure 2.2.8. Experimentally measured (blue curves) and simulated (red curves) electrical characteristics of the planar heterojunction device: (a) linear plot and (b) logarithmic plot.

The simulated recombination zone as the result of applying a positive bias to the anode is illustrated in Figure 2.2.8. It can be clearly seen that the recombination of excitons occurs near the insulator edge, several microns away from the metallic cathode, thereby reducing the optical absorption losses. Simulations also show that the position of the recombination zone does not change under different bias conditions. In other words, light-emission always occurs at the insulator edge,

irrespective of the applied bias.

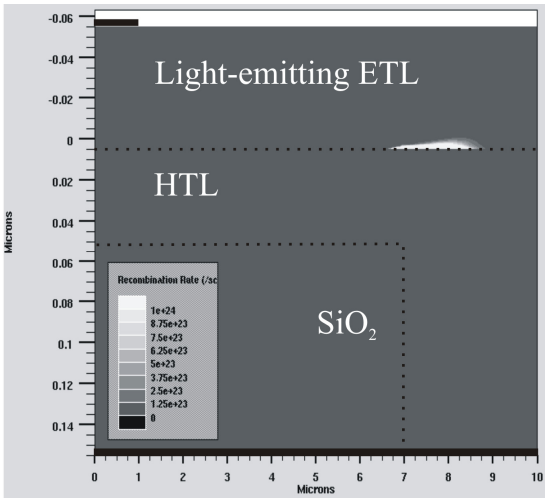

Figure 2.2.9. The numerical simulated recombination zone. Light-emission occurs always near the insulator edge, irrespective of the applied bias.

Numerical simulations also show that it is important to position the metallic top-contact as close as possible to the insulator edge. This is illustrated in figure 2.2.10. The smaller the distance is between the top contact and the insulator edge, the higher the obtained current and therefore the higher the intensity of the emitted light. However, the metallic top-contact may not be deposited too close to the insulator edge to prevent optical absorption.

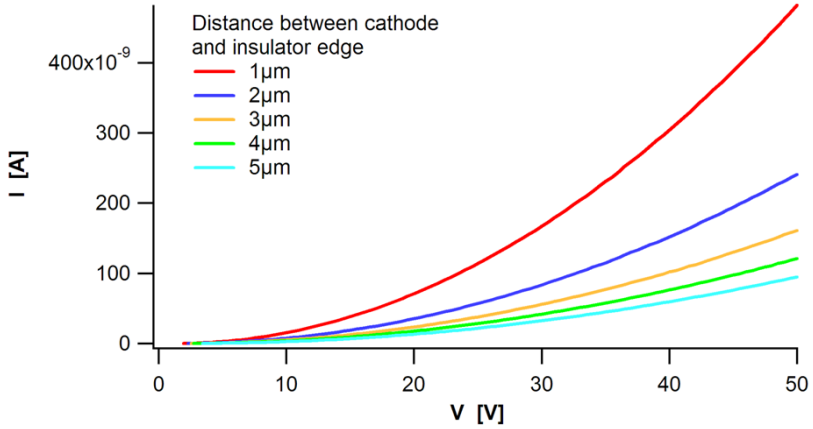

Figure 2.2.10. Simulated electrical characteristics of the vertical heterojunction device for different positions of the metallic top-contact. The highest current is obtained when the metallic top-contact is positioned at 1 µm distance from the insulator edge.

Design of a novel hybrid approach with organics and silicon-on-insulator technology for photonic feedback structures

A novel approach where absorptive electrodes built from doped semiconductor material serve the need for charge carrier injection as well as implementing a photonic cavity was introduced. This

hybrid organic/inorganic concept readily allows the integration of organic lasers with silicon- on-insulator technology important for future applications. As shown in Figure 2.2.11, the novel approach is implemented by two linear or curved arrays of high-refractive-index semiconductor blocks or cylinders on a transparent substrate which is coated with the organic layers. The working principle requires proper engineering of phase shifts and total internal reflection inside the high-index arrays in order to realize a laser resonator with sufficiently high Q-factor even with absorptive building blocks such as doped Si.

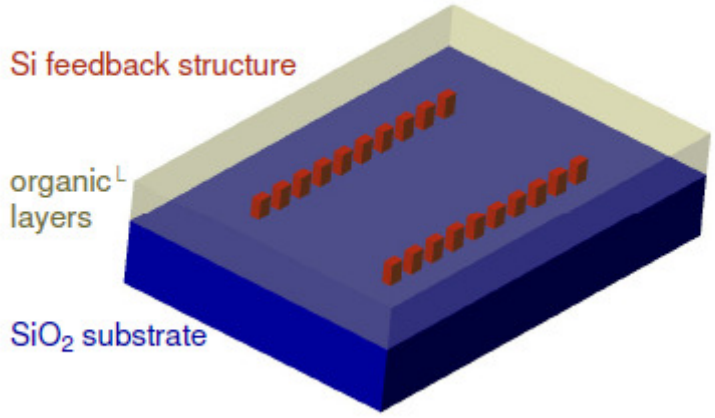

Figure 2.2.11. Illustration of the novel hybrid approach with organics and silicon-on-insulator technology. The doped Si acts as photonic feedback structure and as electrodes for current injection into the organic layer.

Figure 2.2.12 shows 3D finite-difference time-domain (FDTD) simulations of the structure. The distance between the arrays is on the order of 1.8 microns and yields a Q-factor >150 at 500 nm resonance wavelength. Increasing the lasing wavelength (e.g. to 640 nm using DCM2, see D25) reduces the absorption losses by a factor of 4 which should further increase the Q-factor.

Figure 2.2.12. Ab-initio calculations (3D finite-difference time-domain method) of a Fabry-Perot cavity implementing the hybrid concept. The electric field in the direction of the shown arrow (= polarization of the source which excites the cavity) is plotted. The silicon blocks are shown as black lines. The green area in the cross sectional view denotes the organic layer.

In a first step, no electrical contacts are connected to the arrays of semiconductor blocks in order to first demonstrate optically pumped lasing on the basic structure. Yet, the architecture may easily be extended towards the integration of larger electrodes and contact pads through which a driving current can be applied, as illustrated in Figure 2.2.13.

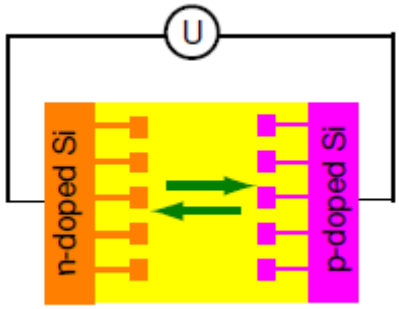

Figure 2.2.13. In this schematic top view of a Fabry Perot resonator, the two gratings comprise n- and p doped Si which offers a high electrical conductivity. The gratings are connected by small ridges with a length on the order of a few optical wavelengths to larger electrodes (doped Si or metal). By applying a voltage to the electrodes charges can be injected into the active organic layer (shown in yellow).

References:

[1] C. Rost, D. J. Gundlach, S. Karg, and W. Rieß, *J. Appl. Phys,* **2004***, 95*, 5782
[2] C. Rost, S. Karg, W. Rieß, M.A. Loi, M. Murgia and M. Muccini, *Synth. Met.* **2004**, *146*, 237
[3] J. Zaumseil, R.H. Friend and H. Sirringhaus, *Nat. Mater.* **2006**, *5*, 69
[4] I. Sokolik, R. Priestley, A.D. Walser, R. Dorsinville and C.W. Tang, *Appl. Phys. Lett.* **1996**, *69*, 4168

Table 2.2.5. Deliverables of WP2

Del. no.	Deliverable name	Workpackage no.	Date due	Actual delivery date	Estimated indicative person-months *)	Used indicative person-months *)	Lead contractor
D5	Modelling of photonic feedback structures compatible with field-effect transistors	WP2	M6	M6	4	4	IBM
D8	Design heterojunction photonic field-effect device structure	WP2	M12	M12	4	4	IBM

D14	Modeling of electrical properties of heterojunction field-effect devices	WP2	M15	M15	2	2	IBM

Table 2.2.6. Milestones of WP2

Milestone no.	Milestone name	Workpackage no.	Date due	Actual delivery date	Lead contractor
M2	Design of photonic feedback structures	WP2	M6	M6	IBM
M5	Simulation of photonic heterojunction device structure	WP2	M15	M15	IBM

WP3. Technology for photonic structuring (WP Leader: AMO)

The technology development and fabrication of inorganic photonic structures embedded in a photonic layer stack was performed in WP3. Different photonic feedback structures were realized in SiO_2 (n = 1.457) and in the high refractive index material Ta_2O_5 (n = 2.1). The design and the precise geometrical dimension of the photonic feedback structure were defined jointly by the partners. The preparation of layouts, lithography and etching steps have been carried out by AMO.

Design and fabrication of linear grating resonators in SiO_2

Linear grating resonators with variable geometrical dimensions have been realized in SiO_2. A flexible lithography technology with high throughput is mandatory to ensure that for any organic material precise designed resonators structure can be realized. Interference Lithography allows a much more efficient fabrication of different linear gratings compared to Imprint Lithography, because we avoid that for all tested organic materials and hence for many different resonator dimensions suitable templates for the imprint process have to be fabricated.

Large area linear gratings have been realized with laser interference lithography (IL). The exposures were carried out on 1.8 µm thick SiO_2 layers thermally grown on Si substrates. A two layer resist consisting of **b**ottom **a**nti **r**eflection **c**oating (BARC) layer to suppress substrate reflectance and a chemical amplified resist was used. The desired line widths of the gratings were achieved by exact adjustment of the exposure dose. First, in cooperation with IMEC distributed feedback resonators

(DBR) suitable for characterisation of the benchmark system MLPP with line to space ratio of 1:1 were realized. The line width of the linear grating was 160 nm and the pitch was adjusted to 325 nm. The resist structures are shown in figure 2.3.1 after development.

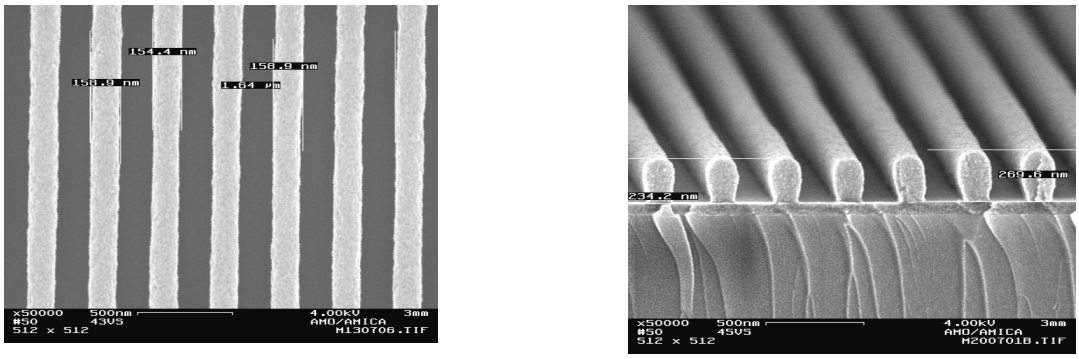

Figure 2.3.1. Top view (left side) and cross sectional (right side) SEM micrograph of the 160 nm wide lines realized by IL.

Different gratings with different line width and pitch have been realized. In cooperation with CNR two types of gratings with 200 nm and 207 nm line width have been fabricated. The pitch was 400 nm and 414 nm, respectively. These gratings are used as second order resonators (m=2) for host-guest systems having the final emitting wavelength in the red at about 630 nm.
Further, second order linear gratings with lines to space ratio of 1:3 were desired on Si substrates with 1.8 µm SiO_2 on top. The design consists of 240 nm wide lines with a separation of 80 nm. For fabrication of these types of gratings EBL has been used. The exposures have been performed with a Leica EBPG5000 system. To ensure accurate electron beam lithography on the insulating substrates a 40 nm thick Ti layer has been deposited as intermediate layer between the SiO_2 surface and the electron sensitive resist. The Ti layer prevents charging during the exposure and acts as a hard mask for the following etching processes. To resolve the quite small space of 80 nm between the 240 nm wide lines an EBL process with high contrast value is mandatory. The negative tone electron sensitive resist HSQ (Hydrogen Silsesquioxane), prebaked at moderate temperature and developed in concentrated TMAH has fulfilled this requirement. As shown in figure 2.3.2, in a 200 nm thick HSQ resist layer clearly resolved 80 nm trenches between the 240 nm wide lines are observed.

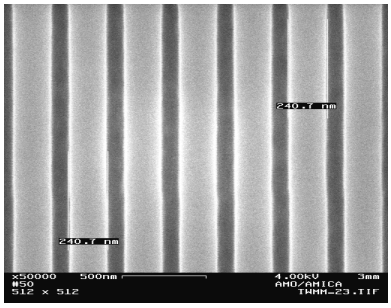

Figure 2.3.2. Top view SEM micrograph of a linear grating in HSQ with lines to space ratio of 1:3.

After the lithography steps the resist patterns have been transferred into the SiO_2 in a dry etching process. The etching has been performed in an inductively coupled plasma reactive ion etching (ICP-RIE) tool. In a first step the BARC layer of the samples exposed by IL has been etched in an O_2 plasma and the Ti layer of the samples realized by EBL in a BCl3 chemistry based etching process. After these first steps the main etching process based on C_4F_8 and He chemistry has been applied, where the lithographically defined structures have been transferred into the SiO_2 layer. Depending on the actual design of the pattern a precise adjustment of many process parameters like ICP / RF power, C_4F_8 /He mixture, etching temperature etc. is necessary to achieve a satisfying etching result. As an example for the dimensional stability of the optimized etching process two SEM micrographs of completely fabricated gratings are shown in figure 2.3.3. On the left hand side a grating with 200 nm desired line width and on the right hand side a grating with 207 nm desired line width are shown. The deviation between the designed pattern size and the realized pattern size is in the range of a few nm.

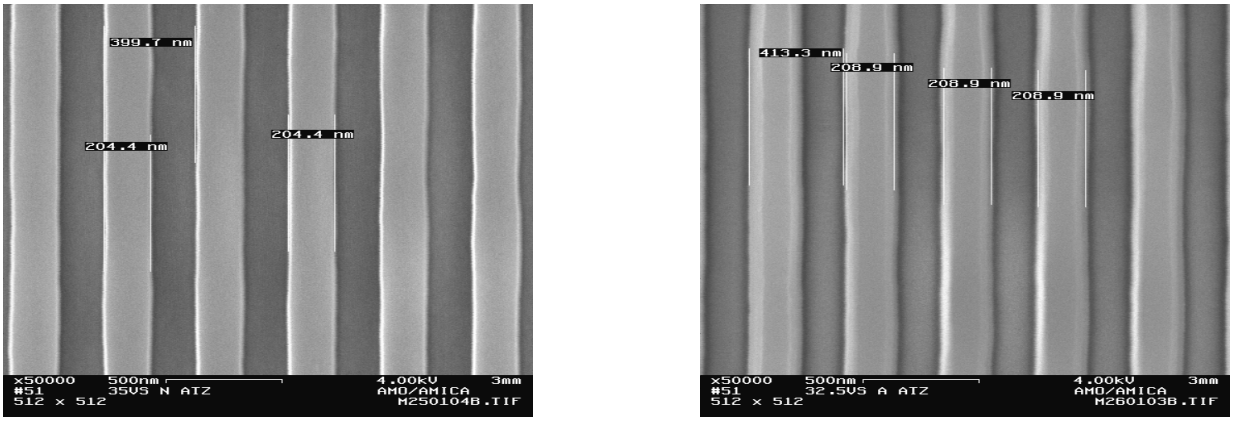

Figure 2.3.3. SEM micrograph of two fully fabricated linear grating resonators in SiO_2.

Figure 2.3.3 demonstrates the potential of IL and ICP etching to fabricate defined linear gratings with a line width accuracy of a few nm. Further, IL allows the fast production of large area gratings with a wide range of line widths ranging from 80 nm to 500 nm. This flexibility made the IL the lithography technology of choice for OLAS, where many different materials were to be tested.

Beside the dimensional stability between the lithographic and the etched structures the steepness of the etched structure is a quality mark of the etching process. To determine the profile of the gratings the cross section was investigated in a SEM. For the gratings shown in figure 2.3.4 a profile angle of better than 80° was determined.

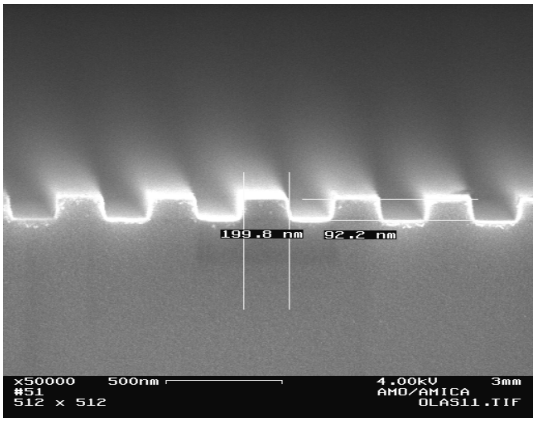

Figure 2.3.4. Cross sectional SEM micrograph of a 90 nm deep etched linear grating resonator

Additional distributed feedback resonators (DBR) with a line to space ratio of 1:1 were realized. The line width of the linear grating was 200 nm and the pitch was adjusted to 400 nm. In the second run, a linear grating was fabricated with slightly wider lines and a pitch of 210 nm. The resist structures for both resonators are shown in figure 2.3.5 after development.

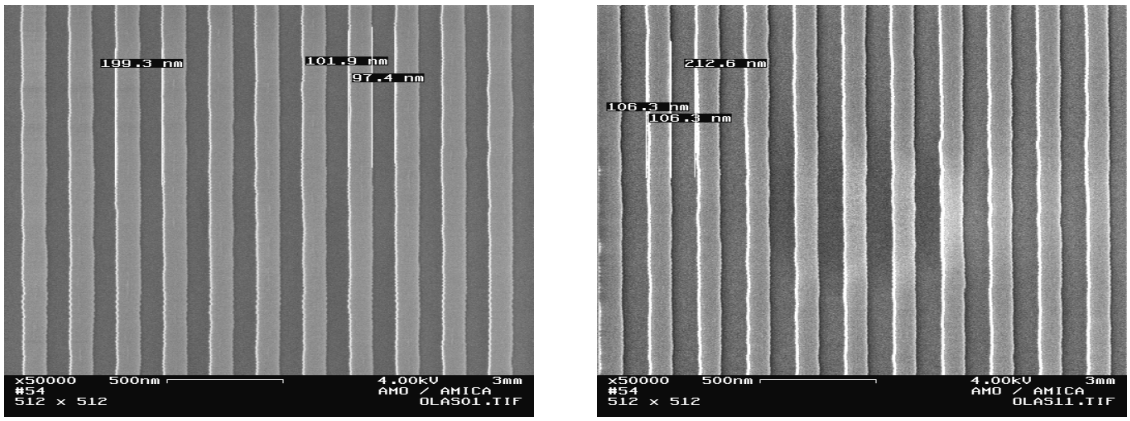

Figure 2.3.5. Top view SEM micrographs of the 100 nm (left) and 106 nm (right) wide lines realized by IL.

After performing the lithography the resist patterns were transferred into the SiO_2 in a reactive ion etching process. For the IMEC resonators an etch depth of 50 nm was realized. For the CNR resonators with 400 nm pitch an etch depth of 90 nm and for the resonators with 414 nm pitch an etch depth of 250 nm was desired. The etching was done using an inductively coupled plasma reactive ion etching (ICP-RIE) tool. In the first step, the BARC layer of the samples was etched using O_2 plasma. The main etching process for SiO_2 is based on C_4F_8 and He chemistry. A precise adjustment of the process parameters like ICP / RF power, C_4F_8 /He mixture, etching temperature etc. is necessary to achieve a satisfying dimensional stability between the lithographic and transferred structures and to achieve anisotropic etch profiles. To determine the quality of the

etching process the cross sections of the etched gratings were investigated using a scanning electron microscope (SEM). For the test grating shown in figure 2.3.6 a steep profile is observed. Even after etching for 200 nm, the SiO_2 still had a residual resist layer that was 315 nm thick. Furthermore, the thin intermediate BARC layer can be seen in figure 2.3.6.

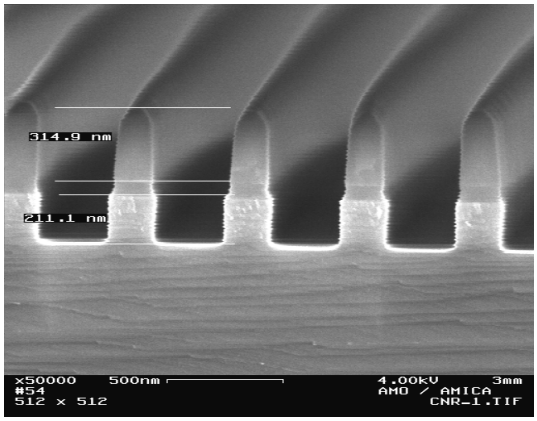

Figure 2.3.6. Cross sectional SEM micrograph of a 200 nm deep etched linear grating with residual IL resist and BARC layer on top.

Resonator structure in Ta_2O_5

AMO developed a sputter process for the deposition of Ta_2O_5 layers and a reactive ion etch process. Further, a high resolution electron beam lithography processes was transferred onto this material. Working with Ta_2O_5 material was a big challenge for AMO because at the start of OLAS no experiences were existing with this material. After development of a direct sputtering process the first optical characterizations of Ta_2O_5 layers by IBM revealed promising results. Indeed, only low losses of the propagating light were observed. After these positive observations the development of the lithography and etching processes was started.
To fabricate feedback structures in Ta_2O_5 three key process modules had to be developed and optimized:

- Deposition of thin Ta_2O_5 layers
- Definition of test and feedback structures by electron beam lithography (EBL)
- Transfer of the electron beam defined resist features into the Ta_2O_5 layer

Subsequent to the development of these modules functional devices could be fabricated by integrating all modules into a full fabrication process flow.

Deposition of thin Ta_2O_5 layers

First, sputter deposition of thin Ta_2O_5 films was investigated. Ar was used as the process gas. RF power was set to 700 W and chamber pressure was preset to be $5 \cdot 10^{-3}$ mbar. A detailed optical

characterization of Ta_2O_5 layers indicates low scattering losses and a homogenous deposition of the layers. As shown in figure 2.3.7, the refractive index determined with spectroscopic ellipsometry exhibits the expected dispersion. The values, however, appear higher than in the literature. No specific absorption bands appear within the spectral range shown in figure 2.3.7.

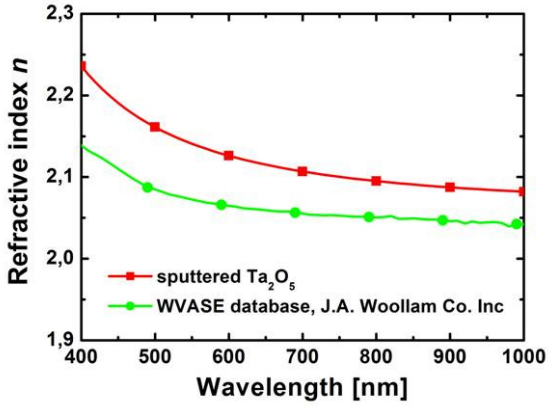

Figure 2.3.7. Refractive index of sputtered Ta_2O_5 layers as a function of the wavelength.

Definition of test structures by EBL and RIE etching

Nanoscale structures in Ta_2O_5 were defined by EBL. A Vistec EBPG-5000 system operating at 100 kV was used to expose hydrogen silsesquioxane (HSQ), a negative tone resist material. Due to its high resolution, low surface roughness and good process control, HSQ is an ideal resist for process development and evaluation.

Using a high contrast development process based on high concentrated tetra-methyl ammonium hydroxide (TMAH) sub-20 nm resist features could be fabricated, as shown in figure 2.3.8.

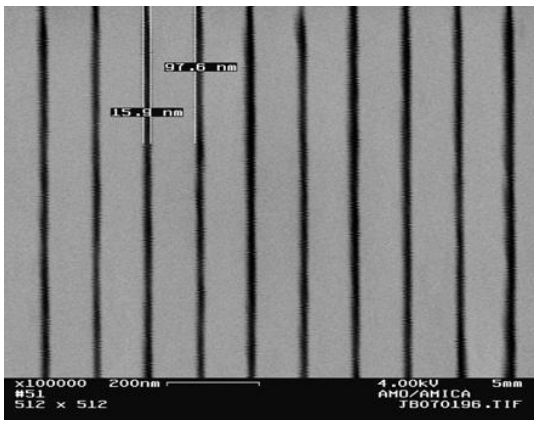

Figure 2.3.8. Top view of 16 nm wide HSQ resist lines on Ta_2O_5.

The profile of HSQ lines was investigated very carefully. Steep resist profiles are mandatory for a

reliable evaluation of the performance of the subsequent etching process. The SEM cross section micrograph presented in figure 2.3.8 demonstrates typical resist features with a steep profile. A line width of 40 nm and an aspect ratio of about 5 were realized.

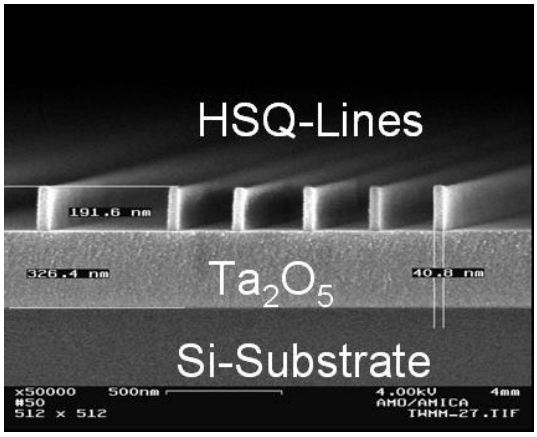

Figure 2.3.9. Cross sectional view of HSQ resist lines on Ta_2O_5.

The HSQ structures were used as masks to develop a reactive ion etch process for the Ta_2O_5 layers. Dry etching of the Ta_2O_5 layers was carried out using an Oxford Plasmalab 100 ICP-RIE tool.

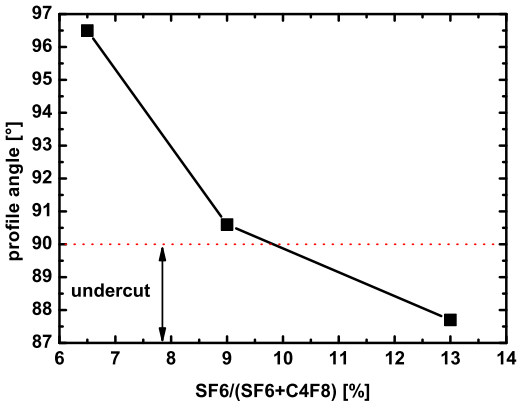

Figure 2.3.10. Profile angle as a function of SF_6 admixture.

The process is based on SF_6/C_4F_8 chemistry and uses high inductively coupled plasma (ICP) and low radio frequency (RF) power. The observed etching profile steepness depends strongly on the ratio of the SF_6 to the C_4F_8 content. In figure 2.3.10 the profile angle is plotted as a function of the SF_6 percentage of the total flow. The C_4F_8 content was kept constant for these investigations. For low SF_6 concentration a tapered etch profile with a profile angle greater than 90° was investigated. A profile angle greater than 90° means, that the line width at the top of the line is smaller compared to the bottom of the line. By increasing the SF_6 concentration, steeper profiles were achieved and for a SF_6 admixture of 11 sccm an optimized profile angle of 90° was realized. Further increase of the SF_6 flow leads to bowing etch profiles with a profile angle below 90°. In this case the line width

at the top of the line is larger compared to the bottom of the line. To demonstrate the quality of the fabrication process, a test pattern consisting of four 25 nm wide lines etched to a depth of 100 nm into a 325 nm thick Ta_2O_5 layer using this optimized dry etch process is shown in figure 2.3.11.

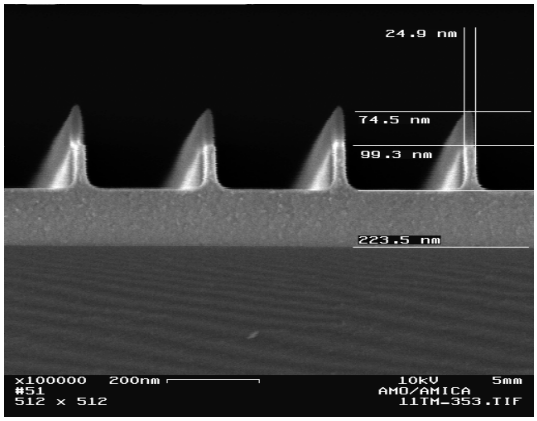

Figure 2.3.11. SEM micrograph of 25nm wide lines in Ta_2O_5.

Fabrication of functional photonic devices

Subsequent to the development and optimization of the key process modules a full fabrication process flow for photonic devices was developed. Silicon substrates covered with an additional 1.8 µm silicon dioxide layer were used as base material. A 30 nm thick Ta_2O_5 layer was deposited on top of this base stack. For the fabrication of photonic feedback structures EBL was carried out using a positive tone resist material, ZEP520a. The resist pattern was transferred into the Ta_2O_5 layer with the optimized SF_6/C_4F_8-based reactive ion etching process. A SEM micrograph of a mixed first and second order feedback structure is shown in figure 2.3.12 (left) and a close up of the second order structure consisting of holes with a diameter of 210 nm and a pitch of 300 nm is shown in figure 2.3.12 (right).

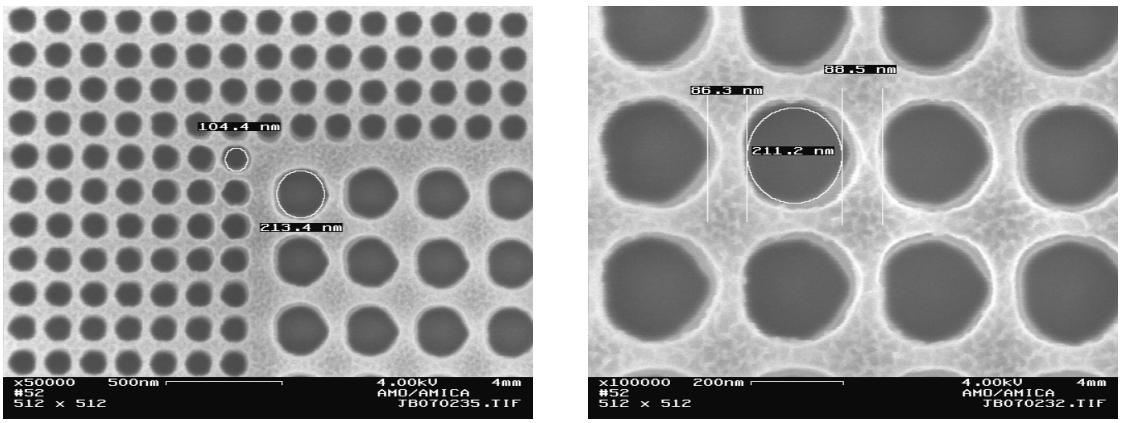

Figure 2.3.12. Ta_2O_5 photonic feedback structure.

The periodic structure is designed to be of second order leading to vertical emitting devices. The periodicity and dimensions of the holes were chosen to achieve laser emission at 495 nm. Square pads with side lengths of 100 µm were fabricated. In a final step, the polymer gain material methyl-substituted ladder-type poly(para-phenylene) (MeLPPP) was spin coated over the structures by IBM.

Realization of the newly designed photonic feedback structures integrating organics and silicon-on-insulator technology

The novel hybrid approach for photonic resonators introduced in WP2, where absorptive electrodes built from doped semiconductor material serve the need for charge carrier injection as well as for implementing a photonic cavity was realized.

In order to realize the delicate dimensions and required fabrication precision the structures were exposed with electron beam lithography in hydrogen silsesquioxane (HSQ) and were subsequently transferred with a HBr-based reactive ion etching process to the silicon-on-insulator substrate. Figure 2.3.13 shows a scanning microscope image of a curved laser resonator. All processing steps including the spin-coating of the organic gain layer on top of the structure consisting of the ladder-type polymer MeLPPP were finalized.

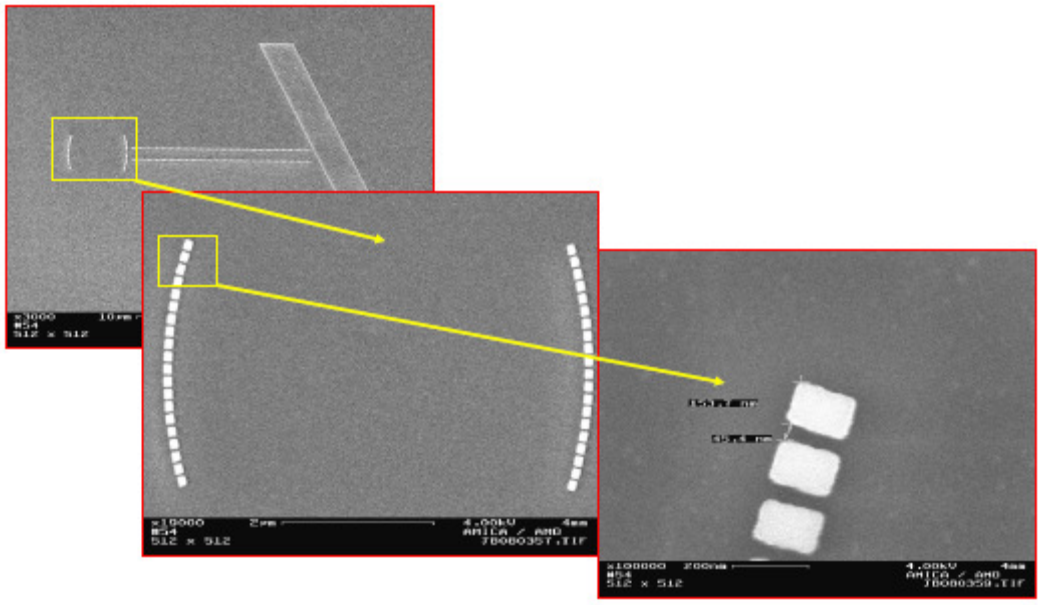

Figure 2.3.13. Scanning electron micrograph of a micro-resonator defined with electron beam lithography in HSQ resist on SOI.

Table 2.3.1: Deliverables of WP3

Del. no.	Deliverable name	Workpackage no.	Date due	Actual/Forecast delivery date	Estimated indicative person-months	Used indicative person-months	Lead contractor
D9	Fabrication of photonic feedback structures compatible with field effect devices	WP3	M12	M12	11	16	AMO

Table 2.3.2: Milestones of WP3

Milestone no.	Milestone name	Workpackage no.	Date due	Actual delivery date	Lead contractor
M.3	Fabrication of the photonic feedback structure	WP 3	M12	M12	AMO

WP4. Photonic characterization (WP leader: RWTH)

The main objectives of this WP are:

- To perform the linear optical characterization of photonic nanostructures
- To image the organic field-effect heterojunctions
- To characterise the optically pumped laser in organic heterojunctions

The task of linear optical characterization was focussed on the experimental evaluation of the optical properties of photonic waveguide structures to be used in the final electrically pumped organic laser device. A technical analysis of waveguide losses was performed in presence of different contact materials for the case of the organic light emitter methyl-substituted ladder-type poly(para-phenylene) (MeLPPP), which is known to be a very efficient laser material and qualifies for an ideal test system. The influence of the contacting materials on the photonic properties of the organic waveguide was analyzed by a complementary analysis of amplified spontaneous emission (ASE) thresholds and waveguide propagation losses.

A series of samples, based on a 150nm thick MeLPPP film were prepared. As contact materials, indium tin oxide (ITO) and aluminium are used respectively as hole injecting and electron injecting

electrode. The photonic properties of the following multilayer slab waveguide samples were investigated:

a) MeLPPP (150nm) on glass substrate
b) MeLPPP (150nm) / ITO (20nm) / glass
c) MeLPPP (150nm) / ITO (100nm) / glass
d) Al (100nm) / MeLPPP (150nm) / ITO (20nm) / glass

The measurements were carried out in an experimental setup where the pump beam, delivered from a femtosecond regenerative amplifier, is elliptically focussed onto the sample by means of a cylindrical lens. Waveguide losses are analyzed by monitoring the edge emitted light generated in the organic layer via ASE where the pump spot was gradually moved away from the waveguide edge. As the output intensity from the end of the excitation stripe is constant, observed decreases in the edge emitted signal result from waveguide losses (mainly absorption and scattering) within the unpumped region. According to the known relation $I(z) = I_0 \cdot \exp(-\alpha z)$, where I_0 is the light intensity at z=0, the waveguide loss coefficient α can be determined. In addition to the direct loss analysis, the ASE threshold was determined for each sample. As the gain of the light emitting MeLPPP material itself does not depend on the adjacent contact layers, deviations of the ASE threshold in the different waveguide samples are an indirect measure of the waveguide losses – although the amount of light guided in the organic layer experiences changes in a multilayer stack. To support the analysis, additional simulations of the mode profile in the slab waveguide samples were carried out which include considerations of the modal filling factors in the gain medium.

ASE thresholds were determined for each fabricated sample by recording emission spectra in dependence on excitation fluences per pulse. The emitted intensity at the peak wavelength (λ = 495 nm) is determined for each sample and displayed in Figure 2.4.1. Obviously, edge emitted PL- and ASE-intensities depend linearly on the excitation fluences. Above the ASE threshold, we observe the characteristic abrupt increase in the output signal slope efficiency. We determine the lowest ASE threshold of 3 $\mu J/cm^2$ in sample (a), i.e. for the case of a bare MeLPPP film on the glass substrate. A 20 and 100 nm thick ITO layer sandwiched between the organic film and the substrate results in an increase of the ASE threshold to 8 and 34 $\mu J/cm^2$, respectively. An additional Al layer on top of the organic film further increases the ASE threshold to 69 $\mu J/cm^2$. Note, that all the samples are optically pumped from the back side, i.e. through the glass substrate. By this means, strong absorption of the pump light at the metallic Al layer can be neglected for the comparison between the samples.

a) b)

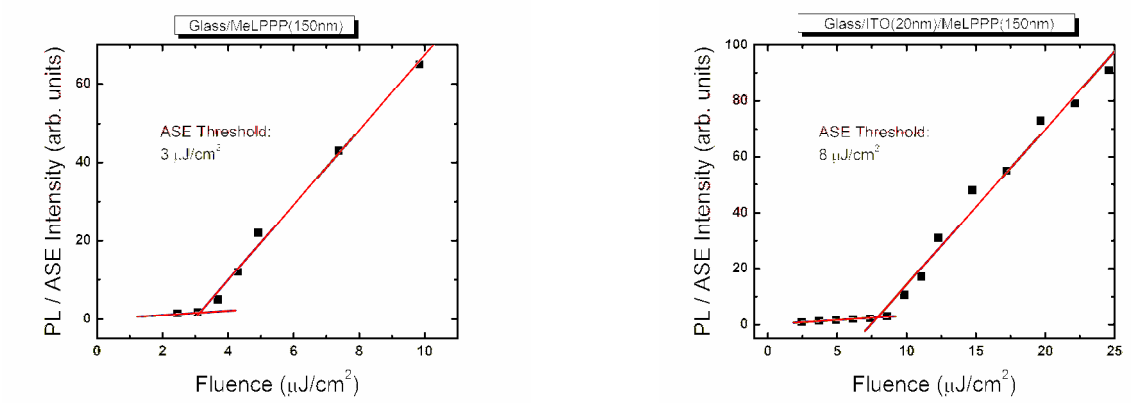

c) d)

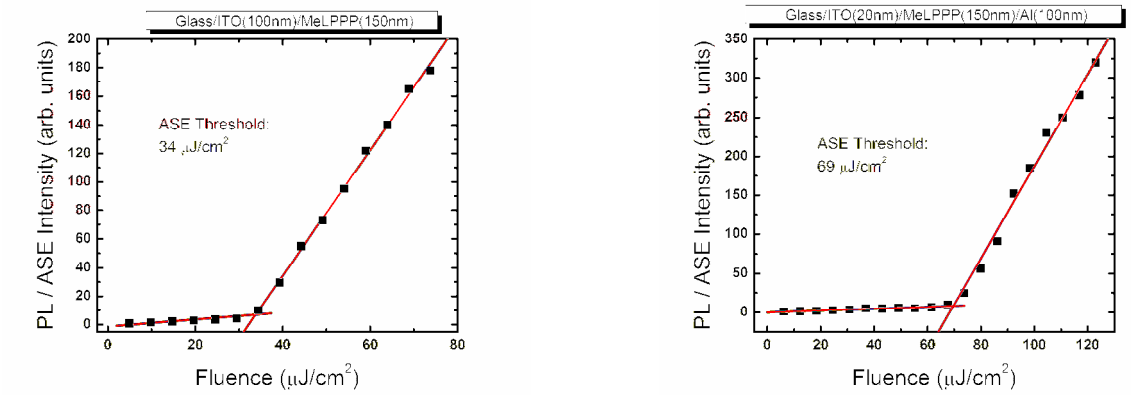

Figure 2.4.1. ASE threshold measurements of different MeLPPP waveguide samples (a) to (d).

One can expect that the observed increase in ASE threshold is based on a reduction of the modal filling factor in the gain medium (reduced gain) and/or the extension of the waveguide modes into the absorbing contact layers (increased waveguide losses). Loss measurements, carried out by the experimental technique introduced above, provide information about the propagation of light in the unpumped region of the waveguide and therefore allow for the assessment of the loss coefficient in the absence of gain. The results of these loss measurements are shown in Figure 2.4.2. For each sample the laser fluence was chosen above its respective ASE threshold. The graphs depict the edge emitted light intensity at λ_{ASE} = 495 nm as a function of the stripe distance from the waveguide edge. The data were fitted by an exponential decay function (red solid lines) to extract the effective waveguide loss coefficients for the different layer stacks.

Waveguide structures comprising absorbing layers adjacent to the organic layer showed a significant increase in loss coefficients. The lowest waveguide losses of 5.3 cm^{-1} are observed for the bare MeLPPP film on the glass substrate (sample (a)). The additional ITO layer sandwiched between the organic film and the substrate increases the waveguide losses to 10.6 and 23.6 cm^{-1} for

the 20 and 100 nm ITO thicknesses, respectively. The Al layer on top of the organic waveguide increases the measured waveguide loss to the largest value of 47.6 cm^{-1}.

a) b)

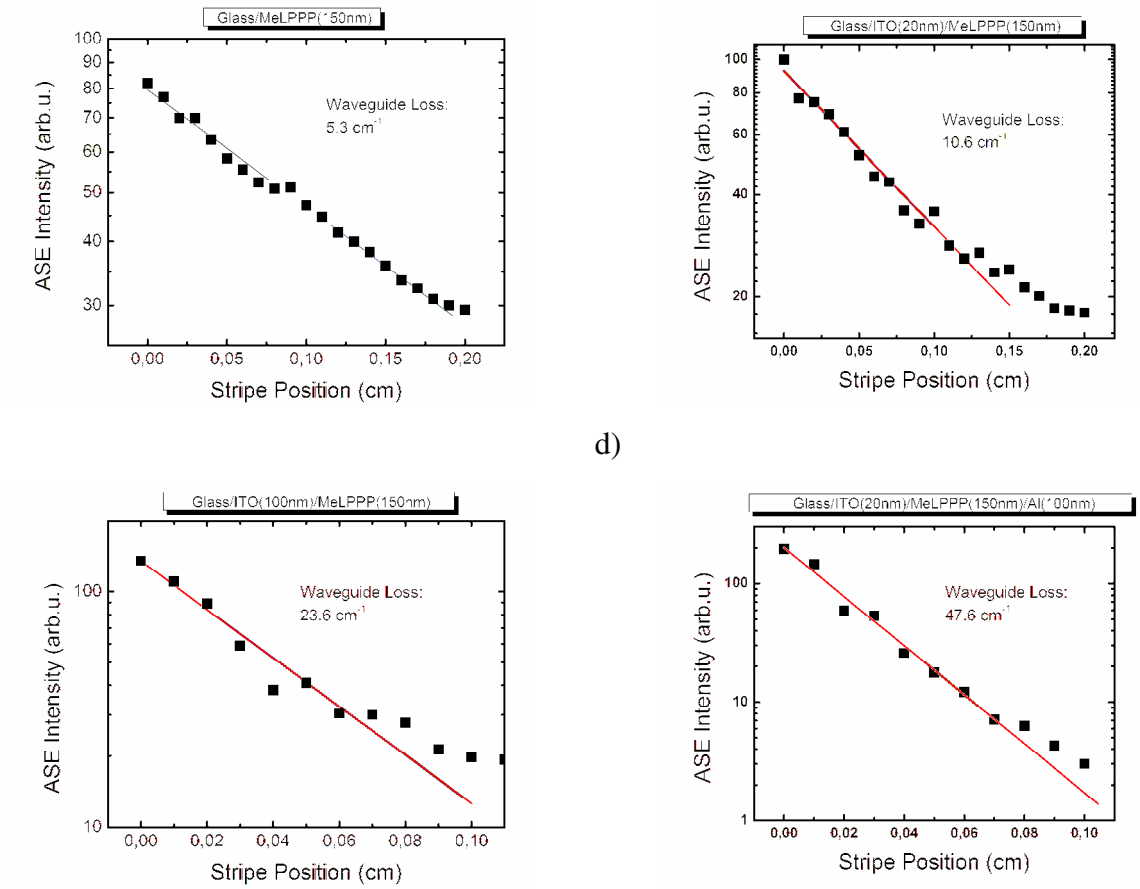

Figure 2.4.2. Propagation loss measurements carried out for MeLPPP waveguide samples (a) to (d).

For a further evaluation of these results, we considered them in context with the light propagation modes in the different structure. To this end, the intensity profile for beam propagation along the structure was simulated using a 2-dimensional beam propagation simulation tool. The optical constants of the involved materials were derived from ellipsometry measurements. The amount of light guided within the active organic layer is represented by confinement factor Γ which is extracted from these simulations.

Table 2.4.1 summarizes the measured ASE thresholds and waveguide losses of the investigated samples: higher ASE thresholds are qualitatively accompanied by increased waveguide losses. In addition the calculated filling factors are listed for each waveguide sample.

Sample	ASE threshold	loss coefficient	Filling factor
MeLPPP/glas	3 μJ/cm^2	5.3 cm^{-1}	50 %
MeLPPP/ITO(20nm)/glass	8 μJ/cm^2	10.6 cm^{-1}	53 %
MeLPPP/ITO(100nm)/glass	34 μJ/cm^2	23.6 cm^{-1}	30 %
Al/MeLPPP/ITO/glass	69 μJ/cm^2	47.6 cm^{-1}	37 %

Table 2.4.1. Measured ASE thresholds and loss coefficients of the investigated slab waveguide samples. Simulated filling factors of the waveguide mode in the emitting organic layer are additionally shown.

Two factors can be discussed with respect to their role on either lasing threshold or propagation losses. The losses of a certain structure are mainly determined by the percentage of light, which is guided within the lossy ITO and Al layers. For the ASE threshold, the amount of light which is guided within the active MeLPPP film (confinement factor) has to be taken into account, as only here amplification takes place.

A comparison between the samples (a) and (b) shows that compared to the bare MeLPPP film the 20 nm thin ITO film decreases the filling factor only very slightly. Consequently, the increase in ASE threshold for sample (b) can be ascribed to increased waveguide losses in this waveguide structure. Increasing the ITO thickness to 100 nm (sample (c)) results in a decrease of the filling factor from about 50 to 30 %. In addition, the amount of light guided in the ITO layer strongly increases. Compared to sample (a), the ASE threshold increases by one order of magnitude while the measured waveguide losses increase by only a factor of 4-5. Hence, the interplay between filling factor and waveguide losses increase the ASE threshold for this sample. Sample (d) exhibits both the largest ASE threshold and waveguide loss coefficient accompanied by a small filling factor.

In conclusion, the investigation pointed out that a strong effect of the contact materials on the ASE threshold is to be expected.

The task of imaging organic heterojunctions was carried out by partner CNR by first employing laser scanning confocal microscopy on a heterojunction system comprising DH4T and P13. The electrical characteristics of double layer heterojunction structures were investigated within WP6. In order to explain the observed variations in the electrical performances between the DH4T/P13 and P13 /DH4T heterojunctions a morphological analysis of the layered structures was performed. Laser scanning confocal microscopy (LSCM) was employed, in which samples are scanned with a laser

and the resulting photoluminescence (PL) is collected. The advantage in using this technique is that the laser excitation penetrates inside the device channel allowing the observation not only of the outermost but also of buried layers. From the PL images one can then deduce the morphological characteristics of the various interfaces. LSCM images of DH4T/P13 and P13/DH4T combinations are displayed in Figure 2.4.3.

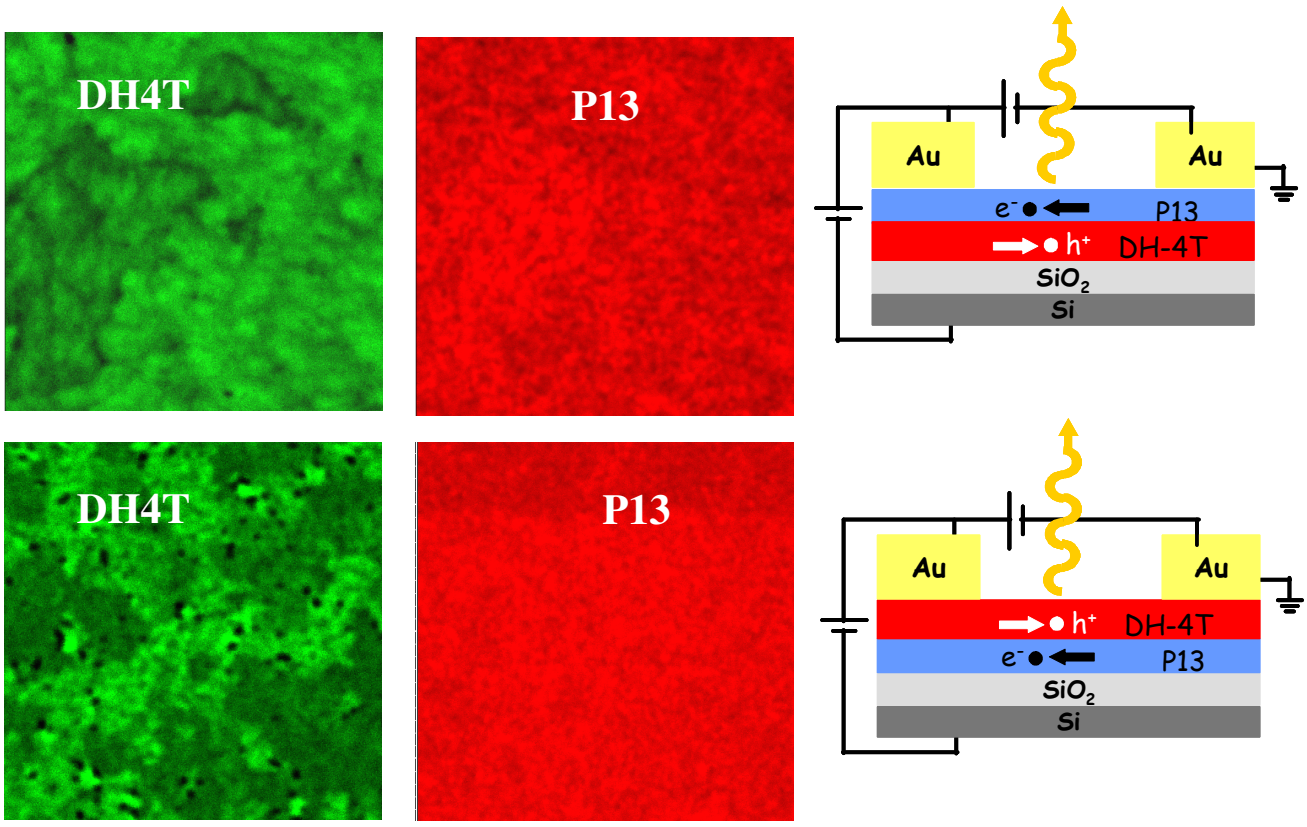

Figure 2.4.3. Laser Scanning Confocal images of DH4T and P13 layers relative respectively to DH4T/P13 and P13/DH4T heterojunctions.

It is evident that, while forming a continuous film on the bare silicon substrate, DH4T films are discontinuous when deposited on P13. The morphology appears to be web-like with empty holes. We conclude that the lack of film continuity is at the origin of the worsening of electron transport in P13/DH4T devices (see WP6). The P13 film, instead, was substantially unaffected by the fact that the substrate was SiO_2 or DH4T layer. These data indicate that the material choice in order to form smooth and continuous organic/organic interfaces is not trivial and that optimum properties are not necessarily obtained by employing the best performing materials in single layer configurations.

As a second step in the task of imaging organic heterojunctions CNR investigated field-effect transistor structures based on three layer vertical organic heterojunctions formed by DHF4T as n-type material, Alq3:DCM as host-guest light emitting system and DH4T as p-type material. It is

extremely important to understand how the morphology of bottom layers affects the subsequent morphology of the upper layers and to determine the optimum growth conditions of each layer to be used for device fabrication. The morphology of each layer within the organic heterojunction was investigated in relation to growth parameters such as film thickness, deposition rate and substrate temperature.

The base samples that we investigated comprised either SiO_2 or ITO followed by an insulating layer of PMMA. The first organic layer of α,ω-diperfluorohexyl-4T (DHF4T), which is used as the n-type transport layer, was grown at two different thickness on top of the PMMA layer (Figure 2.4.4 (a)). Figure 2.4.4 (b) is a 10x10μm AFM image of a 15 nm thick DHF4T layer that was grown at a rate of 0.5 Å/s at room temperature. The image shows that there is a large amount of 3D growth covering the majority of the surface. The 3D structures have a range of heights from 100-180 nm. Next, a similar sample was made by adjusting the DHF4T layer thickness to 5 nm (the rate and temperature remained constant). Figure 2.4.4 (c) is a 10x10μm AFM image of the 5 nm thick DHF4T layer. The image shows that there is still some 3D growth even with a reduction in the sample thickness. When the two images are compared, one can distinctly see that by decreasing the film thickness from 15 nm to 5 nm, there is a significant decrease in the amount of 3D growth.

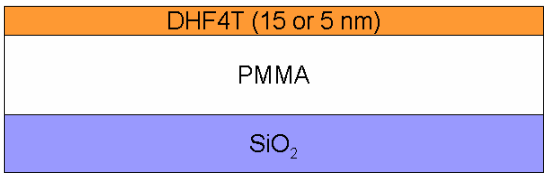

a)

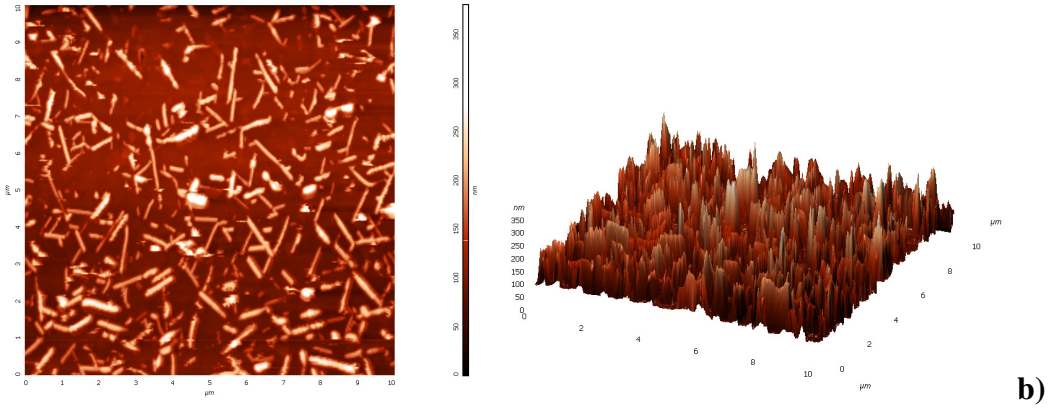

b)

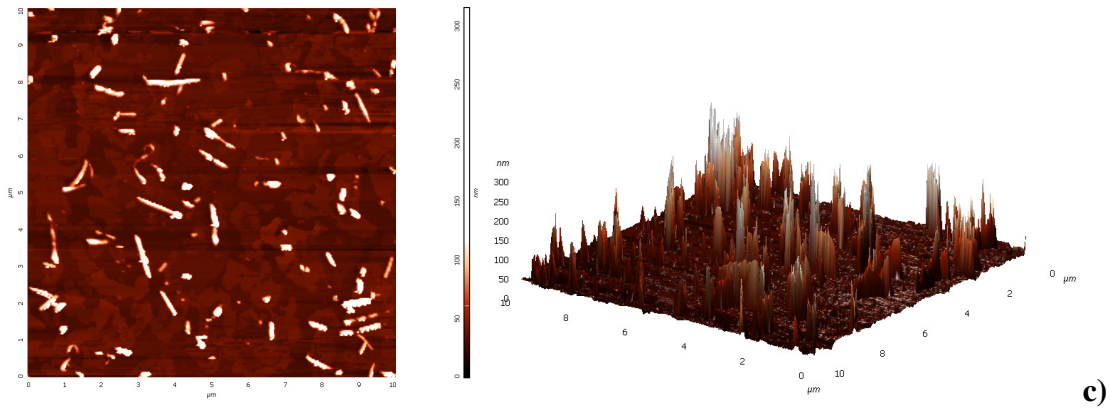

c)

Figure 2.4.4. (a) Schematic structure of the investigated sample structure. 10x10µm AFM images and 3D images of (b) DHF4T layer that is 15 nm thick, (c) DHF4T layer that is 5 nm thick. Both samples are grown on top of PMMA and had a growth rate of 0.5 Å/s at room temperature.

Since the first layer can affect the morphology of the following layers, it is important to reduce the amount of 3D growth from the DHF4T layer in order to obtain a more flat morphology. Therefore, the effects of changing the growth rate and temperature of the DHF4T were investigated next. Figure 2.4.5 (a) is an image of a DHF4T film grown at a slower rate (relative to the sample in figure 2.4.4 (c)) of 0.2 Å/s at room temperature. The image shows 3D growth all over the sample surface. The heights of the 3D structures ranged from 80-200 nm in height. Next, figure 2.4.5 (b) shows a DHF4T film grown at an even slower rate of 1 Å/min and at a lower temperature of -150 °C. When the two images are compared, a significant reduction in the 3D growth is observed when the temperature and rate were decreased.

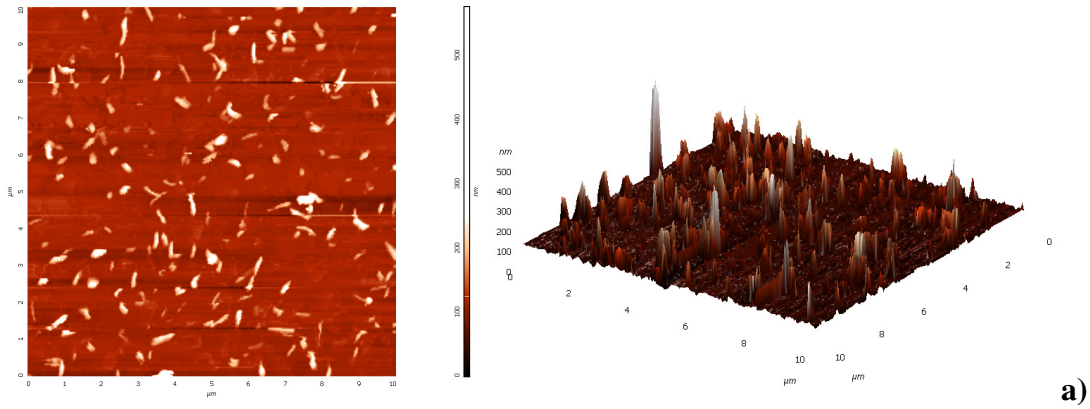

a)

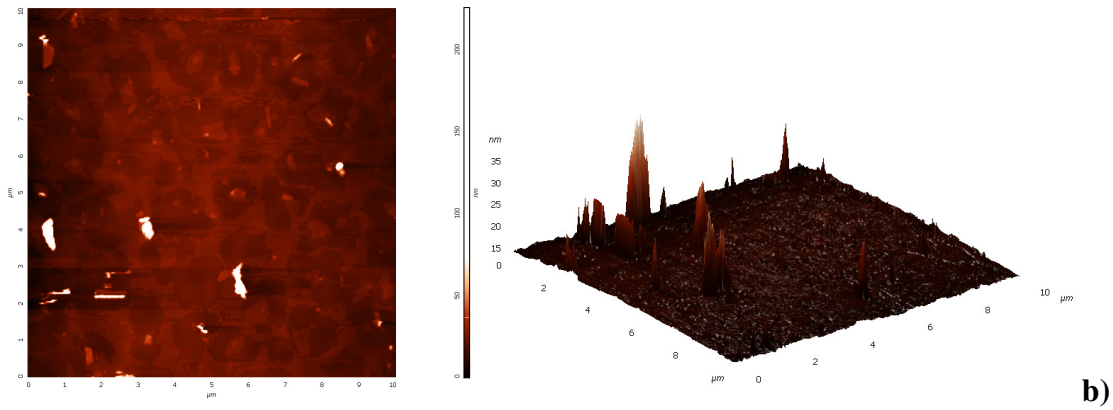

Figure 2.4.5. 10x10µm AFM images and 3D images of (a) DHF4T layer (7 nm) grown at 0.2 Å/s at room temperature, (b) DHF4T layer (4 nm) grown at 1 Å/min at -150 °C.

The next layer of the device that is grown on top of DHF4T is the lasing host-guest layer made up of an Alq3:DCM 5% mixture.

The Alq3:DCM layer was grown on top of a DHF4T layer at a rate of 2 Å/s with a total layer thickness of 20 nm at room temperature (Figure 2.4.6 (a)). The DHF4T layer was 7 nm thick and had a growth rate of 0.2 Å/s at room temperature (Figure 2.4.5 (a)), which are the parameters used for the device fabrication. Figure 2.4.6 (b) is a 2x2µm AFM image of the morphology of the Alq3:DCM 5% layer on top of DHF4T.

Next, the rate of deposition of the Alq3:DCM 5% layer was investigated in order to determine if a slower deposition rate affected the morphology, as it did with DHF4T. Figure 2.4.6 (b) as discussed above, is an image of Alq3:DCM 5% grown at a 2 Å/s rate and figure 2.4.6 (c) is an image of an Alq3:DCM 5% layer on DHF4T that was grown at a slower deposition rate of 0.2 Å/s. The film in figure 2.4.6 (c) has 3D growth that has heights on average of ~75 nm and a range of widths. When the two images in figure 2.4.6 are compared, the images do not show a distinct difference in the morphology. Since the morphology did not significantly change with slower deposition rate, it was concluded that growth rate does not affect the morphology of the Alq3:DCM 5% layer.

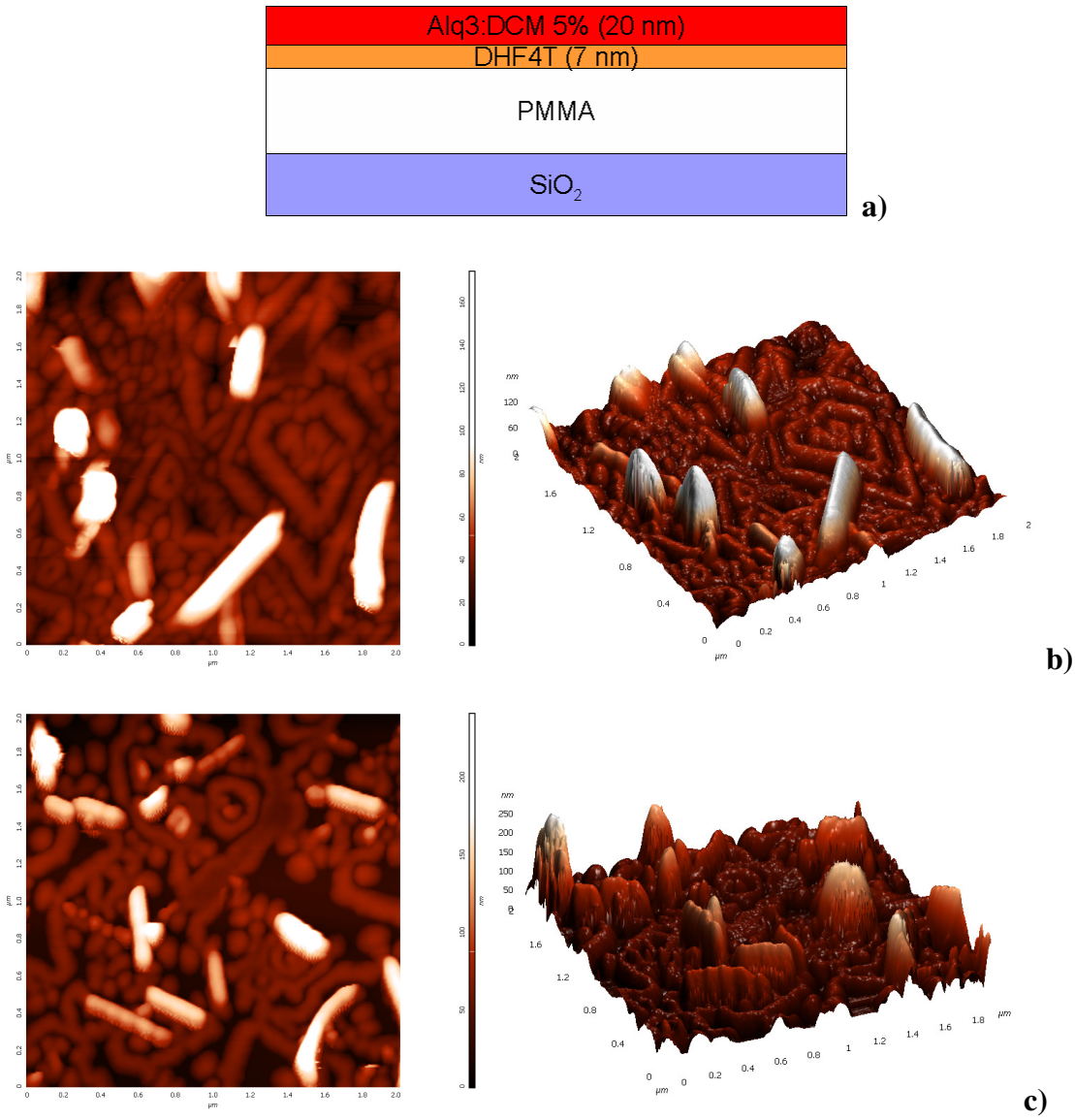

Figure 2.4.6 (a) Schematic of the sample structure of Alq3:DCM 5% on top of DHF4T. 2x2µm AFM images of (b) Alq3:DCM 5% grown on DHF4T with 3D image. Growth rate was 2 Å/s at room temperature and the total thickness was 20 nm, (c) Alq3:DCM 5% grown on DHF4T with 3D image. Growth rate was 0.2 Å/s at room temperature and the total thickness was 20 nm.

The final organic layer in the heterojunction is DH4T, a p-type transport material. The sample had the following structure: SiO_2 or ITO/PMMA/DHF4T (0.2 Å/s, 7nm, RT)/Alq3:DCM 5% (2 Å/s, 20nm, RT)/DH4T (0.2 Å/s, 30nm, RT)/Au electrode (Figure 2.4.7 (a)). The DH4T's morphology was measured in the device's channel, since this is the device's active region. Figure 2.4.7 (b) and (c) show two AFM images of the DH4T layer in two different devices, made the same way but on different substrates: SiO_2 and ITO. The images show that there is still some residual 3D growth from the underlying DHF4T layer, and where there is no 3D growth a more rough morphology is observed. The heights of the larger features range from 100-200 nm and have widths ranging from

200-400 nm. The area without 3D growth had an average roughness of 50 nm.

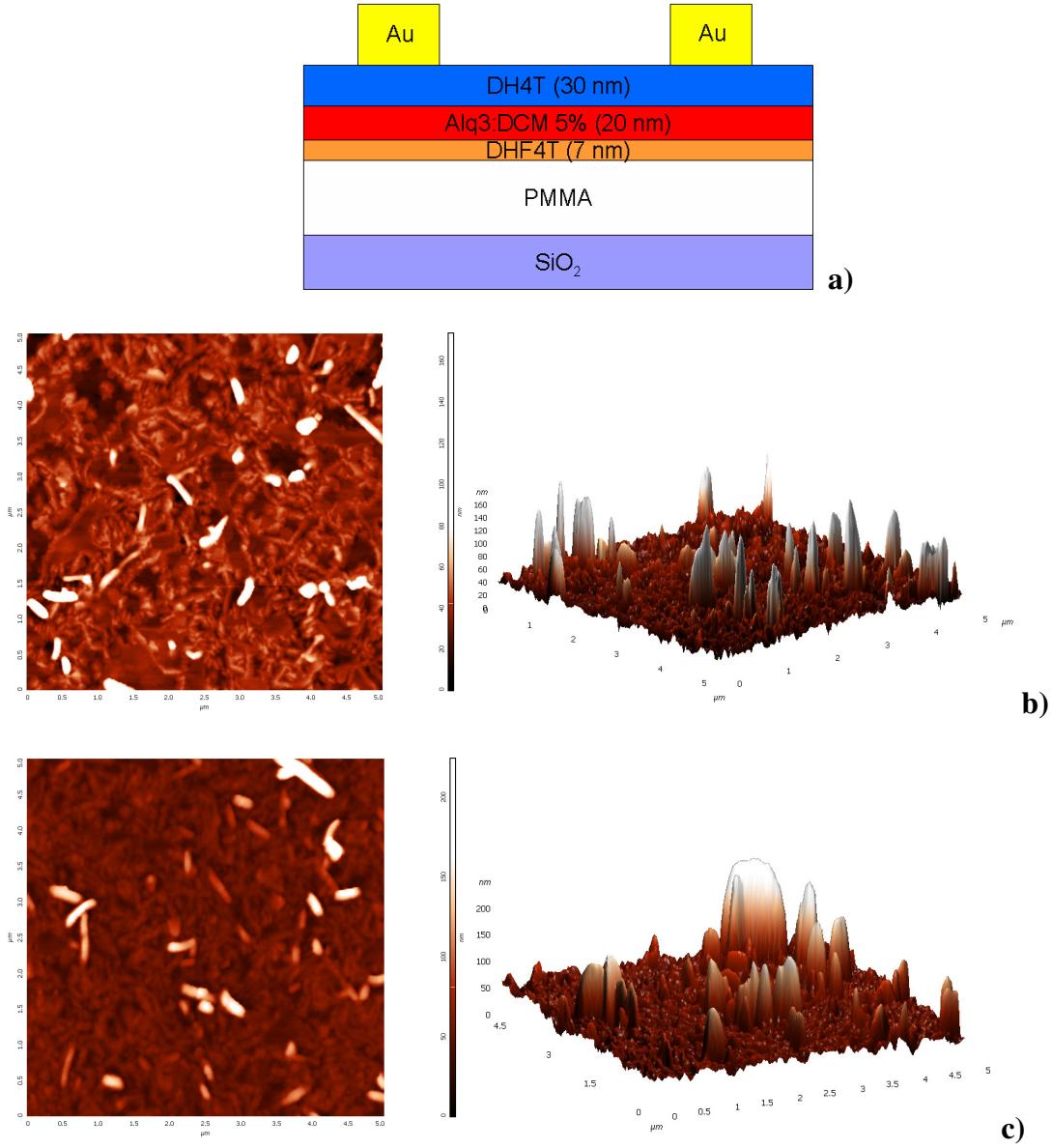

Figure 2.4.7. (a) Schematic of the complete device structure with DH4T on top. 5x5µm AFM images of the DH4T layer. (b) Device made on SiO_2 with 3D image, (c) Device made on ITO with 3D image.

It can be concluded from this work that the first layer, DHF4T, plays a significant role in the morphologies of the Alq3:DCM 5% and DH4T layers. Therefore it is important to obtain the best morphology of the first layer in order to control the morphologies of the subsequent layers.

To prove the suitability of the photonic feedback structures prepared by interference lithography to achieve lasing with the organic light emitting materials used in the project, a batch of samples was prepared by partners CNR (T3:DCM) and IMEC (Alq_3:DCM2). The SiO_2 DFB structures patterned on silicon substrates, used for this investigation, were designed for a target resonance wavelength of

625 nm which should be suitable for both emitting materials. These structures are based on a second order linear Bragg grating with a period of 400 nm for the sample containing T3:DCM and a first order linear Bragg grating with a period of 200 nm in case of Alq_3:DCM2. Both gratings show up a duty cycle of 50%.

Neat films of the organic layer were deposited on plain quartz or glass substrates and serve as reference samples. Table 2. 4.2 summarizes the investigated samples.

Sample name	Emitting material	DFB pitch	DFB type	Sample cross section
T3-A	300 nm T3:DCM (10%)	-	-	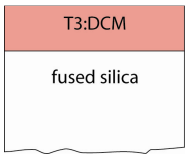
T3-B	300 nm T3:DCM (10%)	400 nm	2nd order	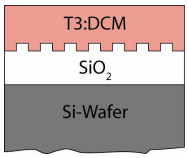
Alq3-A	200 nm Alq_3:DCM2 (2%)	-	-	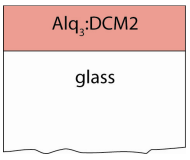
Alq3-B	200 nm Alq_3:DCM2 (2%)	200 nm	1st order	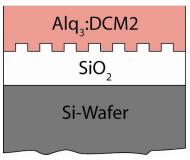

Table 2.4.2. Investigated samples in ASE/laser emission experiments.

Figure 2.4.8 (a) depicts the edge-emitted spectral intensity at the peak emission wavelength of a 300 nm thick T3:DCM film grown on fused silica for different pump powers (sample T3-A). A set of corresponding emission spectra is shown in the inset. At laser fluences below the ASE threshold a broad emission spectrum spanning from 550 to 725 nm is observed. This is attributed to spontaneous emission of the DCM molecules, which are populated in an excited state via optical pumping of the host system T3 and subsequent energy transfer to the guest DCM molecules. Increasing the excitation fluence to higher values results in a spectral narrowing around the maximum emission wavelength of 620 nm – characteristic for ASE.

Furthermore we observe a change in slope of the peak emission curve at ASE threshold, which separates two regimes of diverse differential emission efficiency. The threshold is numerically

extracted from the intersection of two linear regression curves (red lines) for data below and above threshold. For sample T3-A, we calculate an ASE threshold of ~15µJ/cm².

a) b)

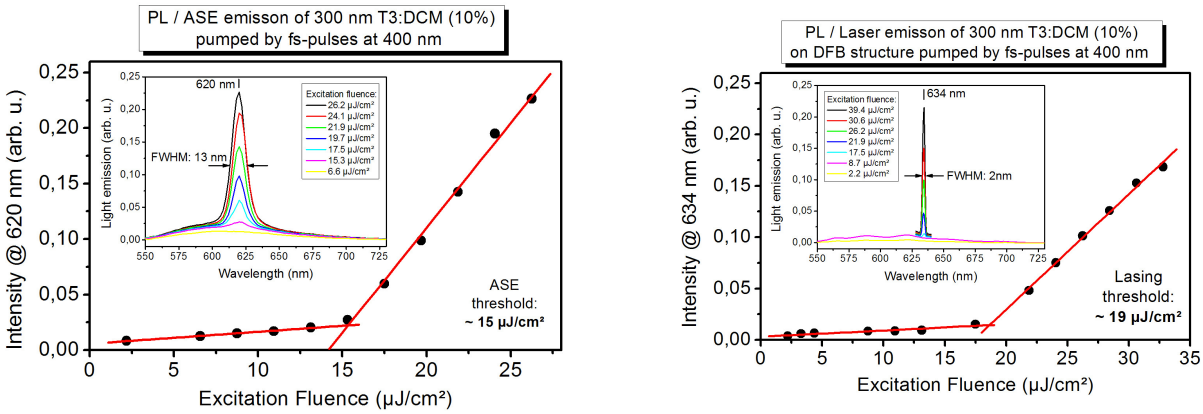

Figure 2.4.8 ASE/lasing threshold measurement of (a) sample T3-A and (b) sample T3-B.

Figure 2.4.8 (b) depicts the results of the same experiment performed on the T3:DCM film grown on a distributed feedback structure (sample T3-B). Again, a spectral narrowing is observed above a certain threshold level accompanied by a change in the slope of emission efficiency. A closer look at the emission spectra (see inset of Figure 2.4.8 (b)) shows, that the peak emission wavelength above the threshold (634 nm) does not coincide with the peak emission wavelength of the ASE characteristics observed in sample T3-A (620 nm). Furthermore the width of the emission peak above threshold in sample T3-B of 2 nm is much smaller as compared to the ASE peak width of 13 nm in sample T3-A.

Both observations can be attributed to the presence of the distributed feedback structure in sample T3-B, forming a resonator for a certain wavelength and forcing the emission to shift away from the material's gain maximum. The coupling strength of the grating, together with scattering losses, determines the resonance width (FWHM of the emission peak), from which a quality factor of ~314 can be calculated for the feedback structure. The lasing threshold in sample T3-B of 19 µJ/cm^2 increases slightly as compared to the value of 15 µJ/cm² in the neat film sample T3-A.

In Figure 2.4.9 the emission characteristics of a 300 nm thick Alq_3:DCM2 film on (a) quartz substrate (sample Alq3-A) and (b) distributed feedback structure (sample Alg3-B) are shown. The Alq3:DCM2 film exhibits characteristic narrowing of the emission spectrum around 650 nm, the gain maximum of this material (see Figure 2.4.9 (a)). From the peak emission we extract an ASE threshold of 6 µJ/cm².

a) b)

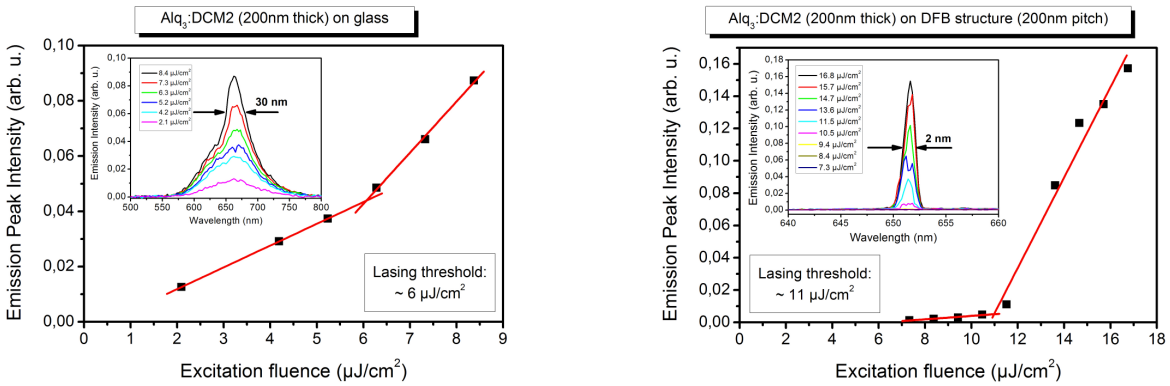

Figure 2.4.9. ASE/lasing threshold measurement of (a) sample Alq3-A and (b) sample Alq3-B.

Figure 2.4.9 (b) shows the emission spectra and peak intensities of the Alq3:DCM2 film grown on the DFB structure. Again a characteristic emission narrowing due to the DFB resonator can be observed, accompanied by a change in slope of the peak emission intensity. For the extracted lasing threshold of 11 μJ/cm^2 we find a moderate increase as compared to the bare organic film on glass substrate (reference sample Alq3-B).

From these data we concluded that a suitable set of organic lasing materials and DFB structures were found within the consortium.

The next step was the investigation of samples, which comprise organic heterojunctions integrated into distributed feedback structures. Additional layers for electron and hole transport in the organic heterojunction are assumed to increase optical propagation losses and decrease the confinement factor of the optical mode. Both effects are expected to result in an increased lasing threshold and necessitate a detailed investigation to ensure the lasing functionality of the organic laser device.

For Alq_3:DCM2, the above described ASE and lasing threshold measurements confirmed a low threshold, which qualifies it directly for testing within more complex structures. For this purpose a sample was prepared by partner IMEC, which contains an organic heterojunction. A layer of 50 nm PTAA serves as hole transporting material and is deposited between sample substrate and the organic lasing layer. In addition a smoother growth of Alq_3:DCM2 is expected on the PTAA surface as compared to the uneven surface of the DFB structure. The thickness of Alq3:DCM was reduced to 150 nm to keep the total thickness of the organic layers constant at 200 nm and still fit the effective refractive index, for which the DFB structures were designed. Like in earlier measurements, a reference sample was prepared in the same fabrication run, grown on a plain glass substrate instead of the DFB structure. Table 2.4.3 lists these samples:

Sample name	Emitting material	DFB type/pitch	Hole transporting material	Sample cross section
Alq3-C	150 nm Alq_3:DCM2 (2%)	1st order / 200 nm	50 nm PTAA	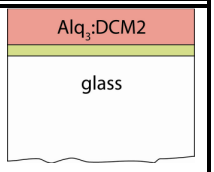
Alq3-D	150 nm Alq_3:DCM2 (2%)	1st order / 200 nm	50 nm PTAA	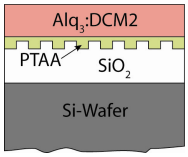

Table 2.4.3. Investigated heterojunction samples in ASE/laser emission experiments.

In Figure 2.4.10 the results of the ASE/lasing emission characterization of the samples containing a heterojunction are shown. In the inset of Fig. 2.4.10 (a) the edge emitted light from the reference sample Alq3-C is depicted. With respect to the single Alq_3:DCM2 films on SiO_2 (shown in Figure 2.4.10) the maximum emission of Alq_3:DCM2 is significantly blue-shifted, that is roughly in the 620 to 580 nm range. This observation is still under discussion within the OLAS consortium and cannot be explained here. As the value for ASE threshold cannot be clearly extracted from the peak emission intensities like in measurements before, we plot here the full width at half maximum versus the excitation fluence. The characteristic narrowing at ASE threshold is obvious and we extract a threshold value of 10 µJ/cm^2.

As mentioned above, we expect an increase in ASE threshold due to the incorporation of the additional PTAA organic layer and its moderate increase from 6 µJ/cm^2 to 10 µJ/cm^2 is reasonable.

a) b)

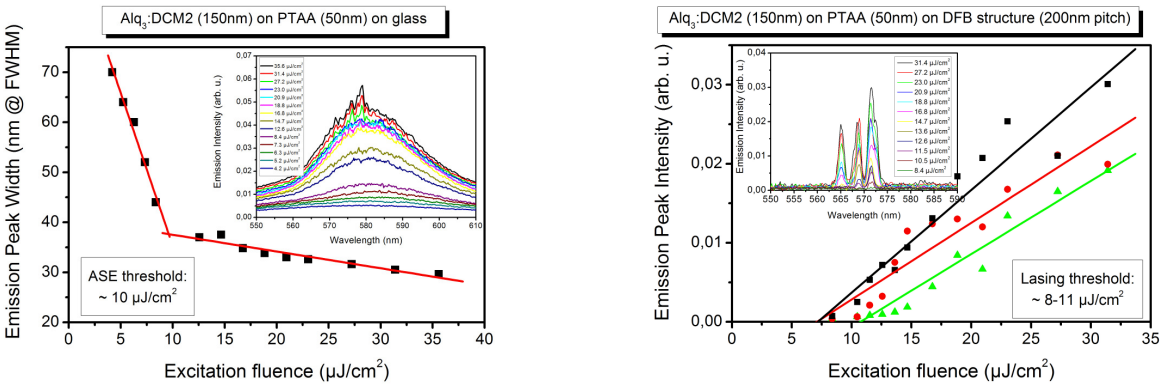

Figure 2.4.10 ASE/lasing threshold measurement of (a) sample Alq3-C and (b) sample Alq3-D.

Figure 2.4.10 (b) depicts the results for the same film stack on DFB structure (sample Alq3-D). Unlike in other measurements the emitted light spectrum does not show a single emission peak but three instead. Each emission peak exhibits a linewidth of 2 nm, which is comparable to result on previous samples containing DFB structures. As the wavelength of the observed emission from Alq3:DCM2 on a PTAA is different from Alq3:DCM2 films on SiO_2. Since this does not coincide with the value for which the DFB structures are designed, this unexpected behaviour shall be analyzed by further modelling of the feedback structure in this wavelength range.

Although we do not see the emission from the expected lasing mode in sample Alq3-D, we conclude from the investigations, that the incorporation of both, heterojunction and DFB structures, does not seriously increase lasing threshold. Moreover lower scattering losses due to the smoother growth of Alq_3:DCM2 on the PTAA layer seems to compensate for lower confinement factor in these structures.

A next important step is to evaluate the effect on the lasing properties of the inclusion in the heetrojunction of an additional organic layer on top of the light emitting one.

First, pump-probe measurements on a 170nm thick layer of Alq3 doped with 2%wt DCM2 deposited on a fused silica substrate has been performed to verify the wavelength with maximum gain of Alq3:DCM2. Figure 2.4.11 shows the time-resolved transient absorption spectrum. The gain region of the DCM2 dye at about 640-650nm appears red-shifted compared to the photoluminescence spectrum which has its peak between 610-620nm. In a complementary measurement, we observed ASE in the same wavelength range, see Figure 2.4.12. Both measurements indicate that the optical feedback mechanism should be designed to have the resonator wavelength around 640 nm.

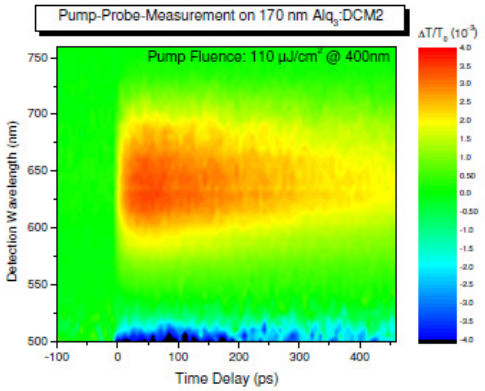

Figure 2.4.11. Transient absorption measurement on Alq3:DCM2 shows a gain maximum near 645nm.

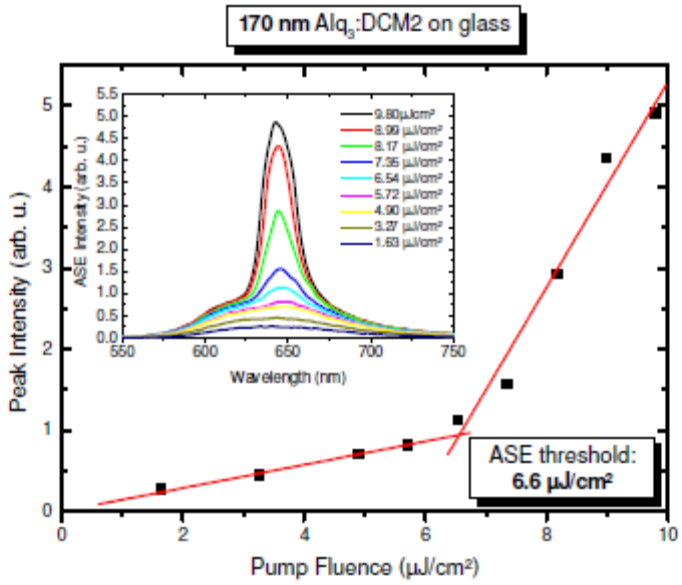

Figure 2.4.12. Measurement of the edge emission as a function of the pump power. Above the ASE threshold narrowing of the spectrum is observed (inset).

While second-order photonic feedback structures are easier to characterize because of the vertical emission direction, first-order structures have a potentially lower lasing threshold because of the lack of vertical losses. Hence, the choice for the final device is a first-order linear grating structure which should exhibit the lowest threshold. From photonic simulations we obtain the optimum photonic grating structure for the given technological and optical constraints. According to these simulations trenches of 50nm depth are etched into SiO2 with a pitch of 210nm and a duty cycle of 50%. Figure 2.4.13 shows a scanning electron microscope image of the cleaved cross section of the fabricated structure after organic layer deposition.

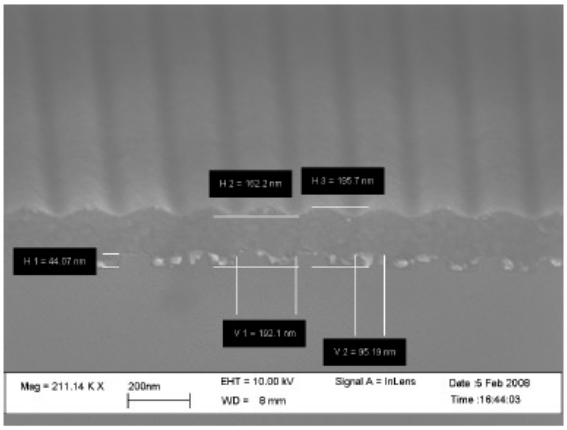

Figure 2.4.13. SEM cross section of the photonic structure covered with PTAA and Alq3:DCM2. Due to low chemical contrast derived from the scattered electron signal it is not possible to conclude if the PTAA fills the trenches of the grating completely.

Because the waviness of the grating is retained on the surface, an effective average thickness must be taken into account in the photonic simulations. Deposition of 200nm organic material on top of the grating yields an effective thickness of 225nm which should result in the lowest possible threshold and a lasing wavelength between 640-645nm. Since the small thickness of the gain layer in the electrically pumped device is a key issue we fabricated a series of samples with Alq3 on first order photonic gratings. We investigated the lasing behavior with decreasing thickness of the DCM2 doped part. These gain regions are always vertically centered in the layer stack in order to achieve good spatial overlap with the intensity maximum of the laser mode, see inset of Figure 2.4.14.

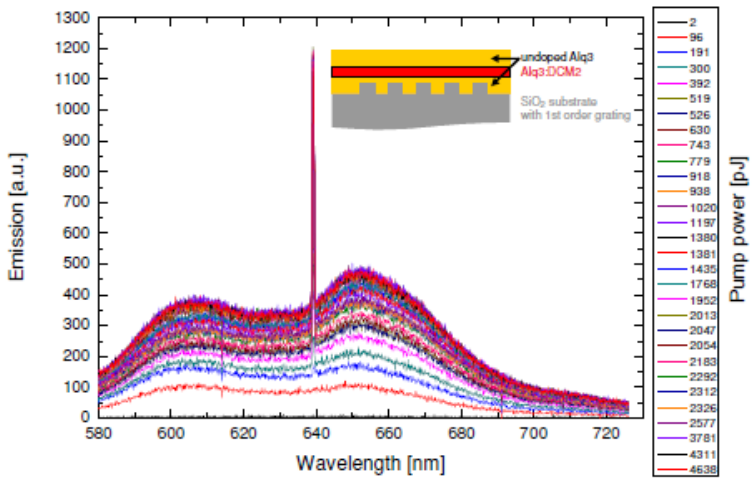

Figure 2.4.14 A lasing peak emerges from the photoluminescence spectrum above the pump power threshold. The inset shows the schematic illustration of the first order distributed feedback lasing structure.

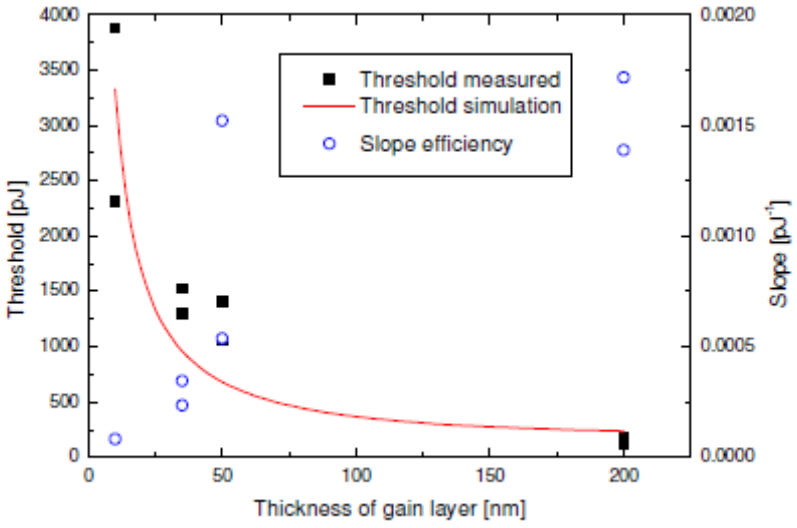

Figure 2.4.15. Measured lasing threshold as a function of thickness of the DCM2-doped part. The solid line is the theoretical expectation from the calculated confinement factor. The open circles are the slope efficiency of the laser.

Figure 2.4.14 shows the emission from 200nm Alq3:DCM2 on the photonic grating. The lasing threshold and the slope efficiency are extracted from this luminescence data. Because the grating is in first order and the lasing mode is guided in-plane, the sample has to be tilted with respect to the light collection lens by approximately 30 degrees in order to be able to detect sufficient scattered intensity. We checked that the tilting angle does not have a significant influence on the extracted values but improves the signal-to-noise ratio dramatically. In Figure 2.4.15 we plot both figures-of-merit as a function of thickness of the DCM2-doped part. Lasing can be observed down to gain layer thicknesses of 10nm. This is particularly encouraging since this thickness corresponds to the Langevin radius in the electrically pumped device. However, the threshold is – as expected from the calculated modal overlap – about one order of magnitude higher than for the device where the whole deposited organic layer shows gain. Accordingly, the slope efficiency of the laser decreases with decreasing gain layer thickness.

Next, the hole transporting layer has been included in the structure by spin-coating 50nm of PTAA on top of the first order grating. Since the refractive indices of PTAA and Alq3 match closely, the grating geometry can be retained. On top of the PTAA, varying thicknesses of DCM2-doped Alq3 are deposited, and the layer stack is completed to a total thickness of 200nm by undoped Alq3 as electron transporting layer.

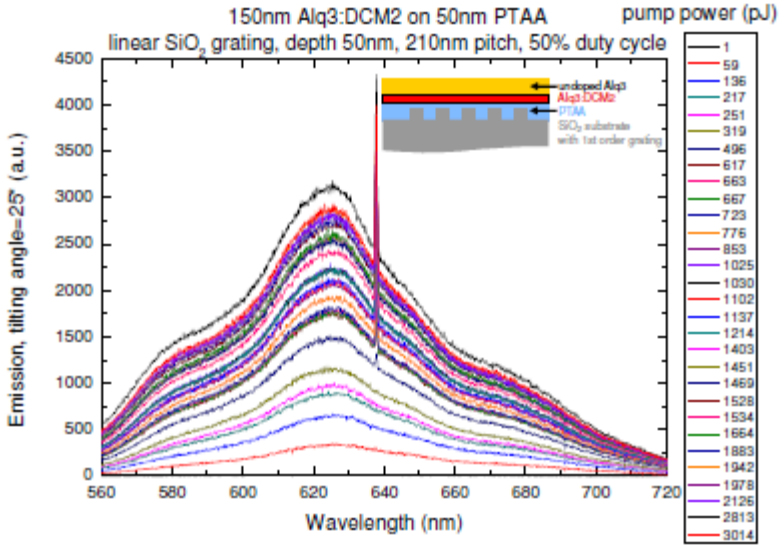

Figure 2.4.16. Emission from lasing structure with hole transport layer, gain layer and electron transport layer. Above the threshold a lasing peak appears in the spectrum.

Figure 2.4.16 shows the luminescence spectra of a sample comprising 50 nm PTAA and 150 nm Alq3:DCM2, measured at various pumping intensities. We observe that the threshold pump power for thick gain layers is only slightly higher compared to the value without PTAA which is an indication of good growth of Alq3 on the spin-coated PTAA. However as shown in Figure 2.4.17, for a thickness of the DCM2-doped layer of 20nm or below, we could not observe lasing. This

indicates that the optical loss due to the layer structure (interfaces, roughness, etc.) is a substantial challenge for lasing even without quenching mechanisms under electrical bias or more absorbing materials such as PTCDI.

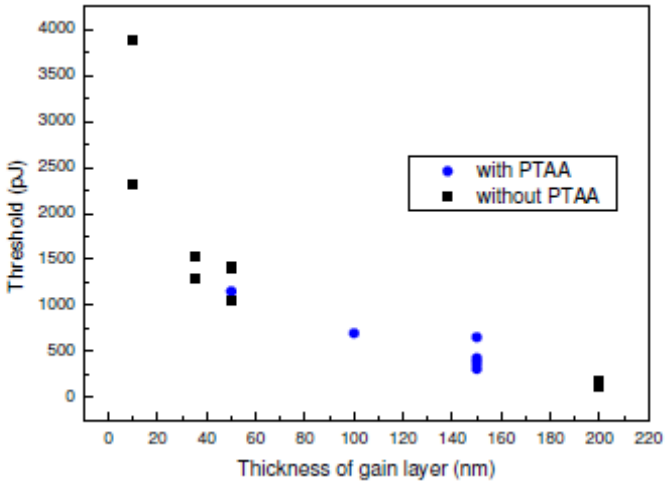

Figure 2.4.17 The laser threshold increases for thinner DCM2-doped layers on PTAA. On the samples with 20nm gain layer thickness or below we could not observe lasing with the available pump energy of several ten thousand picojoules per pulse. Additionally, the threshold for devices without PTAA have been shown for comparision**.**

An important conclusion from these measurements is that we are able to observe optically pumped lasing from a device with the complete material stack. Lasing could be achieved for gain layers of only 10 nm thickness. Such thin layers are equal to the spatial region where the excitons are produced in the electrically pumped device. However, the threshold increases dramatically for these thinner gain layers. For the stack with PTAA and gain layers of 20nm thickness or below lasing could not be achieved. But, since the presence of PTAA does not change the laser threshold pump power significantly compared to Alq3 for thick gain layers, the absence of lasing could be due to some difficulties during preparation of the very thin Alq3:DCM2 layers. Additional measurements of optically pumped lasing in organic heterojunctions in photonic feedback structures are discussed in WP7.

Table 2.4.4: Deliverables of WP4

Del. no.	Deliverable name	Workpackage no.	Date due (month)	Actual delivery date	Estimated indicative person-months (total)	Used indicative person-months (to date)	Lead contractor

D10	Technical analysis of waveguide and mirror losses of photonic feedback structures	4	M12	M12	4	3	RWTH
D15	Morphology and spectroscopy of organic heterojunctions on feedback structures	4	M15	M15	6	6	RWTH
D17	Technical analysis of optically pumped laser of organic heterojunctions on photonic feedback structures	4	M18	M18	4	4	RWTH

Table 2.4.5: Milestones of WP4

Milestone no.	Milestone name	Workpackage no.	Date due	Actual delivery date	Lead contractor
M6	Achieve optically pumped laser of organic heterojunctions on photonic feedback structures	4	M18	M18	RWTH

WP5. Technology for organic heterojunctions (WP Leader: IMEC)

The objective of this workpackage is to develop a full technology set for realizing organic heterojunctions, field-effect light-emitting devices, and for integrating the organic heterojunctions in these field-effect devices.

Different device architectures were considered and pursued in parallel within OLAS, in order to increase the chances of achieving all device specifications. In particular, most of the effort was devoted to the development of the fabrication technology of two device structures: a hybrid vertical/planar device (Device 1) and a three layer vertical heterojunction in a plana+
r field-effect device (Device 2). The two device geometries are depicted in Figure 2.5.1(a) and 2.5.1(b). In both configurations, two different organic layers are employed to transport the holes and electrons, while the light emission occurs several microns away from the metallic contacts. The working principles of these devices are described in detail in WP1.

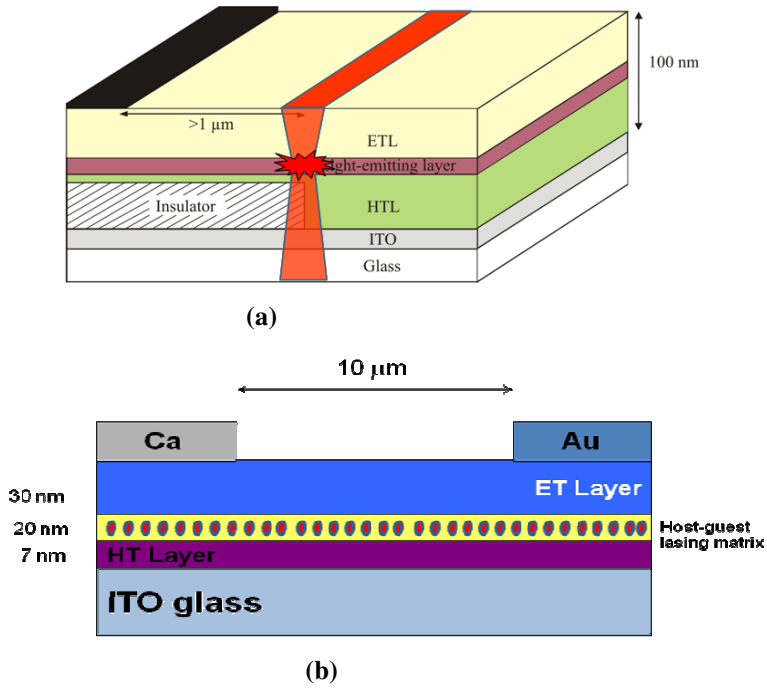

Figure 2.5.1: Scheme of the different device architectures considered within OLAS. (a) Field-effect light-emitting device based on a hybrid vertical/planar organic heterojunction, and (b) Planar field-effect device comprising a three layer vertical organic heterojunction.

Organic light-emitting device based on a vertical/planar heterojunction (Device 1)

The schematic architecture of Device 1 is illustrated in Figure 2.5.1(a). The device is fabricated on top of an ITO-coated glass substrate and comprises an organic hole-transport layer (HTL), an organic light-emitting layer and an organic electron-transport layer (ETL). Prior to the deposition of these organic layers, an insulating layer of SiO_2 is deposited on top of the ITO. Trenches are selectively wet-etched through the SiO_2, to be able to contact the ITO layer which serves as the hole-injecting electrode in the device. The cathode is formed by a thin layer of 0.6 nm lithium fluoride (LiF) followed by the deposition of 100 nm aluminum (Al). This cathode is not positioned vertically above the ITO anode in the trench in the SiO_2 insulator, but it is located fully above the insulator, as shown in Figure 2.5.1(a). The distance between the metallic top-electrode and the insulator edge is one to several microns. Accurate alignment of the metallic cathode is obtained by using an integrated shadow mask technique and angled deposition of the LiF/Al layer (Figure 2.5.2). This technique was developed and optimized by IMEC.

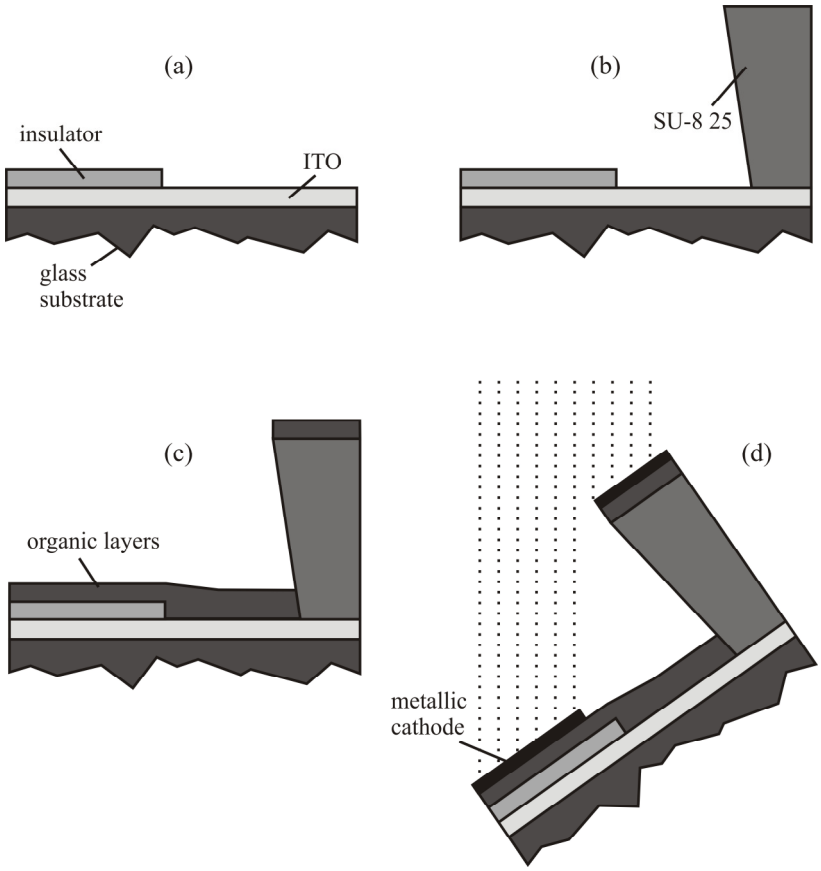

Figure 2.5.2. Schematic processing sequence for Device 1: (a) before creation of the integrated shadow mask, (b) the integrated shadow mask is deposited, (c) after organic layer deposition and (d) deposition of the metallic cathode while the substrate is mounted on a triangular sample holder. During this deposition, the molecular flux is at a 45° angle with respect to the substrate.

The integrated shadow mask is realized by patterning a 20 µm thick negative photoresist SU-8 25 (purchased from MicroChem Corp.). Processing of the SU-8 25 leads to a patterned layer of about 20 µm thickness that is resistant to solvents, acids and bases and has excellent thermal stability. Even higher thicknesses (up to, and even beyond 200µm) are achievable using different formulations of the SU-8 25 photoresist. The highest temperature used in the processing of SU-8 25 is only 95°C, which makes this method thermally compatible with production technologies on flexible substrates. A schematic cross-section of the sample in this stage of the processing is shown in Figure 2.5.2(b).

The different organic layers, being the hole transporting material, the light-emitting layer and the electron transporting material are deposited after application and patterning of the SU-8 25 resist. This is depicted in Figure 2.5.2(c). Subsequently, the sample is mounted on a triangular sample holder and loaded in the ultra-high vacuum system for cathode evaporation. During this deposition, the flux is at a 45° angle with respect to the substrate. The SU-8 25 profile thus creates a shadowed

region with a span similar to the thickness of the SU-8 25, such that the substrate is only partially covered with the metal. Figure 2.5.2(d) schematically illustrates this deposition step. Obviously, the width of the area that is not covered with metal can be changed by using a thicker layer of SU-8 25. The same effect can be achieved by choosing a different angle for deposition.

For our purpose, the distance between the metal top-electrode and the insulator edge is of main interest. This distance is determined by the thickness of the SU-8 25 layer, the deposition angle and the spacing between the insulator and the SU-8 25. By optimizing all these parameters we are able to position the metallic cathode at one to several microns from the insulator edge, as can be verified from the optical microscope images in Figure 2.5.3. The shadowed region where no metal is deposited can be clearly recognized. In Figure 2.5.3(a) the metallic layer (white area) is deposited at a distance of 5 µm from the insulator edge (indicated by the white arrow). In Figure 2.5.3(b) on the other hand has a distance of 17 µm. The difference between both devices is, in this case, achieved by adjusting the spacing between the insulator and the SU-8 25 layer.

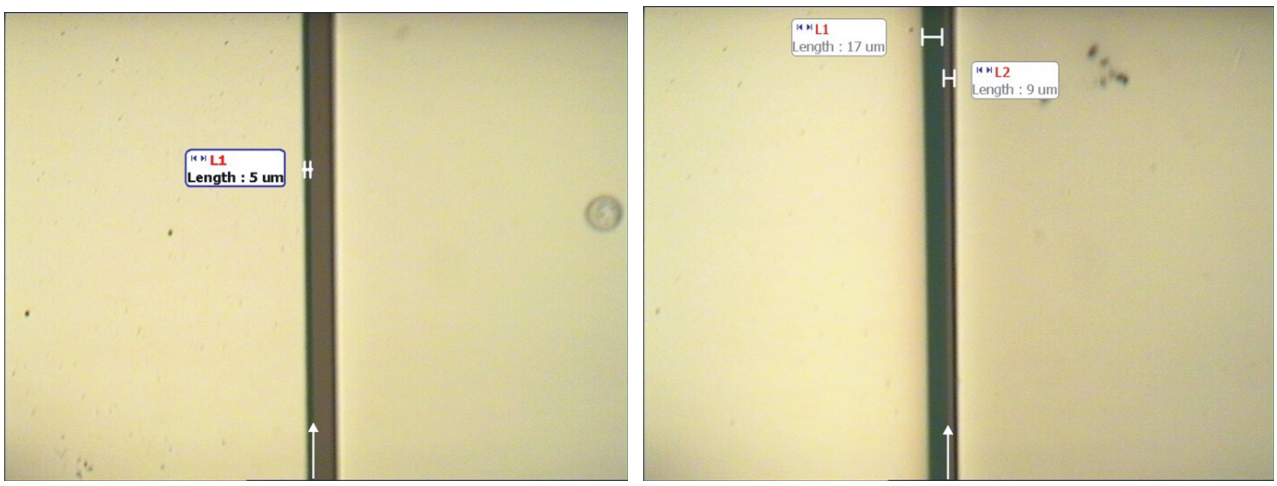

(a) **(b)**

Figure 2.5.3. Optical microscope images of devices fabricated using a thick SU-8 25 layer as integrated shadow mask. The distance between the metallic layer (white area) and the insulator edge, indicated by the white arrow, is 5 µm and 17 µm respectively for (a) and (b).

Figure 2.5.4 shows a scanning electron microscopy (SEM) image of the device structure. The shadowed region where no metal is deposited can be recognized. It can also be verified that the walls of the SU-8 25 layer are slightly re-entrant, which is typical for negative photoresists.

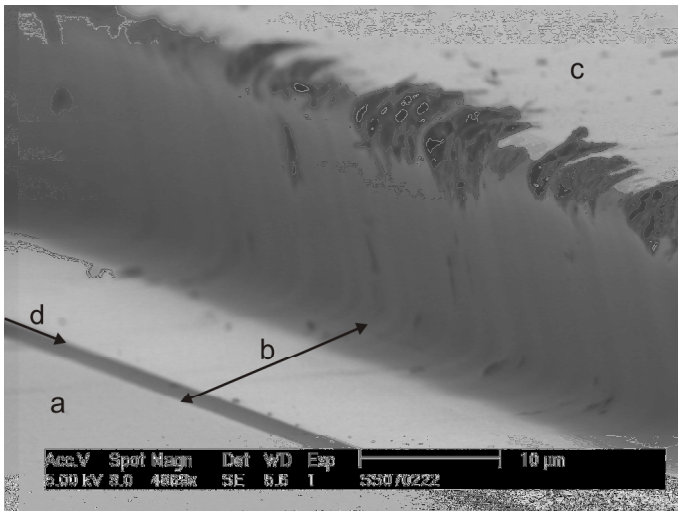

Figure 2.5.4. SEM image of the device structure. a) metallic cathode, b) shadowed region where no metal is deposited, c) the 20 µm thick SU-8 25 layer and d) arrow indicating the insulator edge.

To fabricate Device 1, different organic materials are used. Poly(triarylamine) (PTAA) was selected as the hole-transport material. When PTAA is deposited by spincoating results in a film with a smooth top surface that is favorable for the growth of an additional layer. In addition, PTAA has the advantage of forming high-quality interfaces, which are free of electron traps, and allows achieving good electron transport in an additional organic layer deposited on top of it.

The use of a host-guest system for light-emission was envisaged as the best way for having efficient light-emission and a low lasing threshold. Therefore, the active light-emitting layer consists of a host-matrix incorporating a dopant at a relatively low concentration. Two different host-guest systems are chosen for this device fabrication. The first host-guest system is made of 2,9-dimethyl-4,7-diphenyl-1,10-phenanthroline (BCP) doped with 10% Iridium (III) bis(2-(2'-benzo-thienyl)pyridinatoN,C³')(acetyl-acetonate) ($Btp_2Ir(acac)$). $Btp_2Ir(acac)$ is a well-known red light-emitting phosphorescent dye used in OLEDs and was one of the emitting materials that we considered in the beginning of the project. However, during the course of the project we decided to exclude triplet emitters from further investigation as no amplified spontaneous emission (ASE) could be observed using these materials (see WP6). A second host-guest system is therefore proposed, formed by tris(8-hydroxyquinoline) aluminum (Alq_3) doped with 2% of 4-(Dicyanomethylene)-2-methyl-6-(julolindin-4-yl-vinyl)-4H-pyran (DCM2). Alq_3:DCM2 is a benchmark host-guest system for which low ASE thresholds are achieved.

The electron-transport material is selected according to two criteria. First, the organic electron-transport material should have a high electron field-effect mobility since this mobility determines the performance. Second, as electron transport is intended to occur at the heterojunction between the electron-transport layer and the light-emitting layer, the lowest unoccupied molecular orbital (LUMO) of the electron-transport material should be slightly lower than the LUMO of the host and the guest of the light-emitting layer. N,N'-ditridecylperylene-3,4,9,10-tetracarboxylic diimide (PTCDI-$C_{13}H_{27}$) satisfies these two conditions and is therefore used as the electron-transport material.

Another possibility is to use DHF-4T. This organic material offers a good alternative for PTCDI-$C_{13}H_{27}$ as it allows for high electron mobilities and the LUMO of DHF-4T (3.3 eV) is positioned slightly lower than the LUMO of the host and the guest of the light-emitting layer. Moreover, it has the advantage that the bandgap is larger that the one of PTCDI-$C_{13}H_{27}$, which reduces re-absorption of the red emitted light. The molecular structures of the above mentioned materials are schematically shown in Figure 2.5.5. The position of their energy levels are given in Figure 2.5.6.

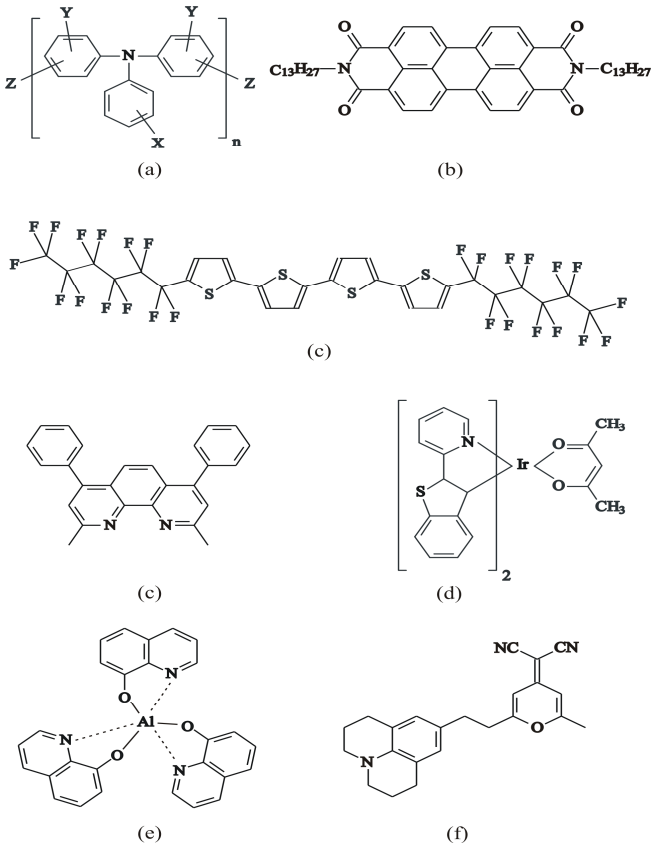

Figure 2.5.5. The molecular structure of (a) PTAA, (b) PTCDI-$C_{13}H_{27}$, (c) DHF-4T, (d) BCP, (e) $Btp_2Ir(acac)$, (f) Alq_3 and (g) DCM2.

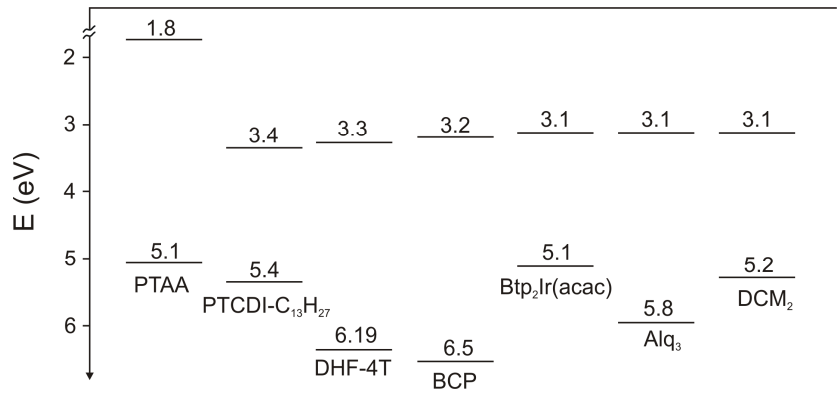

Figure 2.5.6. The energy levels of the highest occupied molecular orbital (HOMO) and the lowest unoccupied molecular orbital (LUMO) of the materials shown in Figure 2.5.5.

PTAA was typically deposited by spin-coating at 1000 rpm for 60 seconds. Subsequently, the sample was heated on a hotplate at 110°C for 20 minutes to make sure all the solvent had evaporated. Afterwards, a 20 nm thick light-emitting layer is deposited in ultra-high vacuum (P = 10^{-8} torr) by co-evaporation of 100:2 (mass ratio) Alq_3 and DCM2 or by co-evaporation of 100:10 BCP and $Btp_2Ir(acac)$. Then, a 50 nm thick electron transport layer was evaporated on top of the light-emitting layer. This layer can be either PTCDI-$C_{13}H_{27}$ or DHF-4T. The deposition rate during evaporation is respectively 0.5 Å/s and 3 Å/s, while the substrate remains at room temperature. All processing steps are carried out in a dry nitrogen glovebox (< 1 ppm O_2, < 5 ppm H_2O) or in ultra-high vacuum.

Devices were typically measured immediately after evaporation in an inert N_2 atmosphere using an Agilent 4156C parameter analyzer. A calibrated integrated sphere (SphereOptics Hoffman GmbH) was used for light intensity measurements and external quantum efficiency calculations. To determine the spectral characteristics, the emitted light is detected by means of an optical multichannel analyzer (OMA) in conjunction with a charge coupled device (CCD). These measurements are performed at room temperature in a cryostat to prevent photo-oxidation. Figure 2.5.7 displays the experimentally measured characteristics of a light-emitting device based on a vertical heterojunction. The device comprises the organic stack PTAA/Alq_3:DCM2/PTCDI-$C_{13}H_{27}$ and has a width of 1 mm. The metallic cathode is displaced by 3.5 µm with respect to the insulator edge. Under forward bias, the current increases with increasing voltage. The electrical characteristics can be explained by the equivalent circuit shown as inset in Figure 2.5.7(b). This equivalent circuit consists of an n-type transistor having a diode between the gate and the drain. The external quantum efficiency of the device is estimated based on luminance, electroluminescence

spectra and current (Figure 2.5.7(c)). The external quantum efficiency is as high as in conventional OLEDs comprising the same materials and is remarkably independent of the current, up to current densities of more than 10 A/cm².

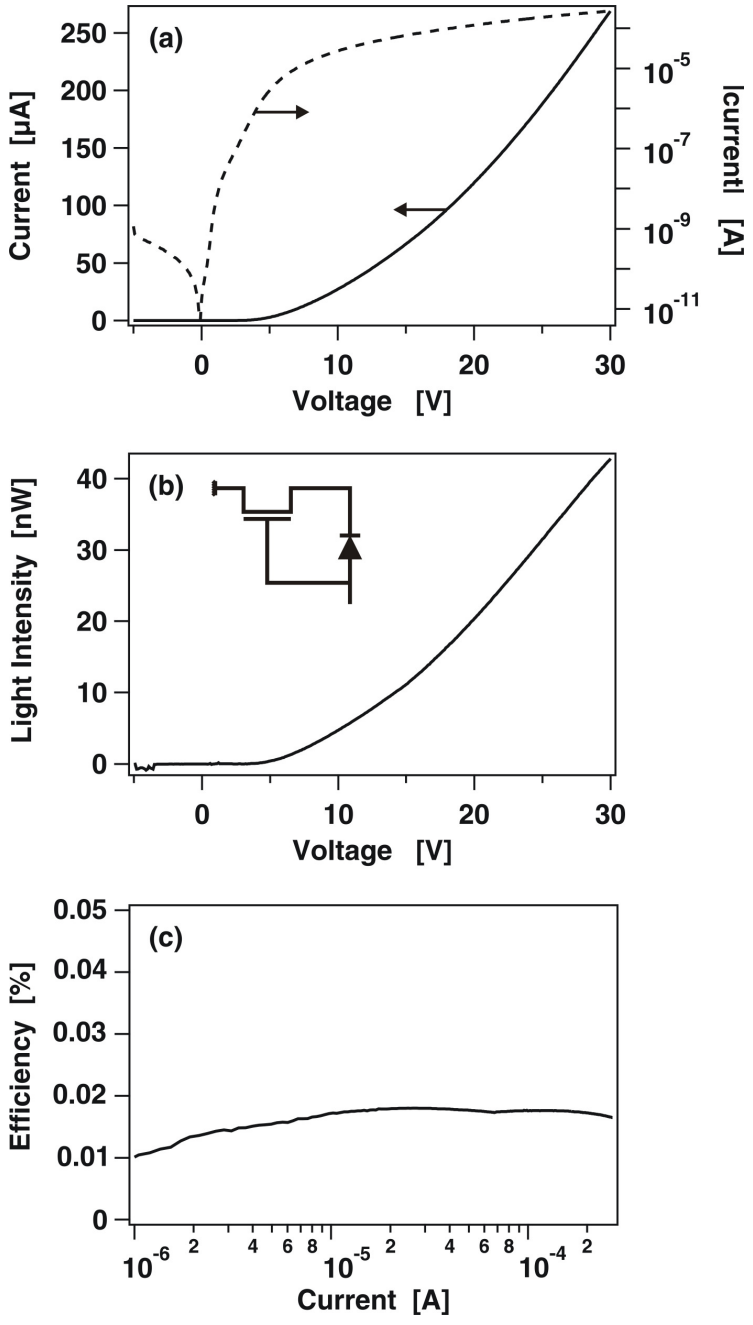

Figure 2.5.7. Experimentally measured characteristics of an organic light-emitting device based on a vertical heterojunction. This device has a width of 1 mm and a distance between top electrode and insulator edge of 3.5 µm. (a) Current-voltage characteristics, (b) corresponding light output. Inset: equivalent circuit of the device, and (c) external quantum efficiency as a function of the current.

Planar field-effect device comprising a three layer vertical organic heterojunction (Device 2)

In order to fabricate field-effect transistors based on three layer vertical organic heterojunctions according to the scheme reported below and described in WP1, a new dynamic masking system was designed and realized.

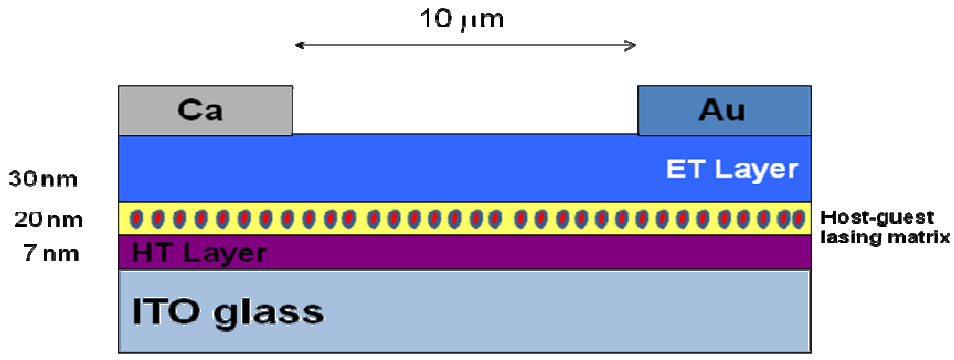

Figure 2.5.8. Scheme of an idealized light-emitting field-effect transistor structure based on three layer vertical organic heterojunctions.

The key features desired when fabricating injection contacts for the device structure in figure 2.5.8 are: i) both metallic contacts should be evaporated on top of the organic heterojunction, ii) the separation between contacts should be as low as 10 µm, iii) the two contacts should be made of different metals (typically calcium and gold).
These features cannot be achieved using standard shadow masks. Therefore a dynamic masking system was realized by CNR, whose main characteristics are described in the scheme of figure 2.5.9.

The fabrication of bi-metal contacts with 10 µm separation on top of an organic heterojunction is accomplished by implementing the following procedure:
STEP I: The organic heterojunction (green) is first evaporated through the three large segments of the shadow mask.
STEP II: The mask is then moved laterally so that the three small area segments in the shadow mask are superimposed to the organic heterojunction deposited in STEP I. The first metal is evaporated thereby fabricating the first contact.
STEP III: The mask is moved laterally along the same direction defined in STEP II over a distance that will determine the transistor channel length. The minimum movement step is of about 1 micron and the positioning error is below 10%.
STEP IV: The second metal is evaporated thereby fabricating the second contact at a distance of few microns from the first one.

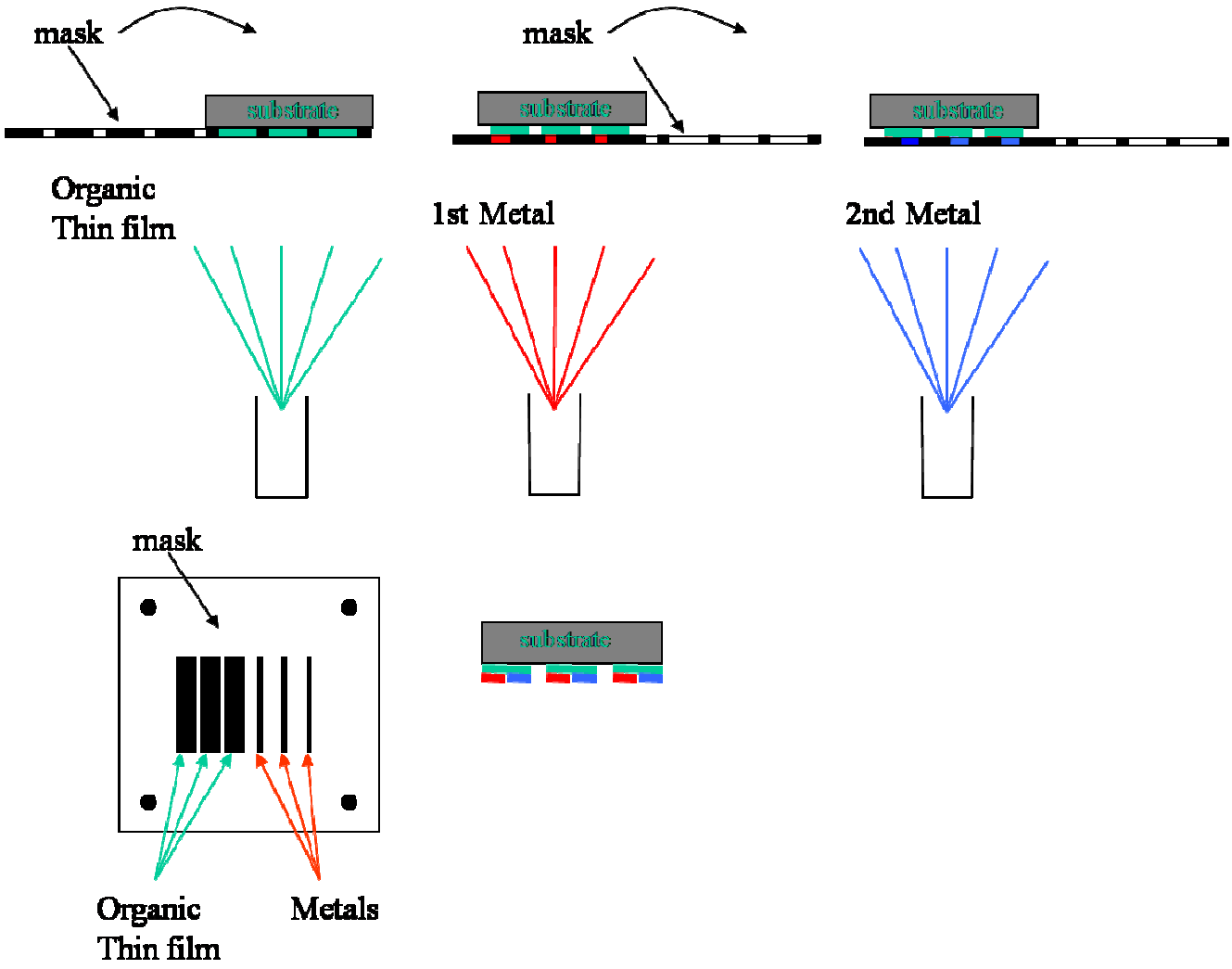

Figure 2.5.9. Schematics of the dynamic system procedure used for bi-metal contact fabrication on top of organic heterojunction with channel length of 10 microns.

Using the mask depicted in figure 2.5.9 and the above described procedure three devices aligned parallel to one another on the same substrate can be contemporary fabricated.

As a feasibility demonstration, figures 2.5.9 and 2.5.11 report pictures of gold top contacts fabricated using the dynamic masking system described in figure 2.5.9. The channel length is shorter than 20 μm.

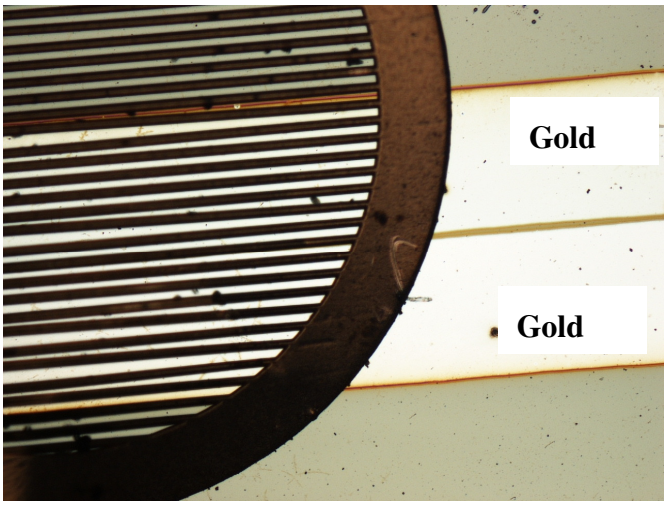

Figure 2.5.10. Photograph of gold top contacts fabricated using the newly developed dynamic masking system. The reference grid has a pitch of 20 μm.

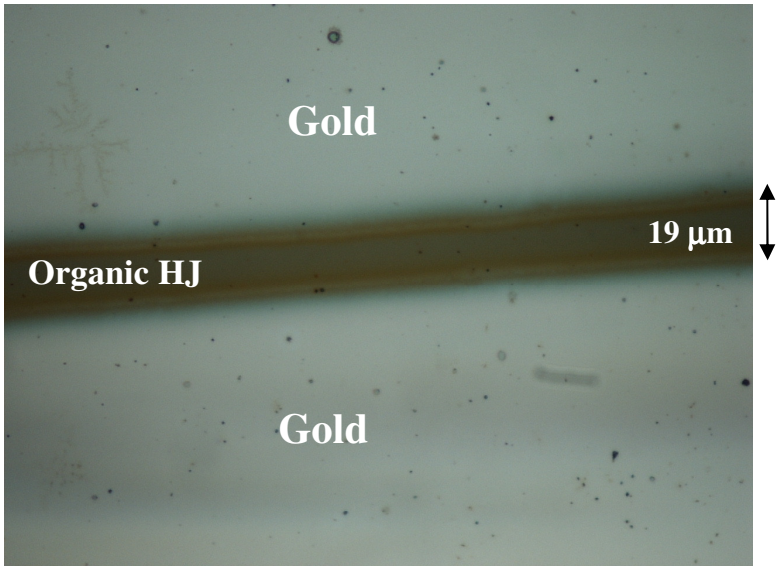

Fig. 2.5.11. Zoom-in of the gold top contacts shown in figure 2.5.11.

The optoelectronic characteristics of the three-layer vertical heterojuntion device are reported in WP6.

Deliverables of WP5

Table 2.5.1: Deliverables List

Del. no.	Deliverable name	Workpackage no.	Date due	Actual delivery date	Estimated indicative person-months *)	Used indicative person-months *)	Lead contractor

D11	Technology set for field-effect organic heterojunctions	5	M12	M12	4	4	IMEC
D18	Fabrication of organic heterojunction field-effect devices	5	M18	M18	10	13	IMEC

Table 2.5.2: Milestones List

Milestone no.	Milestone name	Workpackage no.	Date due	Actual delivery date	Lead contractor
M4	Technology for organic heterojunction field-effect devices assessed	5	M12	M12	IMEC

WP6. Organic heterojunctions characterization (WP leader: CNR)

The workpackage objectives were:

1. To characterise the suitable materials for ambipolar charge transport within the heterojunctions.
2. To perform electrical characterisation of the single materials and the heterojunctions.
3. To achieve a full optical characterisation of the emitting materials
4. To optimise the optoelectronic performances of the devices in order to achieve suitable pre-conditions for lasing.

Field effect transport materials and hybrid vertical/planar devices

In addition to the thorough characterization of the materials identified in WP1, a new electron-transporting material, DFHCO-4T, was investigated for use in the field-effect light-emitting device based on a vertical heterojunction.

DFHCO-4T, for which the molecular structure is shown in Figure 2.6.1, is an n-type material that was developed for use in electron-conducting thin-film transistors. This material, however, may also be useful in organic light-emitting field-effect devices based on a vertical heterojunction, since it fulfills the two criteria that are important for the device operation; DFHCO-4T has a high electron field-effect mobility, and its lowest unoccupied molecular orbital (LUMO, 3.9 eV) is lower than the LUMO of Alq_3 (2.8 eV) and DCM_2 (3.1 eV), making electron transport possible at the

heterojunction between the ETL and the light-emitting layer. In addition, similar to DFH-4T, DFHCO-4T has a larger band gab than PTCDI-$C_{13}H_{27}$, which results in low absorption in the red spectral region.

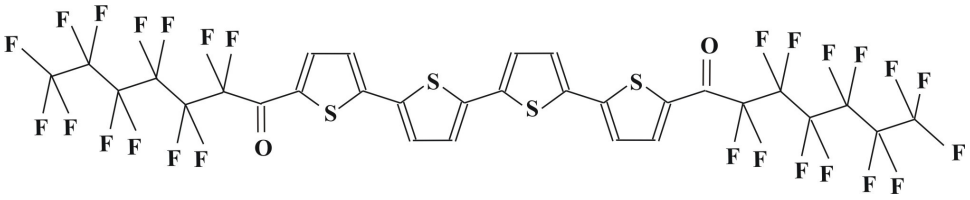

Figure 2.6.1. Molecular structure of DFHCO-4T

An electron field-effect mobility of 1.7 cm^2/Vs has been reported by Yoon et al. for the organic semiconducting material DFHCO-4T.[1] In these devices a top-contact geometry with Au source and drain contacts was used. To check whether also LiF/Al could be used as top contact material we have fabricated DFHCO-4T transistors with LiF/Al top contacts (0.8 nm LiF followed by 100 nm Al) and compared their performance to DFHCO-4T transistors having 100 nm Au as the top metal contact. Thin DFHCO-4T films were deposited by thermal vacuum evaporation of the material using the optimized growth conditions. Prior to the deposition of DFHCO-4T, a 5-nm thick PαMS layer was spincoated on top of the Si/SiO_2 substrate to provide a high-quality, electron-trap free surface allowing excellent electron transport.[2]

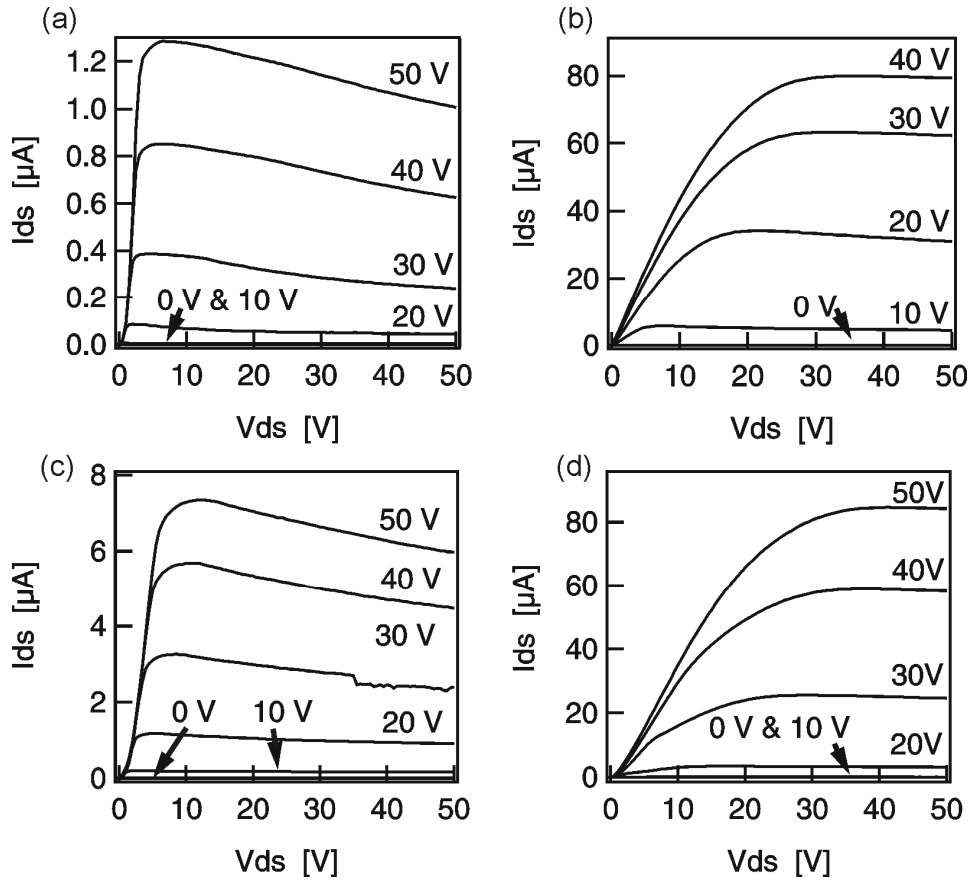

Figure 2.6.2. Output characteristics of DFHCO-4T transistors (W/L=2000/130) using (a) LiF/Al, (b) Au, (c) Yb, and (d) Ag top contacts.

Figure 2.6.2(a) shows the output characteristics of a transistor with 130 µm channel length and LiF/Al top contacts. For this device, an apparent field-effect electron mobility of 0.03 cm^2/Vs was calculated. This value is more than one order of magnitude lower than the electron mobility of DFHCO-4T previously reported using Au top contacts.[1] In addition, the OTFTs show strongly non-ideal characteristics, as apparent from a superlinear dependence of the current on the drain voltage at low bias, the saturation of the output current at a more or less fixed drain-to-source bias, and a decrease of the current at higher drain voltages. On the other hand, transistors fabricated under the same DFHCO-4T growth conditions but with Au instead of LiF/Al source-drain top contacts exhibit much better-behaved output characteristics with much higher drain currents (Fig. 2.6.2(b)). For Au top-contact transistors with 130 µm channel length, a mobility of 4.6 cm^2/Vs is measured. Such remarkable mobility achieved with Au contacts is of high technological relevance because for use in complementary logic it is preferable to use a single type of source and drain metal for both the p-type and the n-type OTFTs. The reproducibility of the results is quite good. The average apparent mobility, calculated from transistors with channel lengths between 50 and 200 µm is 3.5 cm^2/Vs. These field-effect mobilities are higher compared to previously reported results[1]

and we attribute this to the different growth conditions used to deposit DFHCO-4T. The fact that electrons can be efficiently injected from Au into DFHCO-4T despite an injection barrier of about 1 eV is not fully understood yet. The deep LUMO (3.96 eV) of DFHCO-4T and the fact that in a top-contact geometry there is a high gate-field that supports the injection of charges in a large source-gate overlap area[3] might be a possible explanation for this experimental observation.

The low apparent field-effect mobility (i.e., low output currents) and the non-ideal characteristics of DFHCO-4T transistors with LiF/Al top contacts compared to Au top contacts point to the presence of a current-limiting contact problem in the former. A plausible cause of this is the occurrence of a redox reaction between the n-type semiconductor and the Al metal contact. In fact, it is well known that ketone groups - present in the DFHCO-4T chemical structure - are easily reduced into their radical anions according to the reaction scheme shown in Figure 2.6.3(a). The electron transfer reaction is driven by the oxidation of a reactive metal, as for example Mg, Al, Fe and Zn (depicted in Figure 2.6.3(b) for Al) and the reduction of DFHCO-4T. The standard free energy (ΔG^o, Gibbs free energy) of the overall redox reaction depicted in Figure 7(c) can be calculated by $\Delta G^o=-nF\Delta E^o$, where n is the overall number of electrons exchanged between the oxidizing and reducing agents for the balanced redox equation, F the Faraday constant (96485 J/(V_mol)), and ΔE^o the standard cell potential (the difference in standard electrode potentials (SEPs) of both electrochemical couples).

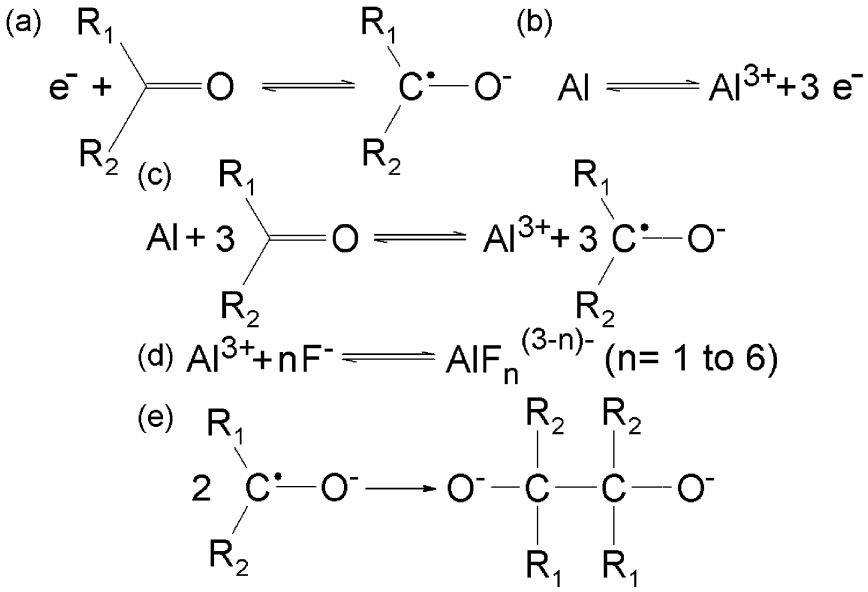

Figure 2.6.3. (a) Reduction of a ketone , (b) oxidation of Al, (c) redox reaction between a ketone and Al, (d) complexation of Al^{3+} by F^-, and (e) dimerization of a ketone radical anion.

For the Al/Al^{3+} couple the SEP in aqueous solution is -1.662 V vs the normal hydrogen electrode (NHE),[4] which is about -1.90 V vs the reference saturated calomel electrode (SCE).[5] Published value for the first reduction potential of DFHCO-4T in tetrahydrofuran is -0.88 V vs the SCE[6] Inserting this potential difference into the equation for ΔG^o, with n = 3 (Fig. 7(c)), gives ΔG^o = -296 kJ/mol, indicating that the reaction between Al and DFHCO-4T is highly exergonic and thus thermodynamically spontaneous.

Similar reductions of organic layers by evaporation of strongly reducing metals have been reported in literature. The reaction of Al evaporated on films of Alq_3 [7-10], $F_{16}CuPc$ [11] and PTCDA[12] for example were experimentally proven. The reduction of DFHCO-4T by evaporated Al (Fig. 7(c)) in our case is furthermore favored by additional side reactions. One of these reactions is the complexation of the Al^{3+} cation by fluoride ions (F^-) originating from an ultrathin (0.8 nm) LiF layer on top of the DFHCO-4T. In fact, F^- anions are well known to form stable complexes ($AlF_n^{(3-n)+}$ with n = 1 - 6, Fig. 7(d)) with Al^{3+} cations [13]. Furthermore, ketone radical-anions readily dimerize according the corresponding acyloinic species (Fig. 2.6.3(e)) [14]. Such additional processes will enforce the DFHCO-4T/Al redox reaction (Fig. 2.6.3(c)) towards the right side according to Le Chatelier's principle.

The products of the reactions displayed in Figure 2.6.3(c-e), an ionic salt and possibly dimerized ketone species, will form a thin interfacial layer between the unreacted DFHCO-4T and Al layers, hindering electron injection. In the case of Au this kind of reaction is impossible: the SEPs of the couples involving oxidation of Au are so high (+1.692 V vs NHE for Au/Au^+ and +1.492 V vs NHE for Au/Au^{3+}) [4] that a reaction with DFHCO-4T would be highly endergonic (ΔG^o = +225 kJ/mol in the case of Au/Au^+ and +619 kJ/mol for Au/Au^{3+}).

To find additional proof supporting the chemical reaction between Al and DFHCO-4T, we fabricated transistors using DFHCO-4T as the organic semiconductor but with two other top-contact metals: Ytterbium (Yb) and silver (Ag). The standard free energies for possible reactions between DFHCO-4T and Yb indicates that this kind of reaction is highly exergonic and thus spontaneous, independently if the Yb/Yb^{2+} couple (SEP: -2.76 V vs NHE [4], corresponding to ΔG^o = -409 kJ/mol) or Yb/Yb^{3+} couple (SEP: -2.19 V vs NHE [4], corresponding to ΔG^o = -449 kJ/mol) is considered. On the other hand, the corresponding value for the reaction of DFHCO-4T with Ag (SEP: +0.7796 V vs NHE [4] for Ag/Ag^+) is +139 kJ/mol, indicating that this reaction is impossible. The output characteristics of Yb and Ag top-contact transistors with 130 μm channel length are

shown in Figure 2.6.2(c) and (d). Transistors with Yb top contacts show similar output characteristics and low apparent field-effect mobility (0.06 cm^2/Vs) as LiF/Al transistors, whereas Ag top-contact transistors attain much higher currents and much better-behaved output characteristics. When Ag is used as top metal contact an apparent mobility of 1.7 cm^2/Vs was measured. These results are in agreement with our argumentation and give further evidence that a redox reaction occurs at the interface between DFHCO-4T and easily oxidizable metals, similar to Hirose et al.'s report that PTCDA reacts with Al, but not with Au and Ag [12].

The high electron field-effect mobility that can be obtained in DFHCO-4T combined with the low LUMO and the low aborption in the red spectral region makes DFHCO-4T particularly interesting for use as the electron-transporting material in organic light-emitting devices based on a vertical heterojunction. Devices comprising PTAA as the hole-transporing layer, Alq_3:DCM_2 as the light-emitting layer and DFHCO-4T as the electron-transporting layer have been fabricated. Because DFHCO-4T only function properly with contacts that have a low chemical reactivity such as Au and Ag, we used the inert contact metal Au to inject electrons in the device.

Devices are typically measured immediately after evaporation in an inert N_2 atmosphere using an Agilent 4156C parameter analyzer. A calibrated integrated sphere (SphereOptics Hoffman GmbH) is used for light intensity measurements and external quantum efficiency calculations. To determine the spectral characteristics, the emitted light is detected by means of an optical multichannel analyzer (OMA) in conjunction with a charge coupled device (CCD). These measurements are performed at room temperature in a cryostat to prevent photo-oxidation. The current-voltage characteristics, the light intensity and the electroluminescence spectrum of the fabricated devices are summarized in Figure 2.6.4. An external quantum efficiency of 0.08% was calculated, which is lower than the value obtained in devices using DFH-4T (0.25%), but still significantly higher than the one of PTCDI-$C_{13}H_{27}$-based devices (0.02%) [see WP5]. We attribute this increased efficiency compared to PTCDI-$C_{13}H_{27}$-based device, to the reduced light re-absorption in the red spectral region, where DCM_2 is emitting. Comparable to previous results, there is no significant reduction of efficiency up to the maximum current.

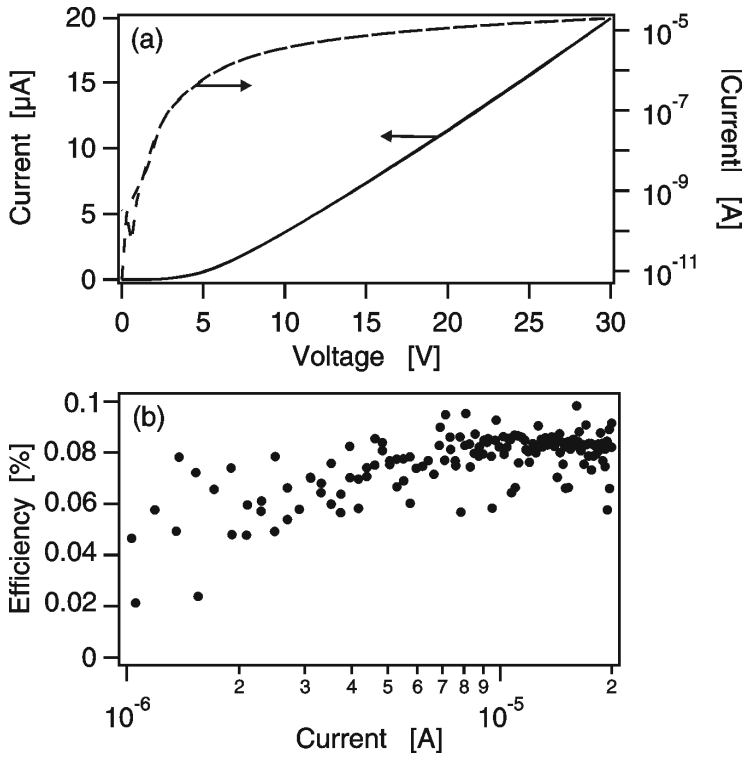

Figure 2.6.4. Measured characteristics of an OLED with field-effect-assisted electron transport comprising the wide band gap material DFHCO-4T as the electron-transporting material. The device has a width of 1 mm and a distance between the top electrode and the insulator edge of 6.7 μm. (a) Current-voltage characteristics, and (b) the external quantum efficiency as a function of the current.

Photonic properties of host-guest lasing systems

As mentioned in WP1, Triplet emitters, and in particular $Btp_2Ir(acac)$, was considered as a potential lasing material at the project onset. In order to verify the potential for lasing of $Btp_2Ir(acac)$, it was dispersed in poly(methyl metacrylate) (PMMA) matrix for checking the possibility to obtain optically pumped ASE. We prepared a 600 nm thick film of the Ir complex embedded in PMMA with 2% concentration so that in principle at least the first TE waveguiding mode should be supported. Since the refractive index of PMMA is about 1.49, and the glass was 1.46 such a small contrast has to be surmounted with a film thicker than for the case of Alq3 (in which 300 nm was more than enough). We find that even at very high pump energies (well above 10 mJ/pulse) no narrowing was observed whatsoever. This can be clearly seen in the left part of Fig. 2.33. For increasing pump energies, not only the PL intensity does not shown an increase in the slope, but in fact, it does show a slight decrease above 200 microjoules per pulse. This is also coupled to the FWHM, not showing any discernible variation with the pump energy.

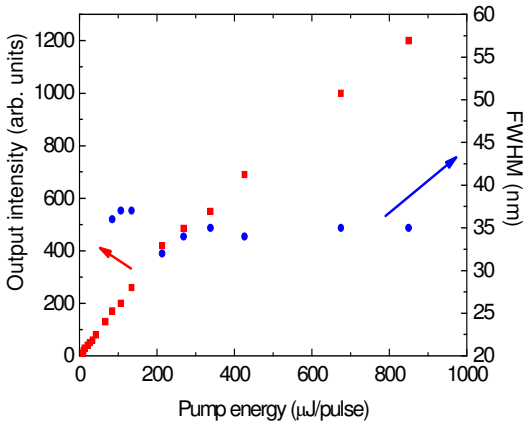

Fig. 2.6.5. PL output and FWHM of the PMMA:Btp2Ir(acac) 2% sample vs. pump energy.

In order to identify the mechanism responsible for the lack of ASE in the triplet emitter, time-resolved transmission changes for this material system were measured in a 4 μm thick PMMA:$Btp_2Ir(acac)$ film deposited on a quartz substrate. The sample was pumped at 400 nm wavelength while we have chosen the probe wavelength at the PL emission maximum at 614 nm. Figure 2.6.6 depicts the result of this experiment at an excitation laser fluence of 195 μJ/cm^2. In contrast to the Alq3:DCM singlet emitting reference sample, the transmission of the triplet emitting PMMA:$Btp_2Ir(acac)$ film drops by roughly $\Delta T/T_0 = -0.3\%$ after excitation at zero time delay. The observation indicates that this material exhibits transient absorption instead of showing gain at the wavelength of maximum PL emission. As a result, ASE, which requires a significant gain factor, cannot be supported in this triplet emitting system.

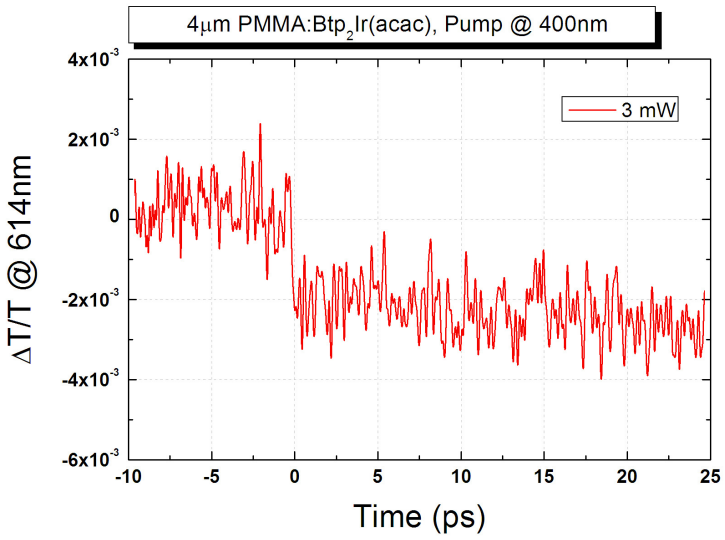

Fig. 2.6.6. Time-resolved transmission change of the 4 μm thick PMMA:Btp2Ir(acac) 2% sample. The excitation laser fluence was 195 μJ/cm^2 at 400 nm wavelength, the probe wavelength was chosen at 614 nm.

Photoluminescence and time-resolved spectroscopic experiments on the prototype triplet emitters btp2Ir(acac) has shown the absence of Amplified Spontaneous Emission even in samples carefully designed to match the refractive index and thickness requirements and excited with pulse energy as high as 800μJ/pulse. The reason for this behaviour has been identified in an effective excited state absorption, which competes with radiative emission, and therefore prevents ASE. Following this result, the consortium decided to focus the future work on singlet lasing emitters.

In addition to measuring optical gain of the reference host-guest system Alq_3:DCM2, we thoroughly investigated the optical properties of a possible alternative lasing system: the ter(9,9-diarylfluorene) (T3):DCM host guest matrix, already introduced in WP4.

We performed time-resolved spectroscopy investigation of the host-guest system by exciting with a femtosecond Ti:sapphire laser at 390 nm and collecting the PL spectra with a monochromator coupled to a streak camera (2.5 ps time resolution).
Contrary to the PL time decay of DCM dispersed in a PMMA matrix, the PL time decay in samples with increasing DCM concentration can no longer be fitted with a single exponential.
The 10% and 20% samples seem to have a similar temporal dynamics while the 2% sample behaves almost as the PMMA dye dispersed sample.
As expected, T3 PL gets progressively quenched with increasing DCM concentration. In particular for the 10% and 20% samples we cannot extract lifetime values from the decay curves since we almost reach the instrument temporal resolution limit.
Nevertheless for the 2% and partly for the 5% samples we were able to fit the host time decay by a Förster-transfer decay function, indicating that the emission of DCM occurs via a non-radiative long-range dipole energy transfer.

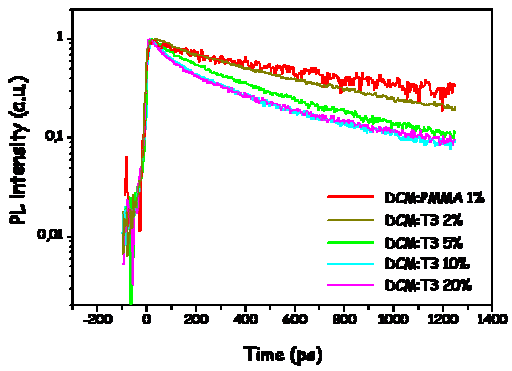

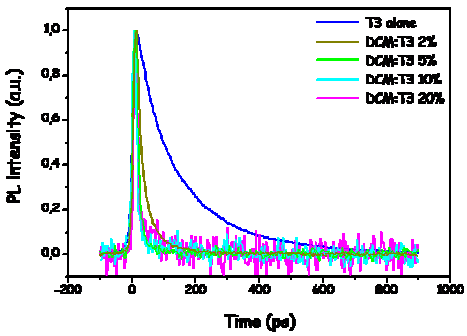

Fig. 2.6.7. PL time decay curves of T3:DCM blend when detection is centered at the DCM emission (top) and at the T3 emission (bottom).

For the low concentration DCM samples, we were able to observe an initial rise in PL intensity followed by a plateau at the intensity maximum and by the natural decay of the DCM excited state. The initial rise is attributed to the energy transfer process from T3.
From these data it is possibile to estimate a value of 60% for the energy transfer efficiency in the first 20 ps of the energy transfer process (about 75% of the entire energy transfer efficiency).

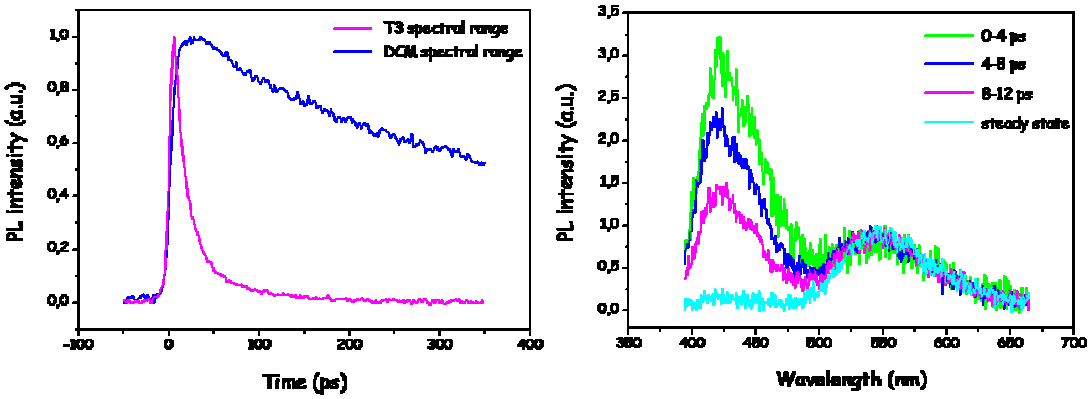

Fig. 2.6.8. Left: comparison between DCM- and T3-components PL time decay in the 2% sample. Right: temporal evolution in the first 12 ps of the energy transfer in the 2% sample (steady state PL for comparison).

From the data reported, the DCM concentration that guarantees an efficient energy transfer preventing DCM aggregation is around 2%. This is also confirmed by the amplified spontaneous emission (ASE) measurements performed on the same samples and it was determined that the 2% sample indeed had the lowest ASE value of 0.6 kW/cm^2.

	T3	2%	5%	10%	20%
ASE threshold [kW/cm^2]	4.4	0.6	1.1	2.8	3.8

Table 2.6.1 ASE threshold values of T3:DCM samples with different DCM concentration. The excitation source is the 355 nm line of a Nd:YAG laser with 25 ns pulse width. The excitation stripe is 4 mm^2. Samples thickness is around 150 nm.

This value is almost an order of magnitude lower than the ASE threshold value that we measured under the same conditions for the model system Alq3:DCM at 2% concentration.

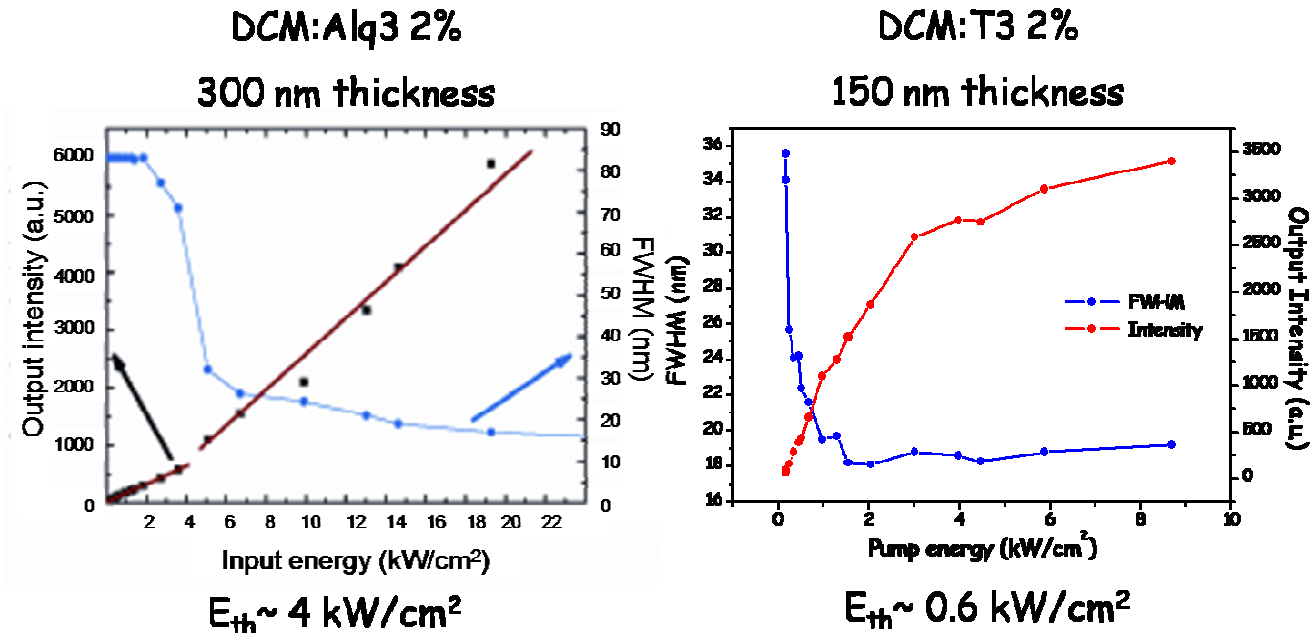

Figure 2.6.9. Comparison between the Alq3:DCM and T3:DCM ASE thresholds measured in the same experimental conditions.

A time-resolved analysis of the gain dynamics of T3:DCM were performed by RWTH and is presented here to allow for a comparison with Alq_3:DCM2.

Figure 2.6.10 (a) shows the differential change in transmission after pumping the sample at 400 nm at zero time delay. The probe wavelength was varied from 550 nm to 700 nm to cover the whole gain region assumed from ASE measurements. The excitation laser fluence was kept constant at 2.4 mJ/cm^2, which is clearly above the previously determined ASE threshold.

(a) (b)

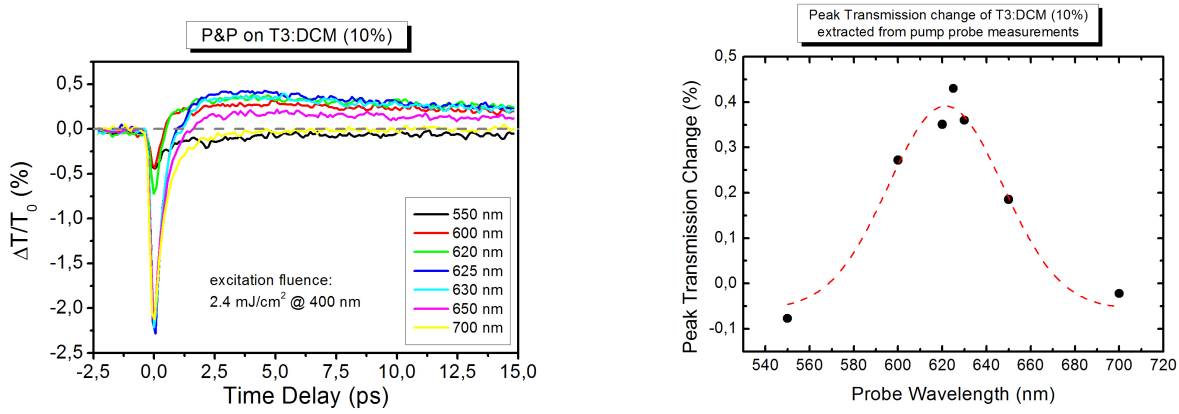

Figure 2.6.10. Time-resolved transmission measurements on T3:DCM for different probe wavelengths (a) and extracted positive transmission change peak values (b).

Upon excitation at zero time delay, the transmission shows an initial drop that recovers within the first picosecond. Depending on the probe wavelengths, this recovery is followed by an overshoot to positive transmission changes or the optically induced transmission change remains negative even on the longer time scale. The time delay between excitation and reaching the maximum transmission change can be identified as the energy transfer time from the optically pumped T3 to the DCM emitter. The transmission change remains positive on a timescale of ~ 30 ps. This positive transmission change is an unambiguous indication of gain at this wavelength, as optical transitions that could be bleached upon excitation are not observed in continuous wave absorption measurements in this wavelength range.

Figure 2.6.10(b) shows the relative transmission change at a time delay of 2.5 ps, which corresponds to the maximum transient transmission after optical excitation as function of the probe wavelengths. A Gaussian function is added to this graph as a guide-to-the-eye. The maximum transmission change at this time delay is observed at a 625 nm probe wavelength and agrees well with the ASE wavelength of 620 nm presented in the section WP4 of this report. Hence, the ASE wavelength can be correlated with the maximum gain wavelength in this host-guest system. For the 300 nm layer thickness of the investigated T3:DCM, the measured transmission change of $\Delta T/T_0$=0.4 % equals an optical gain of 133 cm^{-1}.

The work on field effect interfaces and heterojunctions dealt with the materials and material combination identified in WP1.

First, double layer heterojunction structures based on the combination of P13 and DH4T were investigated. Attention was paid to the growth conditions of P13 in order to achieve optimum conduction in field-effect transistor structures. In fact, P13 needs to be grown while keeping the substrate at a temperature higher than 60°C. We fabricated and analysed both the bi-layer heterojunctions shown in Figure 2.6.11. In one case the P13 is in direct contact with dielectric and the DH4T film is grown on top of the P13 film, in the second case the DH4T molecules are directly in contact with the SiO_2 surface. In Figure 2.6.11 are reported also the electrical transfer characteristics of the devices together with the electroluminescence collected during the device operation. The curves show a well balanced ambipolar behaviour in the case of DH4T/P13 heterojunction with mobility values for both holes and electrons equal to 3 10^{-2} cm^2 V/s. This result is comparable to the highest performances reported in literature for ambipolar organic field effect transitors obtained using pentacene and perfluoropentacene. In that case, however, no electroluminesce was observed during the device operation.

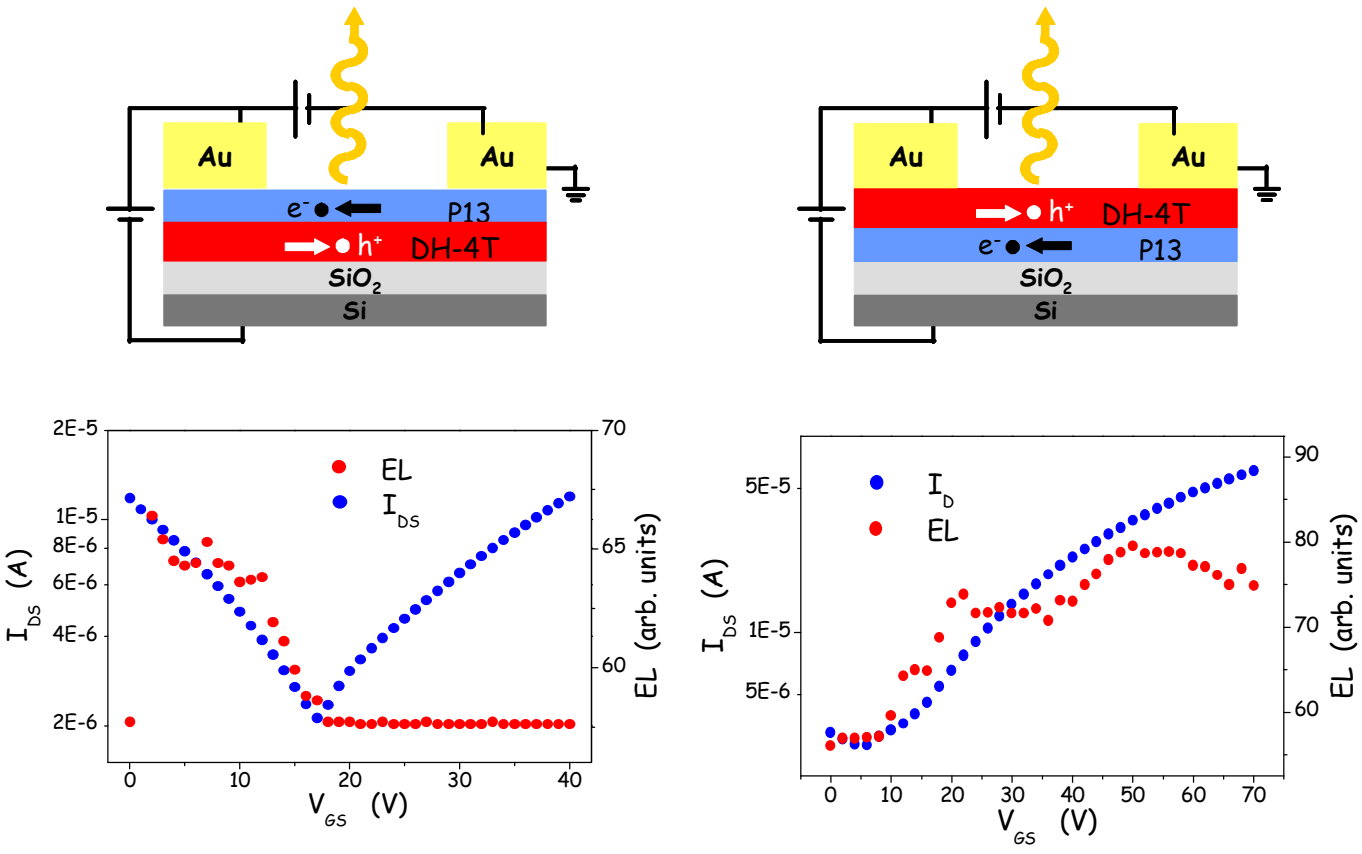

Fig. 2.6.11. Schematic of the device structures and electro-optical characteristics of light-emitting transistors based on DH4T/P13 and P13/DH4T heterojunctions.

In Figure 2.6.11 the drain-source voltage (V_{ds}) is set to operate in the saturation regime. The

transfer characteristics of DH4T/P13 devices show that the hole mobility does not vary substantially with respect to single layer devices, while the electron mobility falls by one order of magnitude despite the fact that P13 growth is carried out under optimized conditions. EL occurs in correspondence to hole transport and increases with increasing current. The output characteristics of P13/DH4T configuration exhibit an unbalanced transport: electron transport is more pronounced than hole transport as electron mobility drops by one order of magnitude with respect to the DH4T/P13 device. EL occurs in correspondence of electron transport and is proportional to the current. From this behaviour we can deduce that in Organic Light Emitting Transistors (OLETs) based on a bi-layer structure EL is always related to charge transport in the layer directly in contact with the substrate and follows a trend that is directly proportional to the current flowing through the device.

In addition to the bilayer device structure, the light–emitting field-effect transistor devices based on the three layer vertical heterojunction described in WP1 was performed at CNR. First, bilayer heterojunctions of α,ω-diperfluorohexyl-4T (DHF4T) and p-(α,ω)-dihexyl-quaterthiophene (DH4T) were characterized in a top contact field-effect configuration (see figure 2.6.7). DHF4T and DH4T will be used as n-type and p-type materials in the three layer heterojunction structure. However, it is important to first verify the electrical and optoelectronic properties of the bi-layer heterojunctions before introducing the light emitting layer. In this way it will be possible to determine how the inclusion of the emitting layer affects charge transport and light emitting characteristics of the devices.

The schematic of the bi-layer heterojunctions device is reported in Figure 2.6.12. Both the DHF4T and DH4T layers were grown at a rate of 0.2 Å/s with the substrate at room temperature. Following the results of the morphological analysis of the individual layers (see WP4), the DHF4T layer thickness was 7nm while that of DH4T was 20nm.

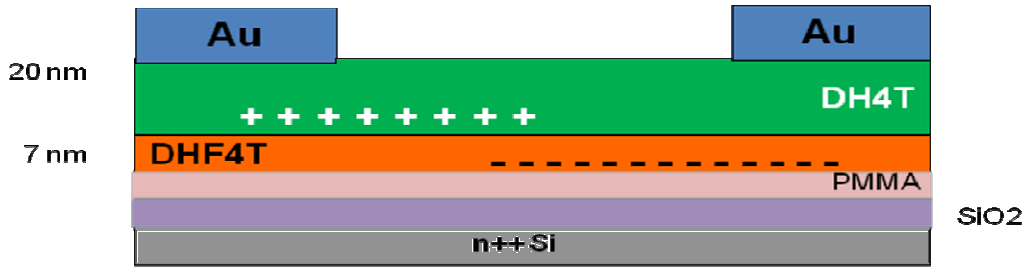

Figure. 2.6.12. Schematic of the field-effect device structure based on the DHF4T/DH4T bi-layer heterojunction. Channel length is L=600 μm and channel width is W=10mm.

The I-V p-type and n-type transfer and output curves of the DHF4T/DH4T bi-layer device of figure 2.6.12 are reported in Figure 2.6.13.

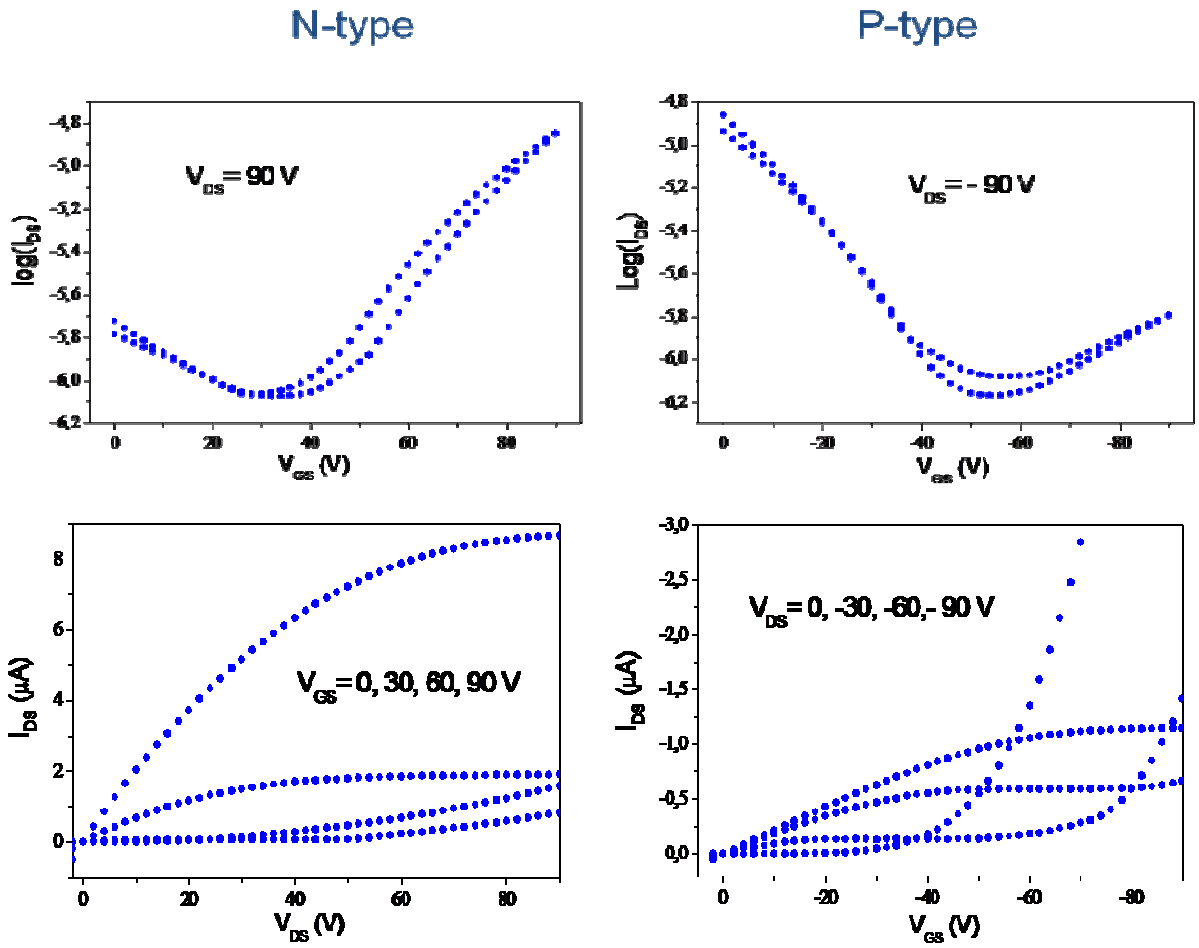

Figure 2.6.13. n-type and p-type transfer curves (top), and n-type and p-type output curves (bottom) of the DHF4T/DH4T bi-layer device.

The IV curves clearly show that the device exhibits an ambipolar behavior of the device. The saturation of n-type and p-type mobilities are μ_n = 5 10^{-2} cm^2V/s and μ_p =1 10^{-3} cm^2V/s. The gate threshold voltages for n-type and p-type operation are V_{Tn} = 31 V and V_{Tp} = -2 V. No electroluminescence emission could be detected from this device.

The device structure comprising a three layer vertical heterojunction is schematically reported in figure 2.6.14. Each layer of the heterojunction was grown using the growth parameters that afforded the best interfacial characteristics as determined by the morphological analysis reported in WP4.

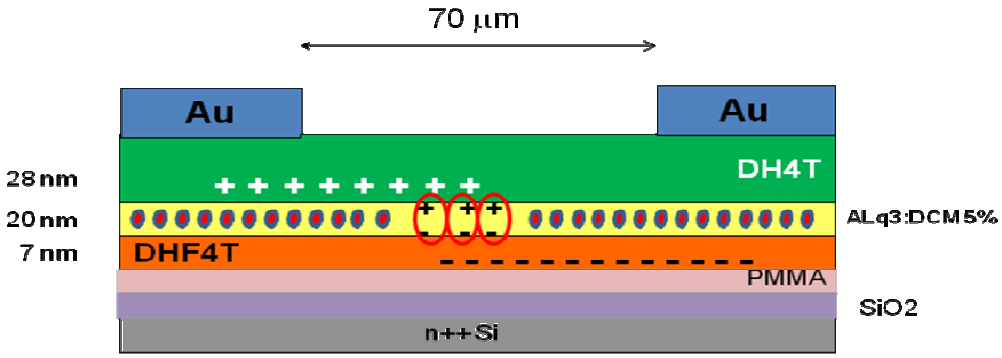

Figure 2.6.14. Schematic of the light-emitting field-effect device structure based on a three layer heterojunction. The nominal thickness is reported beside each layer. DCM concentration in the Alq3 matrix was 5% in weight.

The transfer curves of the three layer heterojunction device shown in figure 2.6.149 are reported in figure 2.6.15 together with the corresponding electroluminescence emission.

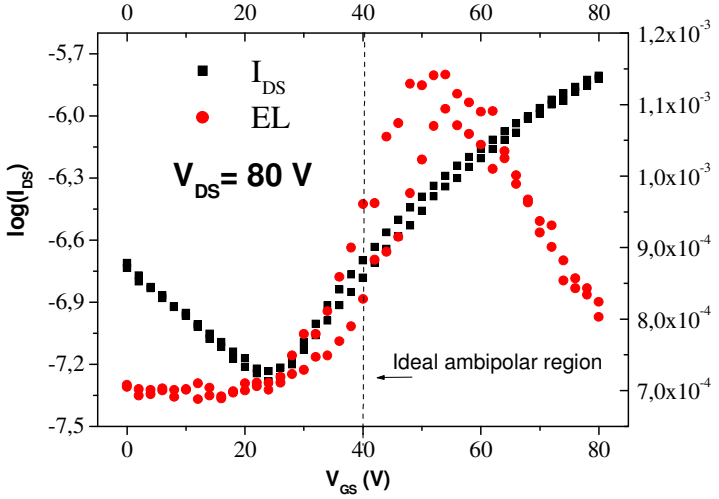

Figure 2.6.15. n-type transfer curves and electroluminescence emission (onward and backward voltage scans) of the three layer heterojunction device shown in figure 2.6.9. Channel length is L=150 μm and channel width is W=10 mm.

The device maintains the ambipolar electrical character observed for the bi-layer heterojunction one, and in addition electroluminescence is generated due to charge recombination in the host-guest emitting layer. The saturation mobility and the gate threshold voltage are $\mu_N=10^{-3}$ cm^2V/s and V_{TN}= 10 V for electrons, and $\mu_P=6.2\ 10^{-5}$ cm^2V/s and V_{TP}= -20 V for holes. As expected the presence of the emitting layer induces a degradation of the p-type transport characteristics evidenced by a decrease in the hole mobility by more than one order of magnitude. However, the electroluminescence intensity is clearly observed at a relatively low voltage, which is an indication of preferential charge recombination in the intermediate emitting layer. Interestingly it is observed

that the light generation occurs in the ambipolar region of the device operation, which indicates exciton formation and light emission in the central part of the channel active area. Even more important is the observation of a peak with an emission intensity located in the range 45 - 55 volts in the both n-type and p-type transfer curves. This indicates that the maximum of exciton recombination efficiency takes place when the electron and hole current are balanced within the device. The current density in the active area of field-effect devices can be estimated considering that charge carriers in the transistor channel are accumulated in the first 1.5 nm close to the relevant interface, either with the dielectric or with the underneath organic layer.
The current density achieved in this device at the highest measured current values is 8 A/cm^2 for electrons and 4.6x10^{-1} A/cm^2 for holes. Although the measured device characteristics are encouraging, it is clear that the electron and hole mobility values, as well as the current densities, need to be substantially improved.

By further optimization of the device fabrication process, and in particular by decreasing the channel length to 85 µm, we find a substantial increase of the n- and p-type electrical currents (see figure 2.6.16). The n-type mobility is enhanced to $\mu = 5x10^{-2}$ cm^{2}V/s with a gate threshold voltage for electrons of $V_{TN} = 14.5$ V. The p-type mobility also improves by two orders of magnitude and reaches $\mu = 4.5x10^{-3}$ cm^{2}V/s with a gate threshold voltage as low as $V_{TP} = 5$ V.

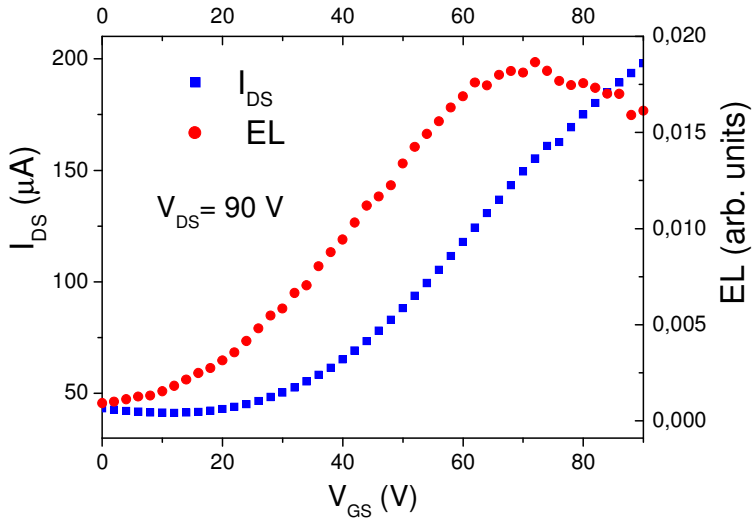

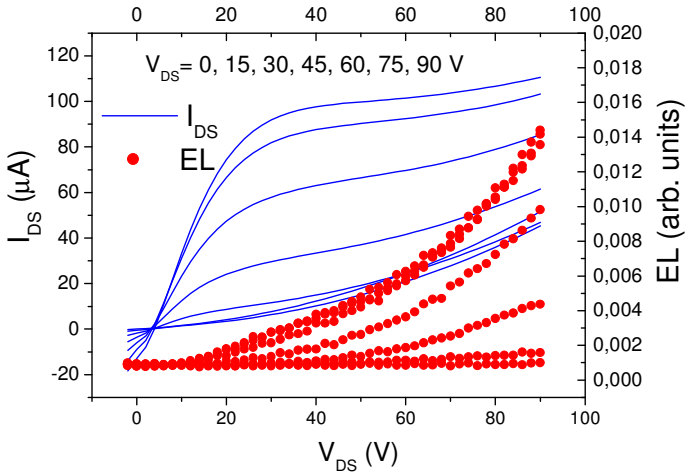

Figure 2.6.16. I-V transfer and output curves and corresponding electroluminescence emission of a three layer heterojunction device with channel length L=85 μm and channel width W=10 mm.

We have determined that this last device affords n-type current densities of 1 kA/cm^2 and p-type current densities of 0.2 kA/cm^2, that are the highest reported current density values for field-effect light-emitting transistor devices to date.

Evaluation of the charge-induced losses in the tri-layer vertical heterojunction device under electrical bias condition

As charge carrier injection into the organic layer is assumed to increase optical absorption, the knowledge and control of these losses is crucial for the performance of the envisaged electrically pumped organic laser device. To determine the electroabsorption of an organic heterojunction, a sample for optical transmission experiments based on the vertical heterojunction based device structure was designed that comprises electrical contacts for biasing. The device was grown on top of a glass/ITO substrate acting as gate contact. The thickness of the ITO film is equal to 150 nm. The sample dielectric was obtained by spin coating 420 nm of PMMA on top of the ITO film. The device active region is formed by a tri-layer structure. The first organic layer was evaporated directly on top of the PMMA and correspond to a 20 nm-thick film of DH4T. The second layer, grown on top of the DH4T film, is formed by a 20-nm Alq3:DCM2 2% coevaporated matrix. The third evaporated layer correspond to a 15 nm-thick film of P13. The 50 nm thick drain and source top-electrodes were made of gold. In a first step no photonic feedback structures were included in the sample. The transmissivity of the sample is measured with a white light probe beam delivered from a fiber based supercontinuum light source. The probe beam is focused at perpendicular incidence within the 200μm wide channel of the planar FET device and the transmitted light through the sample stack is spectrally dispersed by a monochromator and detected by a photo receiver. Electrical biasing is provided by an electrical network analyzer, allowing for the individual driving of all contacts of the FET device. During the measurements the source contact is connected

to the ground level and the drain-source-voltage is kept at constant levels of -80V, 0V or +80V. To increase the sensitivity of the setup, a lock-in detection scheme is used. For this purpose, a periodic square wave of -80V peak level is applied to the gate contact to control operation of the FET device. To ensure that the sample reaches a steady state in each operation condition the modulation frequency is set as low as 1Hz, thus requiring a long integration time of 15s for each recorded transmission value. For the first set of electroabsorption measurements, a constant drain-source voltage of -80V is applied. The modulation of the gate-source voltage leads to a modulation of the drain current between -0.3 µA (gate-source voltage on) and -0.04 µA (gate-source voltage off). Figure 2.6.17 displays the measured current induced change in transmission of the FET structure versus detection wavelength in the range from 500 to 750nm.

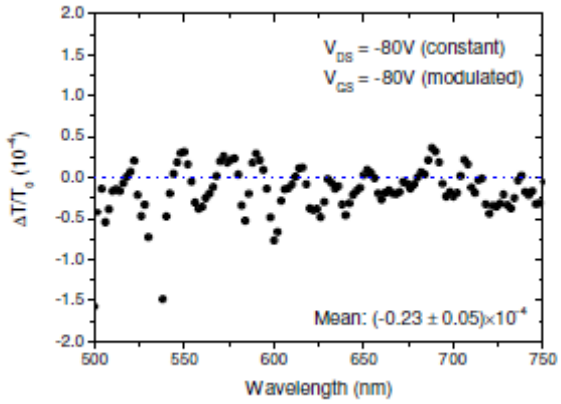

Figure 2.6.17. Electrically induced change in transmission of the FET device due to driving the gate contact at -80V. The drain-source voltage is kept constant at -80V.

Within the noise level of the measurement, no dependence on the detection wavelength can be derived. The mean value of ΔT/T over the whole wavelength range is -0.23×10^{-4} and therefore hints on a weak additional absorption due to driving the FET device electrically. A higher accuracy of this value necessitates a further improvement on the measurement setup and is not available at this time. Nevertheless, the indicated value allows us to estimate an upper limit of the additional absorption within the electrically pumped device. Taking the thickness of the organic layer stack into account, we can calculate a additional absorbance lower than $\Delta\alpha = 4.2/cm^{-1}$. In Figure 2.6.18 the results of an electroabsorption measurement is plotted where the drain contact is connected to ground. In this configuration, no drain current flows, but carriers are accumulated in the organic layer near the gate electrode.

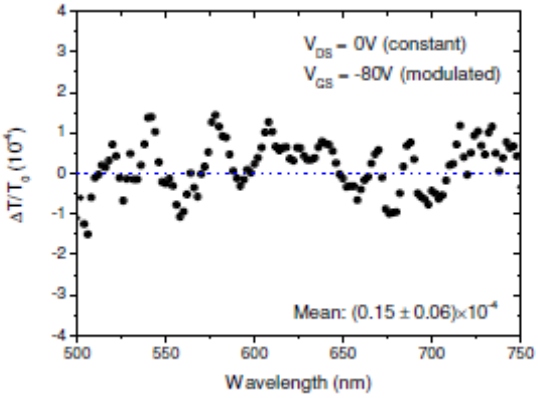

Figure 2.6.18. Electrically induced change in transmission of the FET device due to driving the gate contact at -80V. The drain-source voltage is kept constant at 0V.

Again, no dependence on the detection wavelength is observable on the relative change in transmission within the noise level. The calculation of the mean value reveals a slightly positive value of 0.15×10^{-4} from which a reduction of absorbance $\Delta\alpha = -2.7/cm^{-1}$ can be estimated. The results of the complementary measurement at +80V drain-source voltage are shown in Figure 2.6.19. Here the modulation of the gate voltage leads to a modulated drain current of 3µA (gate-source voltage on) and 0.3µA (gate-source voltage off). Again, no dependence on detection wavelength but a slight additional absorption due to electrical bias is observed. We calculate an upper limit for the relative change of absorbance of $\Delta\alpha = 3.3/cm^{-1}$.

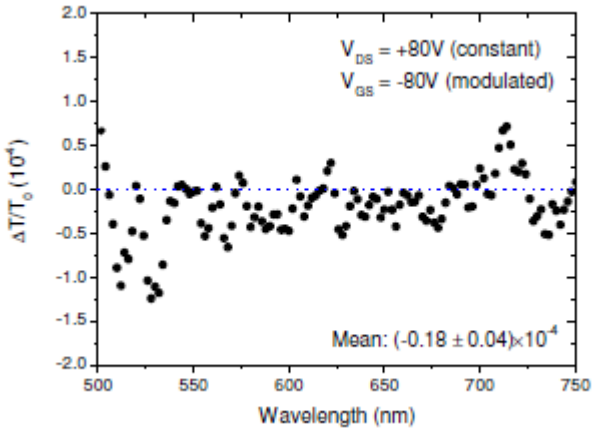

Figure 2.6.19. Electrically induced change in transmission of the FET device due to driving the gate contact at -80V. The drain-source voltage is kept constant at +80V.

The upper limit for the electrically induced additional absorption in all three measurements is far below the earlier achieved optical gain in Alq3:DCM2 of $500cm^{-1}$. Thus we may expect that the laser threshold does not increase significantly in an electrically pumped organic laser device.

References

[1] M. Yoon, C. Kim, A. Facchetti, T. J. Marks, *J. Am. Chem. Soc.,* **2006** *, 128* , 12851.

[2] L. Chua, J. Zaumseil, J. Chang, E. C. Ou, P. K. Ho, H. Sirringhaus, R. H. Friend, *Nature*, **2005**, *434*, 194.

[3] J. Zaumseil, C. L. Donley, J. Kim, R. H. Friend, H. Sirringhaus, *Adv. Mater.,* **2006** *, 18* , 2708.

[4] *CRC Handbook of Chemistry and Physics*, **85**th edition, edited by D. R. Lide (CRC Press (Boca Raton), 2004-2005), pp.8.23-8.33.

[5] A. J. Bard and L.R. Faulkner, *Electrochemical Methods: fundamentals and Applications*, **2**nd edition (Wiley&Sons, 2001), p. 809.

[6] M. Yoon, S. A. DiBenedetto, A. Facchetti, T. J. Marks, *J. Am. Chem. Soc.,* **2005** *, 127* , 1348.

[7] Q. T. Le, L. Yan, Y. Gao, M. G. Mason, D. J. Giesen, and C. W. Tang, *J. Appl. Phys.* **2000**, *87*, 375

[8] M. G. Mason, C. W. Tang, L. S. Hung, P. Raychaudhuri, J. Madathil, D. J. Giesen, L. Yan, Q. T. Le, Y. Gao, S. T. Lee, L. S. Liao, L. F. Cheng, W. R. Salaneck, D. A. dos Santos, and J. L. Brédas, *J. Appl. Phys.* , **2001**, *89*, 2756

[9] C.-I. Wu, G.-R. Lee, and T.-W. Pi, *Appl. Phys. Lett.* **2005**, *97*, 212108

1. [10] C. Shen, A. Kahn, J. Schwartz, *J. Appl. Phys*. **2001**, *89*, 449
2. [11] C. Cheng, A. Kahn, J. Schwartz, *J. Appl. Phys*. **2001**, *90*, 6236

3. [12] Y. Hirose, A. Kahn, V. Aristov, P. Soukiassian, V. Bulovic, S.R. Forrest, *Phys. Rev. B*, **1996**, *54*, 13748

[13] M. S. Corbillon, M. A., Olazabal, and M. Madariaga, *J. Sol. Chem.* **2008**, *37*, 567

[14] H. G. O. Becker, R. Beckert, G. Domschke, E. Fanghänel, W. D. Habicher, P. Metz, D. Pavel, and K. Schwetlick, *Organikum*, **21**st edition (Wiley-VCH (Weinheim), 2001), chap. D.7 Reaktionen von Carbonylverbindungen, pp.586-587.

Table 2.6.2: Deliverables of WP6

Del. no.	Deliverable name	Workpackage no.	Date due (month)	Actual delivery date	Estimated indicative person-months *)	Used indicative person-months *)	Lead contractor
D12	Transport and emitting materials for field-effect organic heterojunctions	6	M12	M12	3	3	CNR
D16	Characterisation of host-guest emission systems and transport materials	6	M15	M15	9	10	CNR

D22	Technical analysis of the opto-electronic properties of organic heterojunctions	6	M24	M30	4	6	CNR

Table 2.6.3: Milestones of WP6

Milestone no.	Milestone name	Workpackage no.	Date due	Actual delivery date	Lead contractor
M7	Final choice of organic materials for heterojunctions	6	18	18	CNR

WP7. Optically pumped laser in field-effect devices (WP leader: IBM)

The objective of this workpackage was to measure the optically pumped lasing properties of the organic heterojunctions integrated into field-effect devices.

ASE properties of the three-layer vertical heterojunction device under optical pumping

Amplified Spontaneous Emission (ASE) has been measured by CNR in the complete device structure based on the tri-layer vertical heterojunction. The devices opto-electronic characteristics and the working principle of the three-component approach have been reported in WP1 and WP6. The effect of the gate and the drain-source contacts on ASE properties has been separately evaluated. In Fig.2.7.1 is reported the scheme of the fabricated sample for the ASE measurements.

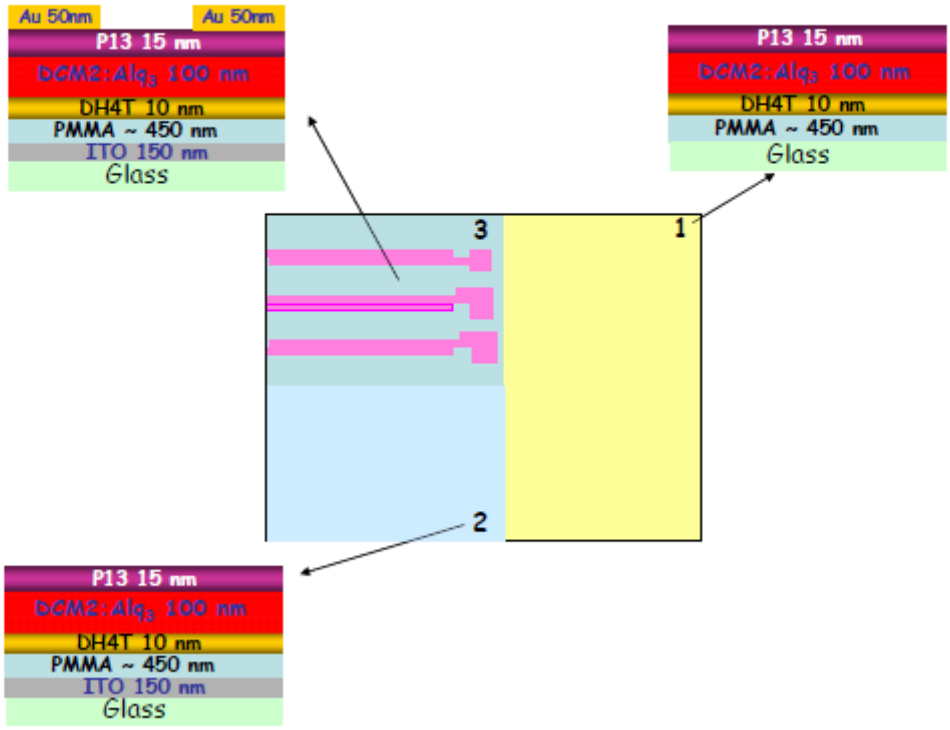

Figure 2.7.1. Scheme of the sample realized for performing ASE measurements on the tri-layer heterojunction. The three different configuration obtained are located in the substrate regions labeled respectively by 1, 2 and 3. The corresponding side views of the sample are also reported.

The ASE properties of the tri-layer heterojunction were measured exciting with the third harmonic of a Q-switched Quantel Nd:YAG laser delivering 25 ns-long pulses at 355 nm with a 10 Hz repletion rate. The output intensity of the laser was controlled by using neutral density filters and the pumped energy was monitored using a calibrated laser power and energy meter (Scientech). An adjustable slit and a cylindrical lens were used to shape the laser beam into a strip with a width of 1 mm and a length of 4 mm. The films were pumped at normal incidence with the long axis of the pump beam perpendicular to the edge of the sample. The output signal was focus on a fiber-coupled Hamamatsu multichannel optical analyzer by a lens system. Measurements were performed in vacuum at a pressure of 10^{-5} mbar .

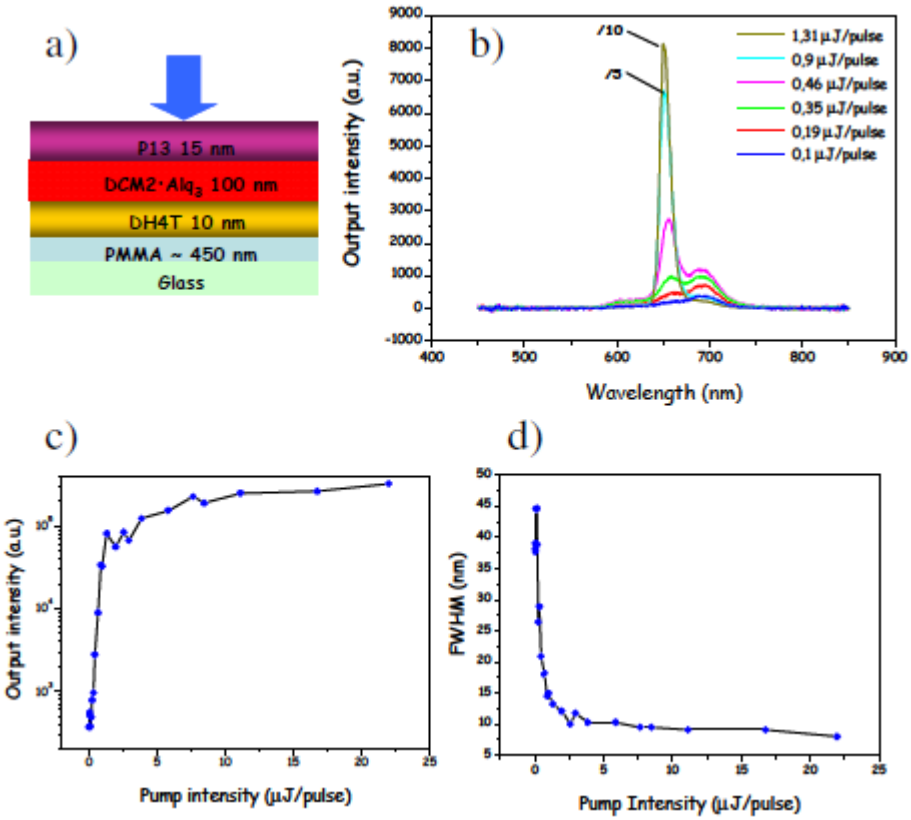

Figure 2.7.2. ASE measurement of the tri-layer heterojunction on glass. a) sample configuration, the arrows indicate light pumping direction; b) emission spectra collected from the edge of a 4 mm^2-wide excitation stripe as function of the pump energy; c),d) dependence of the photoluminescence intensity and full width at half maximum (FWHM) on the excitation pump intensity.

In Fig. 2.7.2(b) the clear spectral narrowing of the photoluminescence (PL) with increasing pump intensity is reported. The energy position of the peak showing the super-linear intensity enhancement is at around 660 nm and can be attributed to the 0-1 DCM optical transition (note that some emission wavelength shifts is induced by the film thickness). The full width at half maximum (FWHM) values versus pump intensity reported in figure 2.7.2(d) show clearly the knee-shaped feature typical of the ASE process. The ASE threshold is located in correspondence of 2,5 µJ/pulse pump intensity. We can conclude that the tri-layer heterojunction grown on top of a glass/PMMA substrate presents optically-pumped ASE for low threshold pump energy values. This means that the introduction of the PMMA film as well as the p-transport DH4T and the n-transport P13 films does not affect the optical properties of the Alq3:DCM2 lasing system.

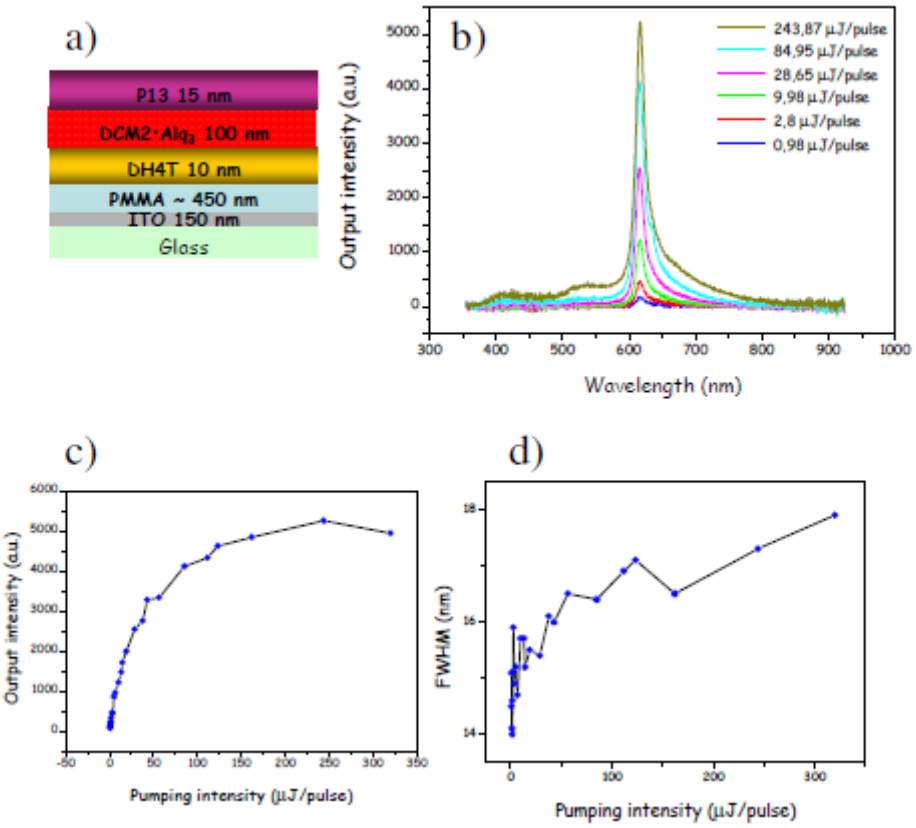

Figure 2.7.3. ASE measurement of the tri-layer heterojunction on ITO. a) sample configuration, the arrows indicate light pumping direction; b) emission spectra collected from the edge of a 4 mm^2-wide excitation stripe as function of the pump energy; c),d) dependence of the photoluminescence intensity and full width at half maximum (FWHM) on the excitation pump intensity.

When the tri-layer heterojunction is grown on top of a glass/ITO/PMMA substrate, the spectral narrowing disappears even if high pump intensity is used. In figure 3b the sample emission as a function of the pump energy is reported. We find an enhancement of the output intensity in correspondence of 600 nm: this feature could be associate to the DCM2 0-0 transition but no corresponding spectral narrowing is observed. The intensity increases by a factor 5 with pump intensity increasing from ~1 µJ/pulse to ~100 µJ/pulse while, in the previous case, the emission intensity gained a factor 102 in correspondence to the same pump intensity range. Moreover this peak is present in PL spectrum even if the pump intensity is very low. The FWHM values reported in Fig. 2.7.3(d) are spread around 16 nm without any evidence of the step feature typical of the ASE transition. In this case we can conclude that no ASE takes place in the Alq3:DCM2 2% matrix because of the presence of the ITO at the bottom of the organic heterojunction. The reasons of this behaviour can be related to the boundary condition imposed by the conducting ITO sheet to the

electromagnetic field in the active region as well as to the diffusion and absorption effects induced by the high refractive index ITO film. Deeper investigations are needed in order to clearly understand the optical behaviour of the heterojunction grown on top of ITO.

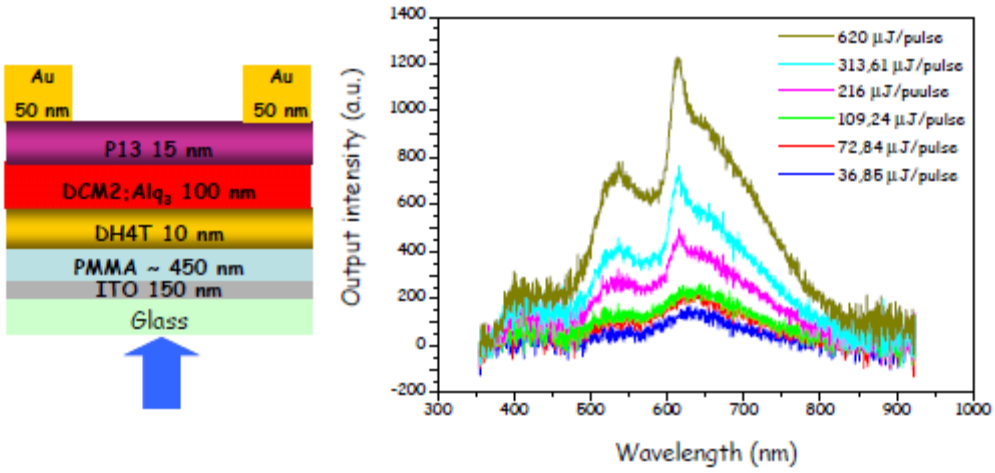

Figure 2.7.4. ASE measurement of the tri-layer heterojunction in the complete device configuration. a) sample configuration, the arrows indicate light pumping direction; b) emission spectra collected from the edge of a 4 mm^2-wide excitation stripe as function of the pump energy.

When the ASE measurements are performed in the real device configuration (Fig. 2.7.4) the exciton quenching effects and optical losses become more dramatic. In this case the output intensity value reached by pumping with 620 µJ/pulse (Fig. 2.7.4(b)) is about one order of magnitude lower than the value obtained from pumping the portion of the substrates without the drain/source contacts using a comparable pump energy value. In Fig. 2.7.4(b) we can recognize the 0-0 DCM2 peak increasing with pump intensity. In the 700 nm spectral region there is the evidence of a spectral feature ascribed to the P13 and in the high energy part of the spectrum the two peaks at about 400 nm an 550 nm are more pronounced that in the previous measurements (Fig. 2.7.3). Also in this case no ASE is observed. We can conclude that the presence of gold top contacts enhance the PL quenching without affecting substantially the spectral response of the organic system with respect to the glass/ITO/PMMA case, while the inclusion of the ITO film below the PMMA dielectric film changes completely the tri-layer PL spectral distribution and prevents the optically pumped ASE formation.

Optically pumped lasing experiments in field-effect organic heterojunctions

In WP4 it has been shown that we are able to observe optically pumped lasing from a device with the complete material stack including hole- and electron transport layers. Lasing could be observed

for gain layers of only 10 nm thickness. In addition, we showed that the presence of PTAA does not change the laser threshold pump power significantly compared to Alq3 for thick gain layers. Alq3 was the electron transporting layer used in WP4. This electron-transporting materials, however, cannot be used in the hybrid devices structure based on a vertical organic heterojunction, because it does not conduct electrons in a thin-film transistor configuration. Indeed, in the hybrid device structure, electrons are transported towards the light-emission zone by field-effect. Thanks to the high field-effect mobility that can be achieved in this way, electrons can be transported over several micrometers, minimizing the absorption losses at the metallic contacts. However, since the non-planar molecular structure of Alq3 prevents the formation of an electron accumulation channel in Alq3 other electron-transporting materials have to be used. Therefore, optically pumped lasing experiments were performed on material stack including hole- and electron transporting layers which are of direct use in electrically pumped devices, particularly in the hybrid device structure based on a vertical/planar organic heterojunction.

Organic light-emitting field-effect devices have been fabricated and characterized using three different electron-transporting materials: PTCDI-C13H27, DFH-4T and DFHCO-4T. These thee materials fulfill the two criteria that are important for device operation; they have a high electron field-effect mobility, and their lowest unoccupied molecular orbital (LUMO) is slightly lower than the LUMO of Alq3 and DCM2, making electron transport possible at the heterojunction between the ETL and the light-emitting layer. In addition, DFH-4T and DFHCO-4T have a larger band gap than PTCDI-C13H27, which results in low absorption in the red spectral region. This is illustrated in Figure 2.7.5, which shows the normalized absorption spectra of PTCDI-C13H27, DFH-4T and DFHCO-4T, and the normalized photoluminescence spectrum of Alq3:DCM2. The absorption spectrum of DHF-4T and DFHCO-4T is clearly blue-shifted with respect to the emission of DCM2. The emission spectrum of Alq3:DCM2 and the absorption spectrum of PTCDI-C13H27 on the other hand, display a significant overlap, indicating that photons emitted by DCM2 will be strongly re-absorbed by PTCDI-C13H27.

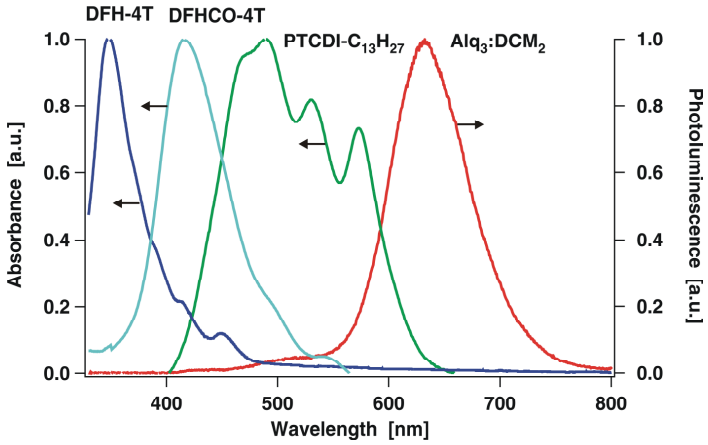

Figure 2.7.5. Normalized photoluminescence spectrum of a thin film of Alq3 doped with 2% of DCM2 and the normalized absorption spectra of PTCDI-C13H27, DFH-4T and DFHCO-4T thin films.

Because of the low absorption in the red spectral region, the losses under optical pumping are expected to be lower for samples comprising DFH-4T and DHCO-4T compared to samples comprising PTCDI-C13H27. However, also other factors, such as surface roughness and film morphology of the electron-transporting material may influence the laser threshold. Thin DFH-4T films deposited by vacuum thermal evaporation show Stransky-Krastanov growth. This implies that the growth of the first few DFH-4T monolayers is two dimensional (2D). However, beyond a certain thickness threshold the film starts to roughen strongly and the growth becomes three dimensional (3D). In the case of DFH-4T films, this 3D growth manifests itself in the formation of thick elongated needles. Figure 2.7.6 shows an atomic force microscopy (AFM) topography image of a 50-nm thick DFH-4T film grown on top of PTAA. Similar growth was observed for DFHCO-4T.

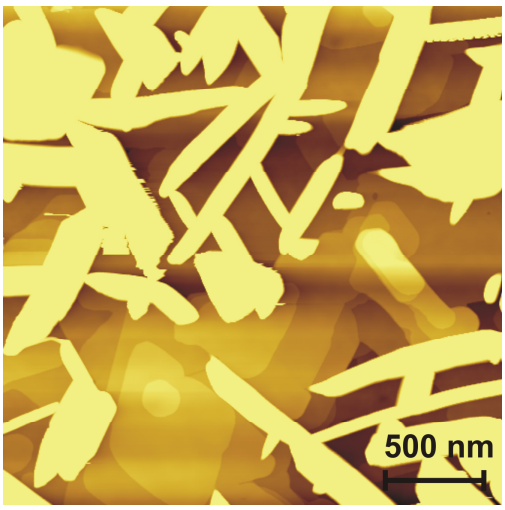

Figure 2.7.6. 2.5 µm x 2.5 µm AFM topography image of a 50-nm thick DFH-4T film grown on top of PTAA.

The rough growth of DFH-4T and DFHCO-4T might be problematic for achieving lasing, therefore it is important to reduce the amount of 3D needles as much as possible. We found that the size of the 3D needles strongly depends on the deposition rate. Increasing the deposition flux reduced their height from ~300 nm to ~100 nm. Increasing the substrate temperature did not really affect the height of the needles but lowered slightly their density. The nature of the substrate on the other hand, did not appear to strongly influence the morphology of 50-nm-thick films, which is in agreement with previous results. An overview of the morphology of DFHCO-4T grown on top of PαMS using different fluxes and substrate temperatures is given in Figure 2.7.7. 3D growth could be largely suppressed by deposition at high substrate temperatures and high deposition flux.

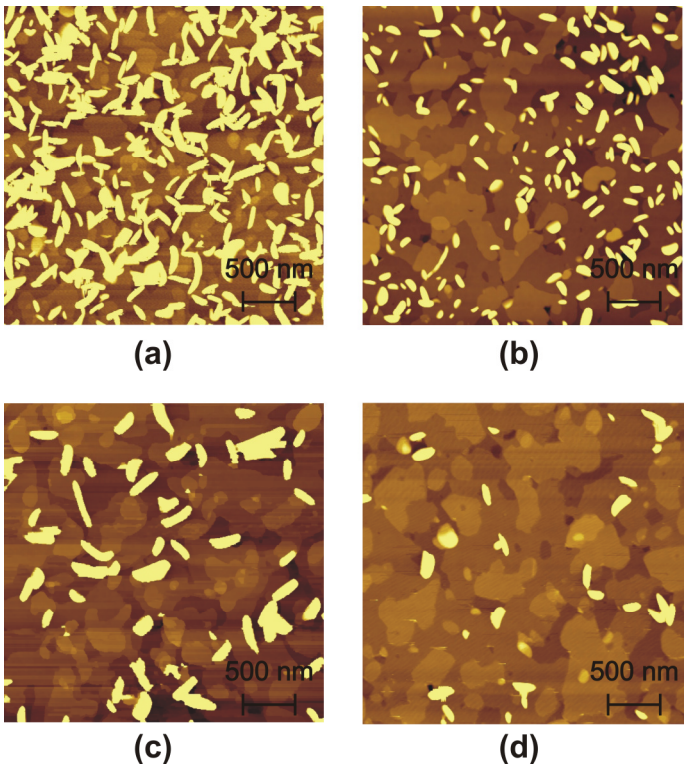

Figure 2.7.7. 3 µm x 3 µm AFM scans of DFHCO-4T grown on top of PαMS using different fluxes and substrate temperatures: (a) flux = 0.2 Å/s and Tsub = 25 °C, (b) flux = 4.5 Å/s and Tsub = 25 °C, (c) flux = 0.2 Å/s and Tsub = 70 °C , and (d) flux = 4.5 Å/s and Tsub = 70 °C.

3D growth could be further minimized by reducing the organic layer thickness. However, a minimum thickness of about 10 to 20 nm is necessary to form an electron accumulation layer for electron transport. Figure 2.7.8 shows the AFM gradient images of a 20-nm thick DFH-4T and a 20-nm thick DFHCO-4T film grown on top of poly-α-methylstyrene (PαMS) under optimized

growth conditions. The 3D needle growth is strongly suppressed. A few 3D features could still be observed for DFHCO-4T sample. These optimized growth conditions were used for sample fabrication.

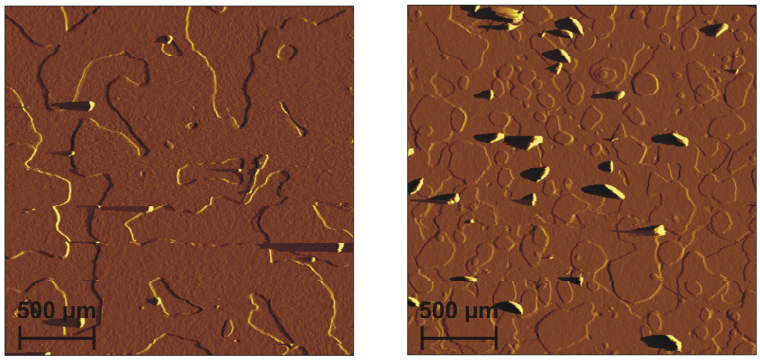

Figure 2.7.8. 2.5 µm x 2.5 µm AFM gradient image of (a) a 20-nm thick DFH-4T film deposited at 5 Å/s, while the substrate was at 60 °C, and (b) a 20-nm thick DFHCO-4T film deposited at 5 Å/s and a substrate temperature of 70°C.

Different organic layer stacks were then deposited on top of first order photonic feedback structures, which were etched into SiO2 with a pitch of 210 nm and a duty cycle of 50%. The depth of the trenches was about 50 nm (see WP3).

The following organic layer stacks were deposited:

A. PTAA (50nm) / Alq3:DCM2 (50nm) / Alq3 (100nm)
B. PTAA (50nm) / Alq3:DCM2 (50nm) / PTCDI (10nm) / Alq3 (90nm)
C. PTAA (50nm) / Alq3:DCM2 (50nm) / DFH-4T (20nm) / Alq3 (80nm)
D. PTAA (50nm) / Alq3:DCM2 (50nm) / DFHCO-4T (20nm) / Alq3 (80nm)

For all samples the total thickness of the organic layers is 200nm, which should resulting lasing around 640nm. Sample A is a reference sample. A lasing threshold of ~1200pJ/pulse has been measured before for this organic layer stack.

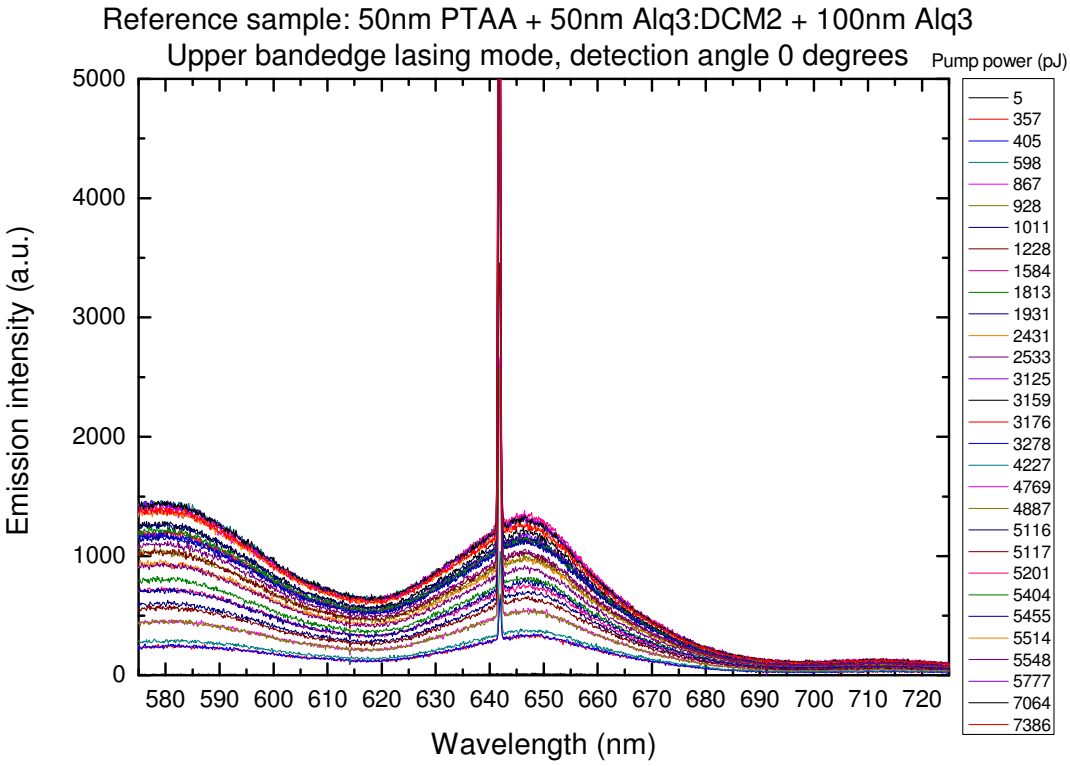

Figure 2.7.9. Emission from a lasing structure comprising 50 nm PTAA, 50 nm Alq3:DCM2 and 100nm Alq3. Above the threshold a lasing peak appears in the spectrum.

Figure 2.7.9 shows the emission spectra of the reference sample, measured at various pumping intensities. Compared to the former ones (WP4), however, a much lower lasing threshold is measured (~400 pJ vs ~1200 pJ). This could be explained by the fact that new gratings were used, which might be cleaner (less roughness / dirt) and therefore contain less scattering impurities which lead to additional losses. In addition, two other facts might indicate small differences between the new gratings and the ones used before. The lasing wavelengths are shifted to the red by a few nm and are now compatible with a total thickness of 250nm (neglecting the waviness). Before, the effective thickness was about 225nm, which is more like the average between valley (200nm organics) and ridge (50nm SiO2 ridge + 200nm organics). A slightly larger grating period from the new grating batch from AMO could induce this effect. Furthermore, the upper and the lower band lasing mode are now separated by only 5 nm (before: 7 nm) which might be an indication that the etch depth of the grating is slightly smaller. These observations prohibit direct comparison between the laser thresholds of the current samples and the ones obtained from older measurements. The thresholds of different samples fabricated on gratings of the same batch can of course be compared.

Table 2.7.1: Summary of the lasing thresholds of the different samples fabricated

	Measured average lasing threshold
Sample A (Reference sample)	400 pJ/pulse
Sample B (PTCDI-C13H27 ETL)	-
Sample C (DFH-4T ETL)	6188 pJ/pulse
Sample D (DFHCO-4T ETL)	6122 pJ/pulse

Table 2.7.1 summarizes the average lasing thresholds of the different samples fabricated. For sample B (comprising PTCDI-C13H27 as the electron-transporting material) no lasing could be observed. We attribute this to the substantial re-absorption of emitted photons by PTCDI (Figure 2.7.5). For sample C and D, however, an average lasing threshold of about 6000pJ/pulse was obtained, indicating that lasing can be achieved on material stacks including hole- and electron transporting layers which are of direct use in the hybrid devices structure based on a vertical organic heterojunction. However, the threshold of the DFH4T and the DFHCO4T samples is about one magnitude larger than the reference sample. This means that probably the layer morphology increases the losses, since both materials should be transparent at the lasing wavelength. In addition, the wavelengths are blue-shifted by about 10 nm compared to the reference sample (see Figure 2.7.10), which is indicative of a much thinner total layer thickness and/or a much lower refractive index than Alq3. A grating with a slightly larger period (~215 nm) would shift the lasing wavelength more to the spectral range with maximum gain, which might result in a lower lasing threshold.

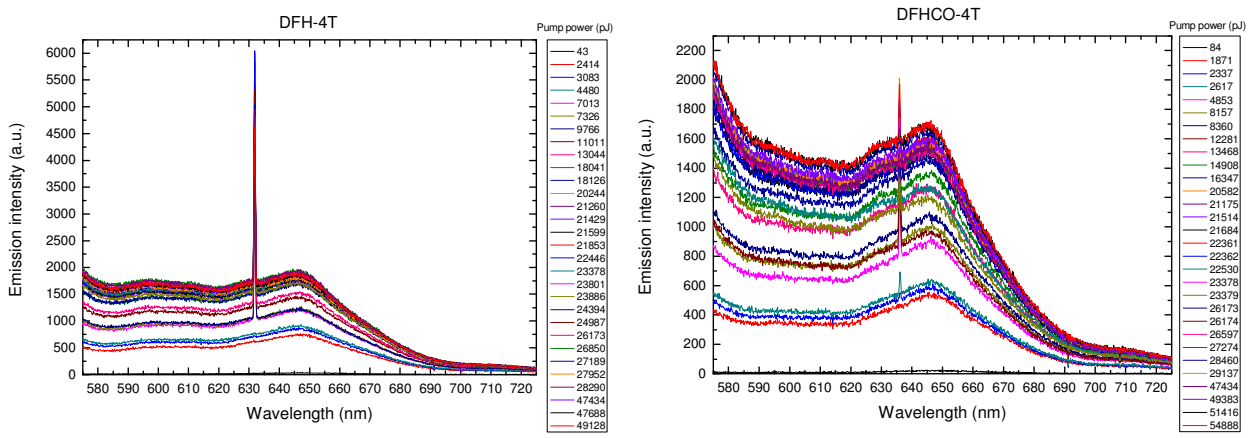

(a) **(b)**

Figure 2.7.10. Emission spectra of (a) sample C, and (b) sample D for various pumping intensities. Above threshold a lasing peak appears in the spectrum.

An important conclusion from these measurements is that we are able to achieve lasing on material stacks including hole- and electron transporting layers which are of direct use in the hybrid devices structure based on a vertical organic heterojunction. However upon inserting an electron-transporting layer the laser threshold is increased about one order of magnitude. Unfortunately, this threshold will increase further when an ITO bottom electrode and a much thinner gain region is used. An increase of a factor 3 may be expected when decreasing the gain layer from 50 nm to 20 nm (WP4). This means that, even without the presence of ITO, the lasing threshold will be ~ 20000 pJ/pulse, which is at the limit of sample degradation.

Enhanced Photonic Feedback Structures

In addition to what forseen in the workplan we studied possibilities to further enhance the photonic feedback structure for the laser. In order to achieve a high integration density the device footprint of the lasers should be as small as possible. However, for a vertically emitting laser, based on a second order planar feedback structure, the shrinking of the footprint increases the loss at the edge of the feedback structure. Therefore the lasing threshold was increased in order to make the realization of small devices impossible. IBM came up with a novel feedback design where a first order feedback structure encloses the second order structure and thereby prevents the loss at the edges of the structure. The mixed order photonic structure was realized in a 30 nm thin Ta_2O_5 layer by AMO. After spin coating MeLPPP as generic organic gain material on top, we were able to demonstrate a reduction of more than a factor of 40 in the footprint while improving the lasing threshold with optical pumping. This design is suitable for incorporation into the electrically pumped OLAS devices.

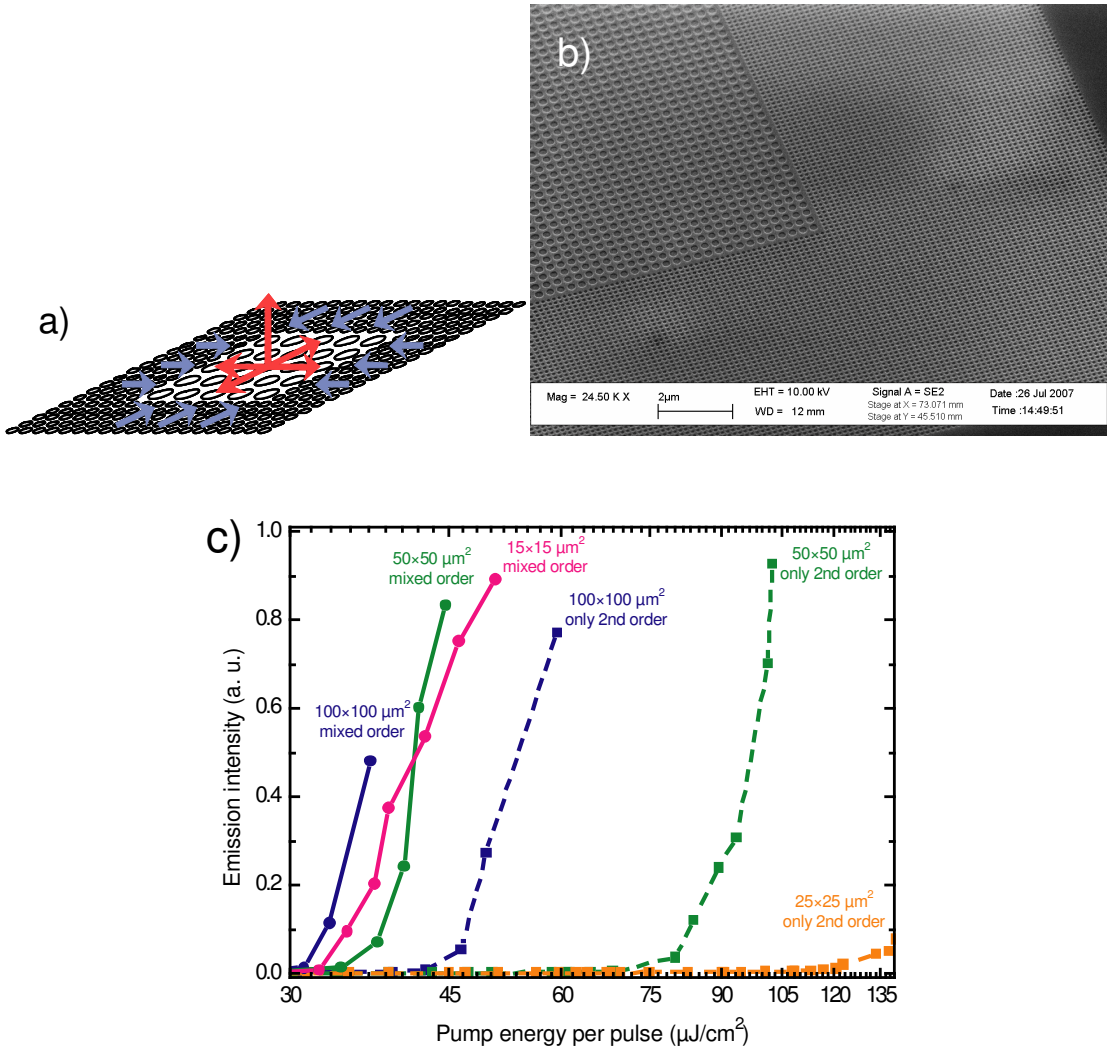

Figure 2.7.11. a) Concept of enclosing a vertically emitting 2nd order feedback structure with a 1st order "mirror". b) SEM image showing the corner of the device (without organic gain layer). c) The laser threshold is experimentally determined by the change in slope of the emitted intensity versus the pump energy. The mixed order feedback structure enables optically pumped lasing even in ultrasmall footprint devices.

Table 2.7.2: Deliverables of WP7

Del. no.	Deliverable name	Workpackage no.	Date due	Actual delivery date	Estimated indicative person-months *)	Used indicative person-months *)	Lead contractor
D19	Fabrication of device structure with integrated field-effect and photonic features	WP7	M18	M18	4	4	IBM
D21	Fabrication of organic heterojunction photonic field-effect devices	WP7	M21	M27	15	10	IBM

D23	Technical analysis of the losses and gain in the optically pumped laser in field-effect devices	WP7	M24	M30	6	0	IBM
D25	Technical analysis of the losses and gain in the optically pumped laser in field-effect devices under electrical bias conditions	WP7	M27	-	6	0	IBM

Table 2.7.3: Milestones of WP7

Milestone no.	Milestone name	Workpackage no.	Date due	Actual delivery date	Lead contractor
M8	Fabricate organic heterojunctions field-effect devices with integrated photonic feedback structure	WP7	M21	M27	IBM
M9	Achieve optically pumped laser in organic heterojunctions field-effect devices under electrical bias	WP7	M27	-	IBM

WP8. Electrically pumped laser (WP leader: IMEC)

This workpackage focuses on the realization of an organic electrically pumped laser and the photonic and electronic characterization of heterojunction electrically pumped lasers.

A major challenge in building an electrically pumped organic laser is the reduction of the absorption losses at the electrodes. Within the OLAS project three different device architectures were developed to reduce these losses: an organic light-emitting field-effect transistor based on a planar heterojunction, a hybrid field-effect/diode structure and a multi-layer field-effect structure. In

all three device geometries the metal electrodes are positioned one to several micrometers away from the optical active region, reducing the optical absorption losses. Two other major obstacles with respect to the realization of an electrically pumped organic laser are the presence of charge carriers and triplet excitons, which may absorb the emitted photons and/or may deplete the exciton population. Both issues were addressed during the project.

Unfortunately, due to the complexity of the task and for technical issues in the fabrication facilities, we were unable to demonstrate electrically pumped lasing within the project timeframe. The obtained results however, indicate further progress towards its realization. Lasing under optical excitation has been observed for organic layer stacks comprising electron and hole transporting layer which are of direct use in electrically driven devices (see WP7). We demonstrated that apart form minimizing the optical absorption losses and achieving high current densities, the hybrid field-effect/diode structure may also be able to reduce the triplet population in the device. In addition, we showed that carrier absorption is not a limiting factor in our devices at the investigated excitation densities.

Pulsed excitation of the hybrid field-effect/diode structure

Apart from the proximity of the electrical contacts and the polaron concentration, also the presence of triplets in the active organic semiconductor is an important issue with respect to the realization of an electrically pumped organic laser. Triplet-state losses such as singlet-triplet quenching or triplet-triplet absorption, might indeed limit the performance of future organic laser devices. One of the approaches suggested in literature to address this difficulty is to operate the device under pulsed excitation. Pulsed operation has several advantages: it avoids heat and stress in the device, it allows higher current densities compared to continuous wave operation, and it makes it possible to separate singlet excitons from triplet excitons and polarons in the time domain. This time separation would allow a tremendous reduction of polaron and triplet absorption in an electrically driven organic light-emitting device. Indeed, one of the main problems associated with electrically pumped organic semiconductors lasers is the inevitable population and accumulation of triplet excitations, which result in excessive triplet-state losses preventing lasing. If conventional spin statistics applies, the recombination of injected charge carriers leads to the creation of a majority (75%) of non-emissive triplet excitations in the active organic semiconductor layer. Due to their long lifetime, these triplet excitations can act as metastable species, which generally have fairly high absorptions to the upper triplet state (triplet-triplet absorption) at the expected fluorescent lasing wavelength. By applying

pulses which have a pulse duration longer than the singlet lifetime (typically ~ 1 ns) and shorter than the lifetime of triplet excitons (milliseconds to seconds for fluorescent materials), and assuming the pulse repetition rate is low, the accumulation of triplet excitons could be reduced. In this way triplet state losses such as singlet-triplet annihilation and triplet-triplet absorption, which are major loss mechanisms with respect to the high photon density required for an electrically pumped organic laser, might be suppressed.

We investigated the pulsed excitation behavior of the hybrid field-effect/diode structure comprising PTAA as the hole-transporting layer, Alq_3:DCM_2 as the light-emitting layer and PTCDI-$C_{13}H_{27}$ as the electron-transporting layer and compared their performance to conventional OLEDs comprising the same organic layers. If the transit time of carriers through the transport layers contributes to the determination of the minimum pulse duration applicable to an OLED, we expect that devices employing an enhanced field-effect mobility may allow shorter pulse durations compared to standard OLEDs.

The devices were characterized in an inert N_2 atmosphere immediately after evaporation of the metallic top-contact. An Agilent 8114A pulse generator (rise and fall time = 8 ns) was used to apply rectangular pulses to our devices. The duty cycle was 10%, and the pulse length was varied between 100 ns and 100 µs. All cables were 50 Ω terminated to avoid reflections. A calibrated integrated sphere (SphereOptics Hoffman GmbH) coupled to an Agilent 4156C parameter analyzer was used for light intensity measurements.

Figure 2.8.1 shows the measured light output as a function of the pulse width for a conventional OLED and a hybrid field-effect/diode structure biased at 7 V and 20 V, respectively. Both devices were fabricated during the same evaporation runs and comprise the same organic layer stack. From Figure 2.8.1 the minimum pulse width that can be applied without affecting the light output can be determined. Since in the hybrid field-effect/diode structure the electrons have an enhanced field-effect mobility, it was assumed that in these devices shorter pulses could be applied compared to standard OLEDs. However, Figure 2.8.1 clearly shows that there is no distinct difference between the minimum allowable pulse width of both device architectures. Both devices allow pulses up to ~10 µs without significant reduction of the light intensity. The shape of the curves, however, differs strongly. The hybrid field-effect/diode structure shows a significantly weaker dependence on the pulse duration compared to the conventional OLED.

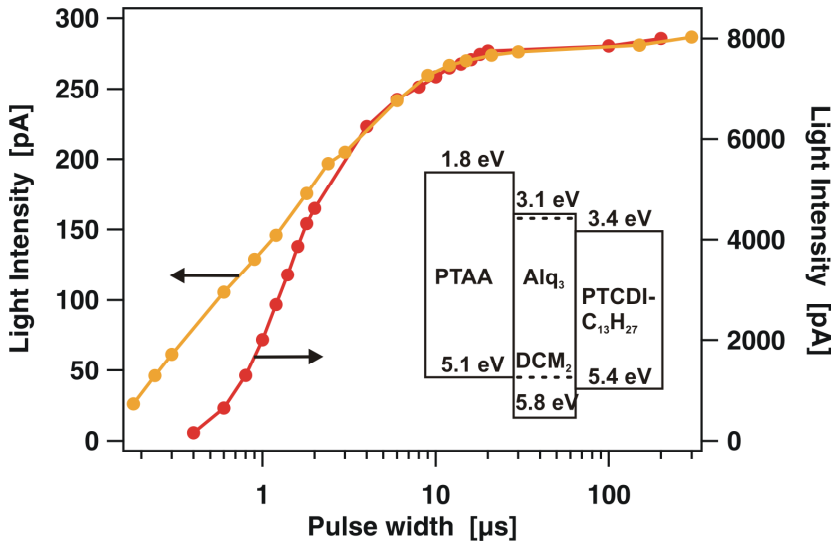

Figure 2.8.1 The measured light intensity as a function of the pulse width for a conventional OLED (red curve) and a hybrid field-effect/diode structure (orange curve) biased at 7 V and 20 V respectively. Inset: energy level diagram of the organic layer stack. The dotted lines indicate the highest occupied molecular orbital (HOMO) and the lowest unoccupied molecular orbital (LUMO) positions of DCM_2.

Different effects may influence the pulse width dependence of light-emitting devices. A first possible reason for the decrease of the light output at short pulse widths could be the finite transit time of carriers through transport layers. One of the parameters controlling this process is the charge carrier mobility. If the mobility of one of the charge carriers is too low, the steady state exciton concentration cannot be reached within the pulse duration, resulting in a decrease of the measured light intensity. To verify whether the charge transport through the electron accumulation layer in PTCDI-$C_{13}H_{27}$ is a limiting factor, we fabricated hybrid field-effect/diode structures having various distances between the metallic contact and the insulator edge, and thus different electron transit times. The result is shown in Figure 2.8.2(a): all devices show the same pulse width dependence. Subsequently, we verified whether charge transport in the hole-transporting or light-emitting layer could be limiting, by varying the thicknesses of the PTAA and the Alq_3:DCM_2 layer. Figure 2.8.2(b) shows the dependence of the light intensity on the pulse width for OLEDs comprising 15 nm or 50 nm PTAA, whereas in Figure 2.8.2(c) the thickness of the active light-emitting layer is changed. The dependence of the light output on the applied pulse width is invariant with the thickness of the layers and hence not limited by the transit times of carriers through any of the layers in our device structure.

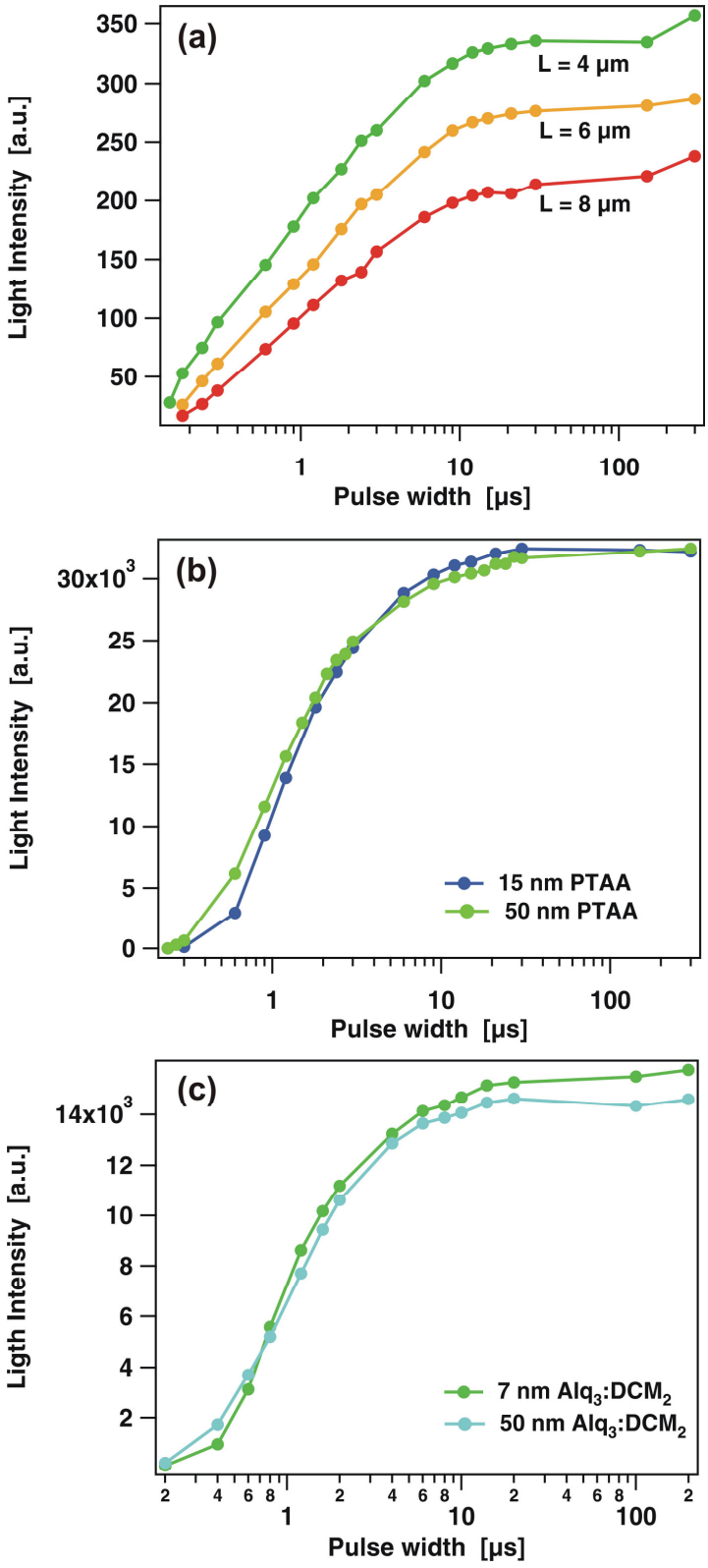

Figure 2.8.2. Dependence of the light intensity on the pulse width for (a) hybrid field-effect/diode structures having, respectively, a distance of 4 µm, 6 µm and 8 µm between the metallic contact and the insulator edge, (b) conventional OLEDs comprising 15 nm or 50 nm PTAA, and (c) conventional OLEDs having an active layer of 7 nm or 50 nm thick. The hybrid field-effect/diode structures were biased at 20V, whereas 7V was applied to the conventional OLEDs.

In multi-layer OLEDs, however, not only charge transport, but also charge accumulation at the hetero-interfaces between the different semiconductors should be taken into account. The energy level diagram under flat band conditions, shown as inset in Figure 2.8.1, clearly indicates the presence of energy level offsets at the organic/organic interfaces. Consequently, injected electrons and holes, transported through the PTCDI-$C_{13}H_{27}$ and PTAA layer, respectively, will accumulate at these interfaces before injection into the active light-emitting layer. Depending on the applied electric field, space charge will be built-up faster and the charges will more easily overcome the present energy barriers. Figure 2.8.3 shows the dependence of the light intensity on the pulse width for an OLED biased at different voltages. It can be clearly seen that the minimum allowable pulse width decreases from 10 µs to about 1 µs when applying higher voltages. This points out that one of the organic/organic interfaces indeed limits the behavior of the device under pulsed excitation. Note that the minimum pulse width that can be obtained without significant reduction of the light intensity is much shorter than the typical triplet lifetime of fluorescent materials, indicating that pulsed excitation might be useful to reduce the accumulation of triplets in the device.

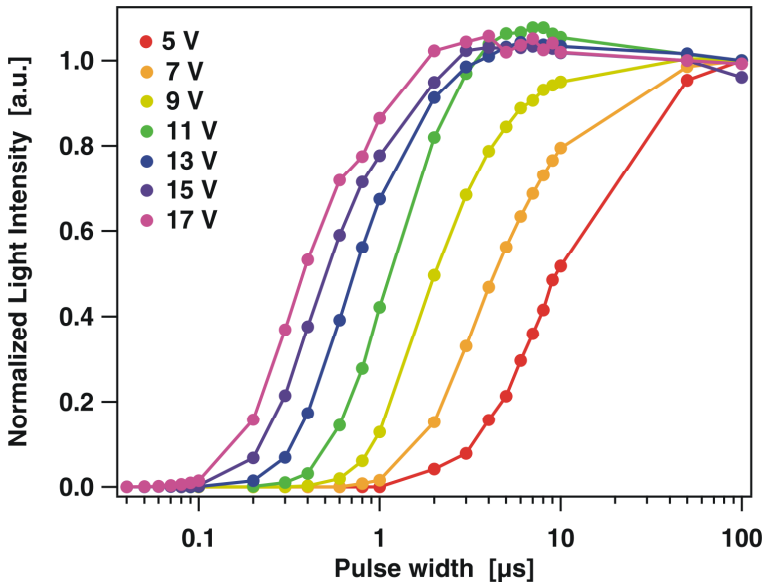

Figure 2.8.3. Pulse width dependence of an OLED comprising PTAA/Alq_3:DCM_2/PTCDI-$C_{13}H_{27}$ as the organic layer stack biased at different voltages.

To verify which interface is the limiting factor two additional OLEDs were fabricated: ITO/PTAA/Alq_3:DCM_2/LiF/Al and ITO/PTAA/Alq_3:DCM_2/Alq_3/LiF/Al. In both devices the energy barrier between the electron-transporting layer and the active light-emitting layer is eliminated. The total thickness of the organic layers was kept constant in order to apply the same electric field over the devices. Consequently, the first device comprises 70 nm of Alq_3:DCM_2,

whereas the second OLED has a 20-nm thick Alq_3:DCM_2 layer and 50 nm of undoped Alq_3. Figure 2.8.4 compares the light output of these two OLEDs with the one of Figure 2.8.3 as a function of the pulse width when a bias of 9 V is applied. A clear difference in pulsed excitation behavior is observed. The minimum pulse width that can be applied without affecting the light intensity shifts to shorter values when the energy offset at the interface between the PTCDI-$C_{13}H_{27}$ and the Alq_3:DCM_2 layer is eliminated. This indicates that the PTCDI-$C_{13}H_{27}$/Alq_3:DCM_2 interface has a limiting effect on the pulsed excitation properties of our light-emitting devices. Since this interface is present in the conventional OLED as well as in the OLED with a remote cathode, it is obvious that the behavior under pulsed excitation of both devices is similar (Figure 2.8.1). The fact that a dependence on the pulse duration is weaker in the case of an OLED with a remote cathode can be understood by a spread in potential drop. Indeed, the light-emission zone of an OLED with remote cathode is approximately 2 µm wide. Over this area the potential drop over the PTCDI-$C_{13}H_{27}$/Alq_3 interface decreases with the distance from the insulator edge (Fig. 2.8.1(b)). Therefore, an OLED with remote cathode is to be interpreted as the sum of sections of standard OLED devices each with a different voltage over the PTCDI-$C_{13}H_{27}$/Alq_3 hetero-interface. This indeed leads to an overall weaker dependence of the light intensity on the pulse duration, as observed in Figure 2.8.1.

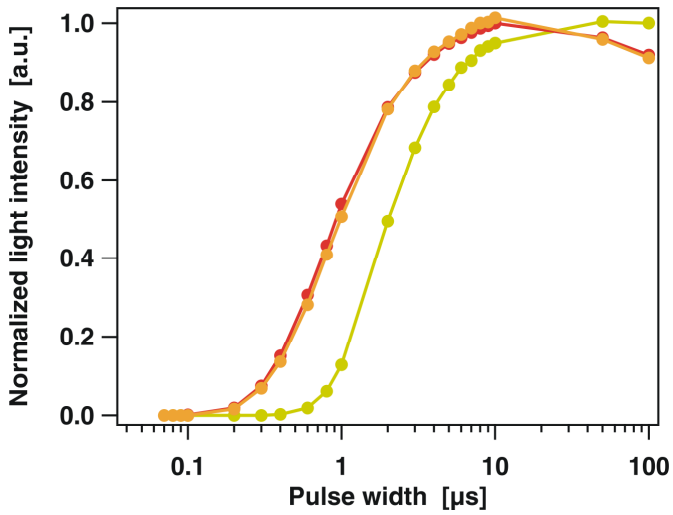

Figure 2.8.4. Light intensity as a function of the pulse width of OLEDs comprising (a) PTAA/Alq_3:DCM_2/PTCDI-$C_{13}H_{27}$ (yellow curve), (b) PTAA/Alq_3:DCM_2 (orange curve), and (c) PTAA/Alq_3:DCM_2/Alq_3 (red curve) as the organic layer stack. A bias of 9 V was applied to the devices.

WP9. Technology assessment and exploitation (WP leader: IBM)

The objective of this workpackage is to assess the newly developed technologies with respect to standard ones and set the bases for the exploitation. This is targeted to guarantee an effective take-up of the developed technological solutions in real applications.

The enduring thrust for higher bandwith data transmission systems and networks ultimately calls for innovative and cost-effective devices capable to satisfy the increasing demand in the area of information transfer. The bottleneck in the current technology is the conversion of the electrically generated data into optical data and vice versa. Up to now optical transmission of data has only been used for long distance transfer. The increasing bandwidth requirements will demand for optical communication on shorter distances with the ultimate need to integrate the optics directly on the chip, in the future. However, the present laser technology based on inorganic semiconductors is not compatible with current CMOS technology and therefore cannot be integrated into the chip. Electrically pumped organic lasers are expected to provide a cost-effective solution. Furthermore, these lasers can easily be integrated with polymer waveguide technology which will be used in optical interconnects in the near future as can be inferred from the figure below.

	Internet, Wide Area Network	Local Area Network	Rack-to-Rack	Card-to-Card	On-Card	On- MCM	On-Chip
					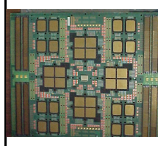	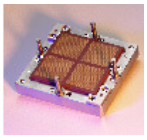	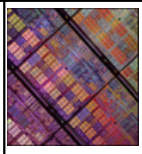
Distance	multi-km	10 - 2000 m	30+ m	1 m	0.1 - 0.3 m	5 - 100 mm	0.1 - 10 mm
Number of lines	1	1 – 10	~100	~100-1000	~1000	~10'000	~100'000
Use of optics	Since the 80s and the early 90s	Since the late 90s	Now	2010+	2010-2015	Probably after 2015	

Exploitable knowledge generated from the project concerned:

- a newly developed sputtering technology of inorganic dielectrics compatible with organics. It can not only be used for dielectric mirrors, but also as an optical coating on top of an organic solar cell as well as an organic light emitting diode in order to optimise the in- and out-coupling of light, respectively.
- An enhanced surface emitting photonic crystal device.
- An enhanced feedback structure consisting of a mixed-order photonic crystal membrane.
- A hybrid organic/semiconductor photonic feedback structure.
- The fabrication and etching processes of amorphous Ta_2O_5 layers.

A more detailed description of each exploitable knowledge item is reported in Section 2. Dissemination and Use.

Table 2.9.1: Deliverables List

Del. no.	Deliverable name	Workpackage no.	Date due	Actual delivery date	Estimated indicative person-months *)	Used indicative person-months *)	Lead contractor
D30	Comparative analysis of the new and existing lasing technologies for exploitation	9	M36	M36	1	1	IBM
D31	Analysis and issuance of Patents	9	M36	M36	0,5	1	IBM
D32	Technology implementation Plan	9	M36	M36	0	0	IBM

Table 2.9.2: Milestones List

Milestone no.	Milestone name	Workpackage no.	Date due	Actual delivery date	Lead contractor
M12	Assessment of electrically pumped organic laser technology	9	M36	-	IBM

Section 3 – Consortium management

The consortium adopted a highly interactive and cooperative management model in order to implement the complex scientific and technological workplan of the OLAS project. The effective integration of the strong multidisciplinary consortium relied on a distribution of tasks to partners according to their specific know how, while the overall work was implemented through a constant and extensive cooperative interaction.

The consortium defined the specific communication tools to be used for the project at the kick-off meeting held in Bologna on February 3, 2006. The tools were a Consortium database, monthly teleconferences, general meetings, bilateral interactions and implementation of joint experiments. These tools were implemented during the first year and then continuously used throughout the duration of the project.

A Consortium Database was regularly used to share all results of the project activity as soon as they become available and to circulate discussion items within the consortium. New results related to the topic of the project are posted in the database, irrespective if they are generated inside or outside the consortium. All partners are sent an alert e-mail concerning the new posted information. The access to the OLAS Database is subject to restrictions as its content is confidential.
The database was built with the constant contribution of all partners and now thoroughly represents the consortium activity and achievements. All the official documents sent to the commission and to the reviewers can be found by partners at any time. The database can be accessed directly or via the public project website entering the restricted area.

Full Meetings have been held each six months. The project coordinator presents the project status by reviewing the project results posted in the database and sets the basis for the discussion. Particular emphasis is given to the discussion of the open critical issues and to the analysis of the possible solutions. The meetings are also a preferential occasion to reinforce direct personal relationships among people directly involved in the project research. The meetings are organized at each partner premises so to build a diffuse awareness of the experimental facilities used for the project. An updated plan for the activity to be performed during the next six months is established at the end of each Full Meeting.
The following Full Meetings were held during the project:

- Bologna on February 3, 2006
- Aachen on September 12, 2006
- Brussels on March 12, 2007
- Zurich on June 5-6, 2007
- Strasbourg on April 13, 2008
- Brussels on March 16, 2009

Monthly Teleconferences have the double scope of providing timely feedback to directly inter-linked activities and of keeping a diffuse awareness of the project advancements and critical issues. Data to be discussed in a teleconference are posted in the database well in advance in order to give to all partners comfort time for their evaluation.
The project coordinator sets an agenda for the teleconference, which is based on the new results to be discussed, and on the specific tasks to be performed in the coming period. During the discussion each partner makes reference to the data previously shared through the database. Immediately after

the teleconference the project coordinator prepares and circulates via e-mail the Meeting Action Plan (MAP) in which are specified the *Action to be Taken*, the *Person responsible* for it and the *deadline*. The actual implementation of the MAP, and the eventual problems encountered, is the first item to be discussed at the next teleconference.

During the project the following Teleconferences were held:

- 04 April 2006;
- 31 May 2006;
- 04 July 2006;
- 26 October 2006;
- 06 December 2006.
- 19 January 2007;
- 27 February 2007;
- 08 May 2007;
- 19 June 2007;
- 11 September 2007;
- 05 December 2007,
- 22 January 2008;
- 27 March 2008;
- 30 June 2008;
- 02 September 2008
- 12 December 2008

Specific visits to partners labs were organized to implement the work decided in the general assemblies and during the Teleconferences:

- January 25, 2007: visit of S. Schols (IMEC) at RWTH (T. Plötzing, M. Foerst) for delivery of samples and joint measurements.
- July 25, 2007: visit of T. Plötzing (RWTH) at IMEC (S. Schols) for collecting samples.
- August 22, 2007: visit of T. Wahlbrink (AMO) at IMEC (S. Schols) to discuss design of the vertical heterojunction light-emitting device with incorporated feedback structure.
- October 04, 2007: Visit of Tobias Plötzing (RWTH) at IMEC for joint sample preparation and direct sample delivery.
- April 01, 2008: visit of T. Wahlbrink (AMO) at IMEC (S. Schols) to discuss issues in sample preparation procedures.

Partner labs have hosted the visits of prominent international scientists in the field of organic

optoelectronic and photonics. We mention that Prof. Chihaya Adachi from the University of Kyushu in Japan (one of the most active labs in the field of organic lasing) visited IMEC and IBM labs in January 2007 and CNR labs in June 2007 to share views and latest results related to the progress towards the electrically pumped organic laser. Rainer Mahrt (IBM) and Michele Muccini (CNR) visited Prof. Chihaya Adachi's lab during the course of the last year of the project.

A project timetable showing a frontlined barchart is reported in Table 3.1.

PROJECT BARCHART and STATUS

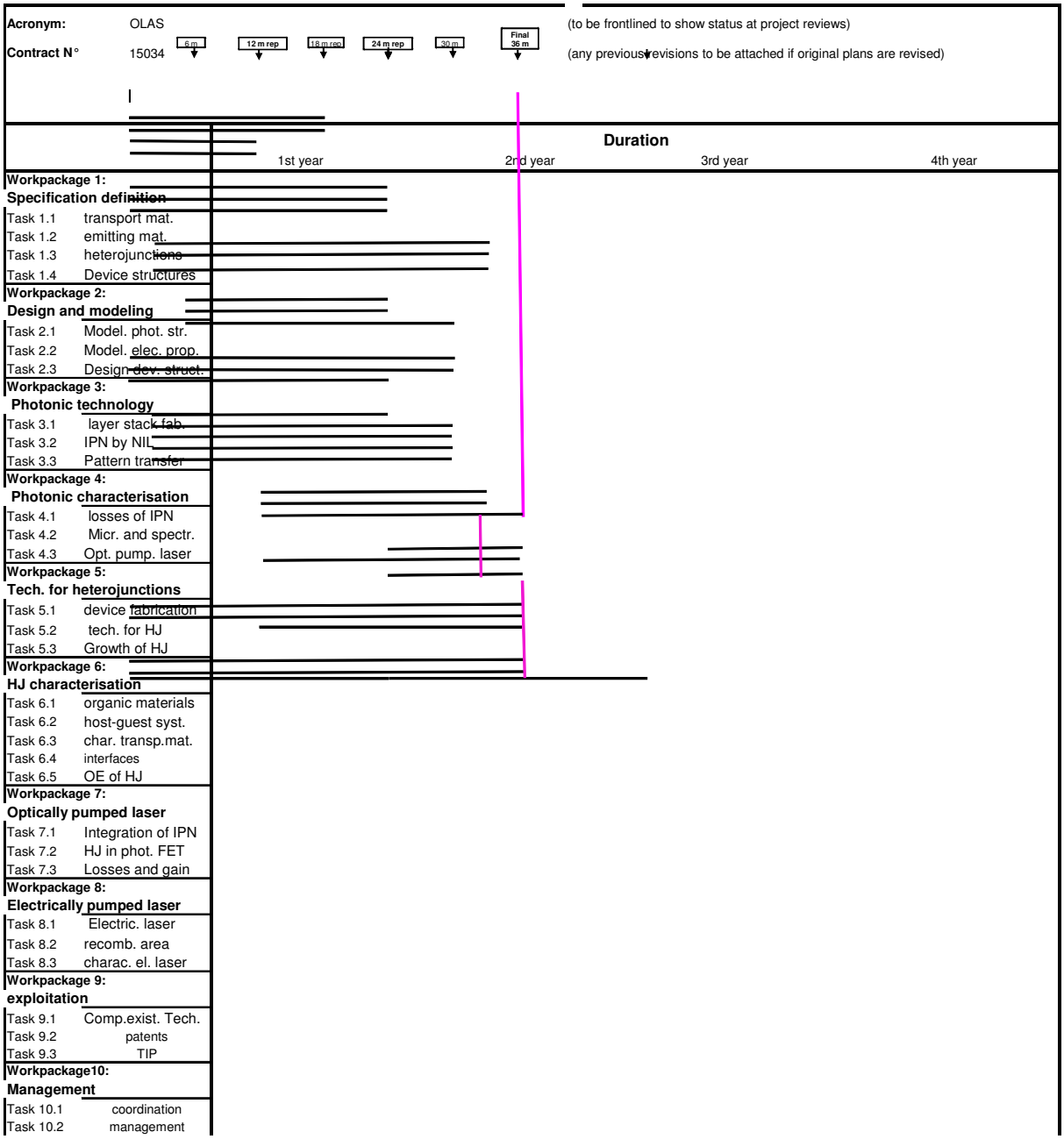

Table 3.1: Workpackages - Plan and Status Barchart

The fabrication of the integrated photonic field-effect devices was not as fast as anticipated due to technological complexity and some technical problems encountered during the multi-step device fabrication process. Despite the fact that within the OLAS project two approaches were developed in order to reduce the losses at the electrodes - a hybrid field-effect/diode structure and a multi-layer field-effect structure- we were unable to demonstrate electrically pumped lasing in these devices within the project timeframe. For this reason Deliverable 28, 29 and 30, which were related to the electrically pumped laser, were not submitted.

Section 2. Dissemination and use

a. Exploitable knowledge and its use

The economic and societal impact of photonics is widespread. Photonic technologies contribute significantly to the sectors of information technology, health science, energy saving, safety and security to name only a few. Therefore, photonics became a booster for technological innovation and is one of the key-technologies of the 21st century. Keeping this in mind the OLAS consortium considers the commercial use and exploitation of the results emanating from the project as of utmost importance.

A list of exploitable results is given in the overview table below.

Overview table

Exploitable Knowledge (description)	**Exploitable product(s) or measure(s)**	**Sector(s)** of application	Timetable for commercial use	Patents or other IPR protection	**Owner** & Other Partner(s) involved
1.Enhanced surface emitting photonic crystal device	Integrated photonics	IT Lighting Sensing Optical communication	>2012	Patent filed 2007	**IBM**
2. Enhanced feedback structure consisting of a mixed-order photonic crystal membrane	Integrated photonics	IT Sensing Optical communication	>2012	Disclosure submitted Patent to be filed 2009	**IBM**
3. Hybrid organic/semiconductor photonic feedback structure	Integrated (silicon-) photonics	IT Optical communication	>2012	Patent filed 2008	**IBM**

4. Fabrication and etching process of amorphous Ta_2O_5 layers		IT Coating Optical communication	2009		**AMO**

Summary and description of inventions:

1. In this invention a central two-dimensional surface-emitting distributed feedback structure is surrounded by a first-order distributed Bragg reflector to reduce the radiation losses at the edge of the device. In contrast to conventional devices which have either a small footprint (DFB) or low lasing threshold (DBR) this device has both of these features combined in one. This invention enables to lower the lasing threshold and/or reduce the footprint dramatically. By tuning the size of the resonator and the mirrors independently one can choose between the benefits of lower threshold and smaller footprint in a continuous way. Perfectly balanced devices for the desired application are feasible. A further advantage is that the out-coupled light is a diffraction-limited beam perpendicular to the surface of the device. The disclosed device consists of a two-dimensional distributed photonic feedback region (DFB) which is designed in second order. In contrast to a linear grating the out-coupled light is strongly directed perpendicular to the device. To circumvent the undesirable edge losses the laser resonator is enclosed with a first-order distributed Bragg reflector. The geometry of the mirror gratings (height, duty cycle, and period) is chosen that the lasing wavelength resulting from the design of the second-order structure is centered within the band-gap of the first order structure. Light of this wavelength is forbidden to propagate in the mirror (the electric-field profile decays exponentially) and is reflected back into the resonator. The central aspect of the present invention is the combination of two-dimensional distributed feedback structures with distributed Bragg reflectors to lower the footprint and lasing threshold. In addition to organic lasers, also conventional semiconductor lasers benefit from this new photonic feedback design.

2. The disclosed device consists of a two-dimensional distributed photonic feedback region (DFB) which is designed in second order. In contrast to the device described in #1, both parts, the two-dimensional distributed photonic feedback structure and the first order distributed Bragg reflector are located within a photonic crystal layer and sandwiched between or centered in the optical gain material enabling better optical confinement and enhanced

efficiency of the photonic feedback structure. This results in an even lower threshold and/or smaller device footprint.

3. This novel concept comprises absorptive electrodes built from doped semiconductor material which serve the need for charge carrier injection as well as implementing a photonic cavity. This hybrid organic/inorganic concept readily allows the integration of organic lasers with silicon-on-insulator technology important for future applications. The invention is implemented by two linear or curved arrays of high-refractive-index semiconductor blocks or cylinders on a transparent substrate which is coated with the organic layers. The working principle requires proper engineering of phase shifts and total internal reflection inside the high-index arrays in order to realize a laser resonator with sufficiently high Q-factor even with absorptive building blocks such as doped Si.

4. In DFB structures the efficiency of the optical feedback structure is determined by the refractive index contrast between the material of the photonic feedback structure and the surrounding material. Between organic gain materials (n=1.65-1.75) and SiO_2 DFB structures (n=1.46) the difference in refractive index is only 0.2-0.3. Furthermore, SiO_2 degrades the guiding and confinement of the optical mode because of its rather low refractive index. Using a high-index material and increasing the index contrast improves the optical feedback and enables lower lasing thresholds and/or smaller device footprints. In OLAS the high-index material Ta_2O_5 (n=2.15) has been integrated into innovative resonator concepts for highly efficient laser cavities. Introducing a thin high-index layer with the proper feedback structure pulls the optical mode towards the high-index layer resulting in an enhanced coupling of the lasing mode. This leads to a reduced threshold and/or smaller device footprints. A complete fabrication process for Ta_2O_5 based laser cavities has been developed and optimized including deposition, high resolution electron beam lithography and reactive ion etching. This fabrication sequence is offered by AMO as service to interested parties.

- The devices described in #1-3 has been fabricated and tested. A possible integration into all optical networks or in optical interconnect technology could be foreseen due to their attractive packaging possibilities and their CMOS compatibility.
- For the devices described in #1&3 patent applications have been filed. For the device described in #2 the patent application is planned for Q1/2009 (see deliverable D31).

- The devices described in #1 together with the process described in #4 have gained tremendous public interest which is reflected in various media coverage by e.g., SPIE newsroom, Elektronik Report AT, Swiss Engineering STZ, Laser Focus World, physorg.com

b. Dissemination of knowledge

A public web page of the project was created at the address www.olasproject.eu. The main information about the project, the public results, the press releases, the dissemination activities of all partners are reported in an appealing graphical environment. Each partner's website is linked and a restricted access area allows direct log-in of authorized people to the Consortium database.

IMEC and CNR have jointly organized two international conference on the topics of the project:

- SPIE - Photonics Europe; Workshop on *"Organic Optoelectronics and Photonics"* (Strasbourg, 2-7 April 2006).
- SPIE - Photonics Europe; Workshop on *"Organic Optoelectronics and Photonics"* (Strasbourg, 7-10 April 2008).

CNR organised the *"14th International Workshop on Inorganic and Organic Electroluminescence & 2008 International Conference on the Science and Technology of Emissive Display and Lighting",* held in Rome, 9-12 September 2008.

OLAS members gave talks at the following International Conferences:

- *SPIE Photonics Europe 2006, 3-7 April 2006 Strasbourg, France [F.Dinelli,* CNR]
- *SPIE Photonics Europe 2006, 3-7 April 2006 Strasbourg, France [*S. Verlaak, IMEC]
- *SPIE Photonics Europe 2006, 3-7 April 2006 Strasbourg, France [*E. DaComo, CNR]
- *SPIE Optics and Photonics West 2006, 13-17 August 2006 San Diego, California, US [S. Schols, IMEC]*
- *SPIE Optics and Photonics West 2006, 13-17 August 2006 San Diego, California, US [M. Muccini, CNR, INVITED]*
- International Workshop "Organic Light-Emitting Device" (OLEDW 2007), Hong Kong, 22-23 January 2007. *[M. Muccini, CNR, INVITED]*
- *7th International Conference on Optical Probes of π-Conjugated Polymers and Functional Self Assemblies, 11.-15.06.2007, Turku, Finland [T. Stoeferle, IBM]*

- *7th International Conference on Optical Probes of π-Conjugated Polymers and Functional Self Assemblies, 11.-15.06.2007, Turku, Finland [M. Muccini, CNR]*
- *Advanced Polymer materials for photonics and electronics, 15-19.07.2007, Prague, Czech Republic [R.F. Mahrt, IBM, INVITED]*
- *SPIE Optics + Photonics, 26-30.08.2007, San Diego, USA [R.F. Mahrt, IBM, INVITED]*
- *SPIE Optics + Photonics, 26-30.08.2007, San Diego, USA [M. Muccini, CNR, INVITED]*
- European Conference on Molecular Electronics (ECME), September 5-8 2007, Metz, France.*[S. Schols, IMEC]*
- *33rd International Conference on Micro- and Nano-Engineering* (MNE07) 23-26 September 2007, Copenhagen, Denmark [T. Wahlbrink, AMO]
- *International symposium on ultrafast- and nano-optics, 29-31.10.2007, Beijing, PR China [R.F. Mahrt, IBM, PLENARY TALK]*
- *International Symposium on Optics & Photonics 2008*, SPIEs Annual Meeting, conference on "Organic Light-Emitting Materials and Devices XII". Talk: *"OLET Technology for solid state lighting applications"* 10-14 August 2008, San Diego, California (USA). [M Muccini, CNR, INVITED]
- *International Symposium on Organic Transistors and Functional Interfaces (OFET2008)*, talk: "*Organic heterojunctions as functional active layers for light-emitting field-effect transistors",* 19-23 August 2008, Sendai (Japan). [M. Muccini, CNR, INVITED]
- *EOS Annual Meeting 2008*, talk: *"Multilayer structures as active layers for light emitting field-effect transistors"*. 29 september – 2 october, Paris (France). [M. Muccini, CNR, INVITED]
- University of Fukuoka, Center for Future Chemistry, "*Organic heterojunctions as functional active layers for light-emitting field-effect transistors"*17 *August* 2008 Fukuoka (Japan). [M. Muccini, CNR. INVITED]

- *SPIE Europe*, Strasbourg, April 7-10, 2008 [R. Mahrt, IBM, INVITED]

- Kyushu University, Center for Future Chemistry, talk "*Photonic bandgap structures with organic materials for lasing and switching applications"* 30 june 2008 Fukuoka (Japan) [R. Mahrt, IBM, INVITED]

- Kyoto University, Graduate School of Engineering, Department of Electronic Science and Engineering, Quantum Optoelectronics Laboratory, talk: *Photonic bandgap structures with*

organic materials for lasing and switching applications, 1 July 2008, Kyoto (Japan) [R. Mahrt, IBM, INVITED]

- *European Optical Society Annual Meeting*, talk:*Organic Lasers with Mixed-Order Photonic Feedback Structures,* 29 September – 2 October 2008, Paris (France) [R. Mahrt, IBM INVITED]

- *Institut optique*, talk: *Lasing and switching in photonic bandgap structures with organic Materials*, *2 October 2008,* Paris (France),[R. Mahrt, IBM, INVITED]

- *SPIE Photonics Europe 2008*, Conference on organic opto-electronics and photonics III, talk: "*Performance oforganic light-emitting diodes with remote metallic contact using high mobility electron-transport layers*" 6-10 April 2008, Strasbourg (France) [S.Schols IMEC, C. McClatchey, J. Genoe, P. Heremans IMEC and A. Facchetti]

- *Quantum Systems and Technologies (QSIT)*, talk:"*Photonic Nanostructures for Lasing and Switching Applications*", 23-25 January 2008, Arosa (CH) [T. Stoeferle, IBM]
- *Cavendish Laboratory Seminar*, talk: *"Photonic Nanostructures and Materials for Lasing and Switching Applications"*, 12 May 2008, Cambridge (UK) [T. Stoeferle, IBM, INVITED]

The following papers were published in International Scientific Journals:

1. M. Muccini
   A bright future for organic field-effect transistors
   NATURE MATERIALS **5** (2006) 605

2. F. Dinelli, R. Capelli, M.A. Loi, M. Murgia, A. Facchetti, T. Marks and M. Muccini
   High-mobility ambipolar transport in organic light-emitting transistors
   ADVANCED MATERIALS 18 (2006) 1416

3. S. De Vusser, S. Schols, S. Steudel, S. Verlaak, J. Genoe, W. D. Oosterbaan,L. Lutsen, D. Vanderzande and P. Hereman,
   A light-emitting organic field-effect transistor using an organic heterostructure within the transistor channel
   APPLIED PHYSICS LETTERS, 89, (2006), pp223504

4. R. Capelli1, F. Dinelli, M.A. Loi, M. Murgia, R. Zamboni and M. Muccini
   Ambipolar organic light-emitting transistors employing heterojunctions of n-type and p-type materials as the active layer
   JOURNAL OF PHYSICS: CONDENSED MATTER 18 (2006) S2127

5. S. De Vusser, S. Steudel, S. Schols, S. Verlaak, J. Genoe, W. D. Oosterbaan,L. Lutsen, D. Vanderzande and P. Hereman
Light-emitting organic field-effect transistor using an organic heterostructure inside the transistor channel
SPIE Proceedings Paper 6192-16 pp. 71-80 SPIE Photonics Europe 2006

6. R Capelli, F Dinelli, M A Loi, M Murgia, and M Muccini
Ambipolar light-emitting field-effect transistors based on molecular thin films
SPIE Proceedings, Paper 6333-29 SPIE Optics and Photonics West 2006

7. S. Schols, S. Verlaak, J. Genoe and P. Heremans
A novel organic light-emitting device for use in electrically pumped laser
SPIE Proceedings, Paper 6333-30 SPIE Optics and Photonics West 2006

8. Kristian Baumann, Thilo Stöferle, Nikolaj Moll, and Rainer F. Mahrt, Thorsten Wahlbrink, Jens Bolten, Thomas Mollenhauer, and Christian Moormann, Ulli Scherf
Organic mixed-order photonic crystal lasers with ultrasmall footprint
APPLIED PHYSICS LETTERS 91, 171108 2007

9. Z.-X. Xu, V. A. L. Roy, P. Stallinga, H.-F. Xiang, **M. Muccini**, S. Toffanin and C.-M. Che
Nanocomposite Field Effect Transistors based on ZnO / MEH-PPV blends
APPLIED PHYSICS LETTERS, 90 (2007), 223509.

10. C. Dragonetti, L. Falciola, P. Mussini, S. Righetto, D. Roberto, R. Ugo, A. Valore, F. De Angelis, S. Fantacci, A. Sgamellotti, M. Ramon and M. Muccini
The Role of Substituents on Functionalized 1,10-Phenanthroline in Controlling the Emission Properties of Cationic Iridium(III) Complexes of Interest for Electroluminescent Devices.
INORGANIC CHEMISTRY, 46 (2007) 8533-8547.

11. F. Todescato, R. Capelli, F. Dinelli, M. Murgia, N.Camaioni, M. Yang and M. Muccini
Influence of the dielectric and of the active layer doping on the FET mobility in PPV-based devices
SPIE 6655 «Organic Light Emitting Materials and Devices XI », Ed. by Z. H. Kafafi and F. So (2007), Pg. 665514-1.

12. Sarah Schols, Stijn Verlaak, Cédric Rolin, David Cheyns, Jan Genoe, and Paul Heremans
An Organic Light-Emitting Diode with Field-Effect Electron Transport
ADV. FUNCT. MATER., 18 (2008), 136–144

13. T. Benincori, F. De Angelis, M. Capaccio, L. Falciola, M. Muccini, P. Mussini, A. Ponti, S. Toffanin, P. Traldi, and F. Sannicolò
Spider-like Oligothiophenes
CHEMISTRY - A EUROPEAN JOURNAL, 14 (2008) 459

14. Raffaella Capelli, Franco Dinelli, Stefano Toffanin, Francesco Todescato, Mauro Murgia, Michele Muccini, Antonio Facchetti, Tobin J. Marks
Investigation of the Opto-Electronic Properties of Organic Light Emitting Transistors Based on an Intrinsically Ambipolar Material
JOURNAL OF PHYSICAL CHEMISTRY, 112 (2008) 12993.

15. T. Wahlbrink, J. Bolten, T. Mollenhauer,H. Kurz, K. Baumann, N. Moll, T. Stöferle, R.F. Mahrt
Fabrication and characterization of Ta2O5 photonic feedback structures.
MICROELECTRONIC ENGINEERING, , 85, (2008), 1425.

16. Todescato, F.; Capelli, R.; Dinelli, F.; Murgia, M.; Camaioni, N.; Yang, M.; Bozio, R.; Muccini, M.
Correlation between Dielectric/Organic Interface Properties and Key Electrical Parameters in PPV-based OFETs
JOURNAL OF PHYSICAL CHEMISTRY B, 112 (2008) 10130.

17. Cabanillas-Gonzalez, J.; Sciascia, C.; Lanzani, G.; Toffanin, S.; Capelli, R.; Ramon, M. C.; Muccini, M.; Gierschner, J.; Hwu, T.-Y.; Wong, K.-T.
Molecular Packing Effects on the Optical Spectra and Triplet Dynamics in Oligofluorene Films
JOURNAL OF PHYSICAL CHEMISTRY B, 112 (2008) 11605.

18. R. Zamboni, R. Capelli, S. Toffanin, M. Murgia, M. Först and M. Muccini.
OLET architectures for electrically-pumped organic lasers
SPIE Vol. 7118 71180C-5

19. Mai-Yan Yuen, V. A. L. Roy, Wei Lu, Steven C. F. Kui, Man-Ho So, Stephen Sin-Yin Chui, Michele Muccini, J. Q. Ning, S. J. Xu, and Chi-Ming Che
Semiconducting and Electroluminescent Nanowires Self-assembled from Organoplatinum(II) Complexes
ANGEWANDTE CHEMIE INTERNATIONAL EDITION 47 (2008), pp. 9895

20. S.Schols, C. McClatchey, J. Genoe, P. Heremans and A. Facchetti, SPIE Proc, 6999,699910, (2008).

21. S. Schols, C. McClatchey, C. Rolin, D. Bode, J. Genoe, P. Heremans and A. Facchetti, Adv. Funct. Mater. 44, (2008),15

22. S. Schols, L. Van Willigenburg, R. Müller, D. Bode, M. Debucquoy, S. De Jonge, J. Genoe, P. Heremans, S. Lu and A. Facchetti,
Appl. Phys. Lett. 93, (2008), 263303.

23. K. Baumann, N. Moll, T. Stöferle, T. Wahlbrink, J. Bolten, J. Mollenhauer, C. Moormann, B. Wang, U. Scherf, and R. F. Mahrt
Ultra-small footprint photonic crystal lasers with organic gain material
Proceedings of the SPIE, 6999, 699906 (2008)

24. K. Baumann, T. Stöferle, N. Moll, R. F. Mahrt, T. Wahlbrink, J. Bolten, and C. Moormann
Mixed-order photonic feedback structures for organic lasers
Proceedings of the SPIE Europe, Strasbourg, April 7-10, 2008

25. R. F. Mahrt,
Ultrasmall footprint photonic-crystal lasers with organic gain
Material Laser & Photonics Reviews (invited paper) to be submitted

26. M. Muccini
Advancements in Organic Light emitting transistor technology
Laser & Photonics Reviews (invited paper) to be submitted

Media coverage:

1. physorg.com, 19.11.2007
"Researchers present new solution for miniaturized organic lasers"
2. LASER FOCUS WORLD, Volume 44, Issue 1, January 2008
"ORGANIC OPTOELECTRONICS: European team characterizes photonic-feedback structures for mini organic lasers"
3. S. Schols, Laser Focus World, Volume 44, Issue 3, March , 2008

"*Remote cathode paves way for electrically pumped organic laser"*

Overview table on dissemination activities.

Planned/ actual Dates	**Type**	**Type of audience**	**Countries addressed**	**Size of audience**	**Partner responsible /involved**
	Project web-sites				
January 2006	www.bo.ismn.cnr.it/OLAS	*Research*	*International*		CNR
Feb. '08	www.olasproject.eu	*Research*	*International*		CNR
	Conference organization:				
2-7 April 2006	SPIE - Photonics Europe	*Research*	*International*	*hundreds*	CNR; IMEC
7-10 April 2008	SPIE – Photonics Europe	*Research*	*International*	*hundreds*	CNR; IMEC
9-12 Sept. 2008	EL2008	*Research*	*International*	*hundreds*	CNR
	Talks at Conferences				
2-7 April 2006	*SPIE Photonics Europe 2006 [*S. Verlaak, IMEC]	*Research*	*International*	*hundreds*	IMEC

Planned/ actual Dates	**Type**	**Type of audience**	**Countries addressed**	**Size of audience**	**Partner responsible /involved**
2-7 April 2006	*SPIE Photonics Europe 2006 [F.Dinelli,* CNR]	*Research*	*International*	*hundreds*	CNR
2-7 April 2006	*SPIE Photonics Europe 2006 [*E. DaComo, CNR]	*Research*	*International*	*hundreds*	CNR
13-17 August 2006	*SPIE Optics and Photonics West 2006 [S. Schols, IMEC]*	*Research*	*International*	*hundreds*	IMEC
13-17 August 2006	*SPIE Optics and Photonics West 2006 [M. Muccini, CNR, INVITED]*	*Research*	*International*	*hundreds*	CNR
15-19.07.07	*Advanced Polymer Materials For Photonics And Electronics (Prague)*	*Research*	*International*	*hundreds*	*IBM*
11.-15.06.07	*7th International Conference on Optical Probes of π-Conjugated Polymers and Functional Self Assemblies (Turku)*	*Research*	*International*	*hundreds*	*IBM*
28.-31.10.07	*Application and development of ultrafast- and nano-optics (Beijing)*	*Research*	*International*	*hundreds*	*IBM*
22-23 January 2007	OLEDW 2007	*Research*	*International*	*hundreds*	CNR
11-15 June 2007	OP2007	*Research*	*International*	*hundreds*	IBM
11-15 June	OP2007	*Research*	*International*	*hundreds*	CNR

Planned/ actual Dates	Type	Type of audience	Countries addressed	Size of audience	Partner responsible /involved
2007					
15-19 July 2007	Advanced Polymer materials for photonics and electronics	*Research*	*International*	*hundreds*	IBM
26-30 August 2007	*SPIE Optics + Photonics*	*Research*	*International*	*hundreds*	IBM
26-30 August 2007	*SPIE Optics + Photonics*	*Research*	*International*	*hundreds*	CNR
5-8 Sept 2007	ECME	*Research*	*International*	*hundreds*	IMEC
23-26 Sept 2007	MNE07	*Research*	*International*	*hundreds*	AMO
28-31 October2 007	Application and development of ultrafast- and nano-optics (Beijing)	*Research*	*International*	*hundreds*	*IBM*
23-25 January 2008	*Quantum Systems and Technologies (QSIT)*, Arosa (CH) [T. Stoeferle]	*Research*	*International*	*hundreds*	*IBM*
6-10 April 2008	SPIE Photonics Europe 2008 [S. Schols, P. Heremans]	*Research*	*International*	*hundreds*	IMEC
7-10 April 2008	*SPIE Europe*, Strasbourg, 2008 [R. Mahrt,, INVITED]	*Research*	*International*	*hundreds*	IBM
12 May 2008	*Cavendish Laboratory Seminar*, Cambridge (UK) [T. Stoeferle, INVITED]	*Research*	*International*	*hundreds*	IBM

Planned/ actual Dates	**Type**	**Type of audience**	**Countries addressed**	**Size of audience**	**Partner responsible /involved**
30 June 2008	*Kyushu University, Center for Future Chemistry*, Fukuoka (Japan) [R. Mahrt, INVITED]	*Research*	*International*	*hundreds*	IBM
1 July 2008	*Kyoto University, Graduate School of Engineering, Department of Electronic Science and Engineering, Quantum Optoelectronics* Kyoto (Japan) [R. Mahrt, INVITED]	*Research*	*International*	*hundreds*	IBM
10-14 August 2008	*International Symposium on Optics & Photonics 2008*, (USA). [M Muccini,. INVITED]	*Research*	*International*	*hundreds*	CNR
19-23 August 2008	*International Symposium on Organic Transistors and Functional Interfaces (OFET2008),* Sendai (Japan). [M. Muccini, INVITED]	*Research*	*International*	*hundreds*	CNR
17 August	University of Fukuoka, Center for	*Research*	*International*	*hundreds*	CNR

Planned/ actual Dates	**Type**	**Type of audience**	**Countries addressed**	**Size of audience**	**Partner responsible /involved**
2008	Future Chemistry, Fukuoka (Japan). [M. Muccini, INVITED]				
29 Sept-2 Oct. 2008	*EOS Annual Meeting 2008,*, Paris (France). [M. Muccini, INVITED]	*Research*	*International*	*hundreds*	CNR
29 Sept-2 Oct. 2008	*EOS Annual Meeting 2008,*, Paris (France). [R. Mahrt, INVITED]	*Research*	*International*	*hundreds*	IBM
2 October 2008	Institut Optique, Paris, France, [R. Mahrt, INVITED]	*Research*	*International*	*hundreds*	IBM
	Publications				
	NATURE MATERIALS **5** (2006) 605				CNR
	ADVANCED MATERIALS 18 (2006) 1416				CNR
	APPLIED PHYSICS LETTERS, 89, pp223504 (2006)				IMEC
	JOURNAL OF PHYSICS: CONDENSED MATTER 18 (2006) S2127				CNR
	SPIE Proceedings				IMEC

Planned/ actual Dates	Type	Type of audience	Countries addressed	Size of audience	Partner responsible /involved
	Paper 6192-16				
	SPIE Proceedings, Paper 6333-29				CNR
	SPIE Proceedings, Paper 6333-30				IMEC
	APPLIED PHYSICS LETTERS 91, 171108 (2007)				IBM/AMO
	APPLIED PHYSICS LETTERS 90, (2007), 223509				CNR
	INORGANIC CHEMISTRY, 46, (2007), 8533				CNR
	SPIE proceedings paper 665514-1.				CNR
	ADV. FUNCT. MATER. 18, (2008), 136–144				IMEC
	CHEMISTRY - A EUROPEAN JOURNAL, 14, (2008), 459				CNR
	JOURNAL OF PHYSICAL CHEMISTRY, 112, (2008), 1425				CNR
	MICROELECTRONIC ENGINEERING, 85, (2008), 12993.				AMO/IBM
	JOURNAL OF PHYSICAL CHEMISTRY B, 112, (2008) 10130				CNR
	SPIE VOL. 7118 71180C-5				CNR
	ANGEWANDTE CHEMIE INTERNATIONAL EDITION 47, (2008), PP. 9895				CNR

Planned/ actual Dates	Type	Type of audience	Countries addressed	Size of audience	Partner responsible /involved
	SPIE PROC, 6999,699910, (2008)				IMEC
	Adv. Funct. Mater. 44, (2008),15				IMEC
	Appl. Phys. Lett. 93, (2008), 263303				IMEC
	Proceedings of the SPIE, 6999, 699906				IBM
	Proceedings of the SPIE Europe, Strasbourg, April 7-10, 2008				IBM
	Media Coverage				
19 Nov 2007	physorg.com	Wider scientific community	**International**	*Thousands*	AMO
January 2008	LASER FOCUS WORLD, Volume 44, Issue 1	Wider scientific community	**International**	*Thousands*	AMO/IBM
March 2008	Laser Focus World, Volume 44, Issue 3 [S. Schols]	Wider scientific community	**International**	*Thousands*	IMEC

c. Publishable results

- Exploitable knowledge #1, "Enhanced surface emitting photonic crystal device"

We report on a vertical surface-emitting organic laser structure with a high-index Ta_2O_5 two-dimensional (2D) photonic crystal layer with reduced lasing threshold. The second-order photonic crystal is surrounded by a first-order photonic crystal mirror which acts as a distributed Bragg reflector (DBR). In this way more light is confined within the resonator, resulting in a dramatically reduced footprint of the lasing device. The basic idea is to enclose a second-order vertically emitting laser structure by mirrors in order to reflect light back into the active region otherwise lost due to leakage. Here, we choose first-order structures as mirrors because they show no perpendicular out-coupling. Since the mirror structure is integrated into the same planar Ta_2O_5 layer

as the second-order lasing structure the layer thicknesses of the Ta_2O_5 as well as of the organic gain material (MeLPPP) are fixed. Therefore, only the lattice constant and the hole radii forming the structure are free parameters. For a lattice constant of 150 nm, second-order band-edge lasing occurs around 494nm, close to the gain maximum of our polymer material. The magnitude of the bandgap does not change very much over a certain range of hole radii whereas the wavelengths decrease for increasing radii due to the higher total fraction of MeLPPP in the structure (MeLPPP fills the holes). This allows for shifting the bandgap region according to the desired laser emission wavelength. In order to center the bandgap around the lasing wavelength defined by the second-order structure a hole radius of 50 nm is chosen.

Lasing has been observed for both types of devices fabricated. However, the 25µm x 25µm as well as the 15µm x 15µm second-order-only structures (no first-order mirrors) showed no lasing. In contrast, all mixed-order photonic crystal structures, even the smallest ones, showed lasing with a considerably reduced lasing threshold compared with their second-order only counterparts. Here, the first-order photonic crystal structure reflects the propagating laser mode back into the second-order photonic crystal structure, therefore enhancing the propagation length and thus satisfying the requirements for a certain interaction length for lasing. By using the mixed-order approach, all structures provide the coupling length needed because of the mirror effect resulting from the first-order structure. Therefore, one can decrease the area of the vertical emitting laser by an order of magnitude and still work at the same lasing threshold level.

In summary, we have investigated laboratory prototypes of mixed-order two-dimensional photonic crystal laser structures based on a thin film of high-index Ta_2O_5 in combination with a high-gain organic polymer. We designed an optimized mixed-order structure by means of FDTD simulations and showed that the mixed-order structures are superior compared with the second-order only ones in terms of lasing threshold and in device footprint. Such small-footprint structures are key components of future integrated photonic devices for both communication and sensing applications. Furthermore, they offer an attractive packaging possibility for light-emitting arrays coupled to high-density optical interconnects.